SILICON CARBIDE (SiC) AND SILICON DIOXIDE (SiO_2) MICROMECHANICAL RESONATORS WITH ULTRA-LOW DISSIPATION

A Dissertation
Presented to
The Academic Faculty

Benoit Hamelin

In Partial Fulfillment
of the Requirements for the Degree
Doctor of Philosophy in the
School of Electrical and Computer Engineering

Georgia Institute of Technology
December 2018

SILICON CARBIDE (SiC) AND SILICON DIOXIDE (SiO_2) MICROMECHANICAL RESONATORS WITH ULTRA-LOW DISSIPATION

Approved by:

Dr. Farrokh Ayazi, Advisor
School of Electrical and Computer Engineering
Georgia Institute of Technology

Dr. Azadeh Ansari
School of Electrical and Computer Engineering
Georgia Institute of Technology

Dr. Pamela Bhatti
School of Electrical and Computer Engineering
Georgia Institute of Technology

Dr. Oliver Brand
School of Electrical and Computer Engineering
Georgia Institute of Technology

Dr. Peter J. Hesketh
School of Mechanical Engineering
Georgia Institute of Technology

Date Approved: November 5th, 2018

To my angels Alex, Grand-père, Mamine, Rozenn, Susanne and Simone

To my ever-supportive family and friends

To my loving wife

ACKNOWLEDGEMENTS

Dr. Ayazi is one of the select few in the field that continuously and with a sense of urgency pushes the state-of-the-art beyond reason. I am fortunate to have had Dr. Ayazi as a mentor throughout the years and help me navigate challenging research projects. I am grateful to have learned so much under his guidance and his dedication. Further, in 2014, I had the bad luck of having to take a leave from research for over 6 months; I am forever grateful that Dr. Ayazi facilitated my return by letting me lead our SiC efforts. This particular effort has lasted much longer than expected but enabled me to learn so much and to elevate my work standards.

I would like to thank my committee members Dr. Ansari, Dr. Bhatti, Dr. Brand, and Dr. Hesketh for their feedback and insights during the proposal and dissertation process.

I would like to thank Gary Spinner, Vinh Nguyen, Andrew Watkins and Thomas Johnson-Averette for their everlasting dedication to make the STS AOE tool meet our high standards. I would like to thank Dr. Thomas for many insightful discussions. I would like to thank the many other staff members of IEN that are so instrumental day in and day out.

Fruitful discussions with former and fellow labmates have been key to learn to navigate through the cleanroom. I wish to thank IMEMS members Dr. Casinovi, Dr. Chan, Mr. Daruwalla, Mr. Hodjat-Shamami, Dr. Jeong, Dr. Ko, Dr. Norouzpour-Shirazi, Dr. Serrano, Dr. Shao, Dr. Sorenson, Dr. Tabrizian, Dr. Tavassoli, Dr. Wen, Mr. Yang. I would also like to thank collaborators and particularly Dr. Li. I would like to thank friends from other Georgia Tech research groups for guiding me including Nordine and Iacopo

I would like to thank my wonderful roommates Autumn, Aurélie, Alli, Dickson, Federico, Joel, Sandra, Tobias, my man Andreas and my close ‘frenchies’ Harold, Léa, Laetitia, Maurine, Pauline, Raul, Robert, Tori; you have been such a great group helping through the toughest moments.

The emotional support of my loving parents Bernard and Christine and of my ever-supportive siblings Sophie, Charlotte, Olivier and Jean has been tremendously helpful from day one despite the long distance. I would like to apologize to my nephews and nieces, my cousins, my aunts and uncles and my grandparents for missing so many important family events while pursuing my work. I am grateful for my godfather Dr. Balagna who took so good care of me. I am forever in debt.

Myriam Hamelin, I am blessed to have married you. You have been patient, kind, thoughtful, loving, calming. You are the bedrock and foundation upon which this work and dissertation relies on. I am so much looking toward the next chapters in our lives.

TABLE OF CONTENTS

LIST OF TABLES

LIST OF FIGURES

LIST OF SYMBOLS AND ABBREVIATIONS

Abbreviation		Symbol
Δf	Frequency split	
μHRG	Micro HRG	
d	Average grain size	
ρ	Density	
C_P	Specific heat capacity per unit mass	
κ	Thermal Conductivity	
AIR	Viscous damping	Q_{AIR}
ALD	Atomic Layer Deposition	
Al_2O_3	Alumina	
ANC	Anchor loss	Q_{ANC}
AKE	Akhiezer	Q_{AKE}
AOE	Advanced Oxide Etcher	
B	Shear modulus	
BW	Bandwidth	
BAW	Bulk Acoustic Wave	
CTE	Coefficient of Thermal Expansion	α
C_v	Specific heat capacity per unit volume	
δ	Thickness of dissipative layer	
DRIE	Deep Reactive Ion Etching	
DSP	Double Side Polished	

ϵ	Strain	
E	Young's modulus	
E_{ds}	Imaginary component of E	
HARPSS	High-Aspect-Ratio Poly and Single Crystal Silicon	
HRG	Hemispherical Resonator Gyroscope	
k_B	Boltzmann constant	
λ	Thermal eigenfrequency	
LDV	Laser Doppler Vibrometer	
LPCVD	Low Pressure Chemical Vapor Deposition	
MEMS	Micro Electro-Mechanical Systems	
MNEΩ	Mechanical Noise Equivalent Rotation	
ν	Thermal eigenmode	
PSSR	Pierced Shallow Shell Resonator	
PnC	Phononic crystal	
Q	Quality Factor or Q-factor	Q
RCA	Radio Corporation of America	
RTP	Rapid Thermal Annealing	
SCS	Single-Crystal Silicon	
SSR	Shallow Shell Resonator	
T_0	Temperature	
t	Thickness	
TED	Thermo-elastic Damping	Q_{TED}
TEOS	Tetraethyl Orthosilicate	
ω	Mechanical pulsation	

W_{Stored} Stored energy

SUMMARY

Silicon carbide (SiC) and silicon dioxide (SiO_2) are both promising materials in the quest for micromechanical resonators with ultra-low dissipation. Because of the legacy of the IC industry and ease of fabrication, silicon (Si) has been the prominent structural material for MEMS devices. However, from the perspective of dissipation, SiC and SiO_2 may outperform Si: Akhiezer damping (AKE) in SiC and thermoelastic damping (TED) in SiO_2 are greatly reduced comparatively to Si. The implementation of high-Q SiC and SiO_2-based micromechanical resonators involves several challenges. This dissertation attempts to address those challenges to facilitate the deployment of high-performance resonant sensors made from SiC and SiO_2 for high-performance applications in harsh environments.

The first part of this dissertation presents fabrication and characterization of 1 mm-wide low-frequency (10-100kHz) thin shallow shell resonators in SiO_2, a miniature version of the lauded Hemispherical Resonant Gyroscope (HRG). The unique out-of-plane curving profile of the shallow shells in conjunction with self-aligned hollow pedestals decouples the SiO_2 shells from the Si substrate acoustically, mitigating anchor loss. It has been shown that AKE and TED are not the limiting dissipation mechanisms due to the low frequency operation and the near-zero coefficient of thermal expansion (CTE) of SiO_2. The fabricated shallow shells exhibit high Q-factors independent of frequency up to 1MHz, an unambiguous signature of surface loss.

The second part of this dissertation investigates fabrication of bulk acoustic wave (BAW) resonators in single-crystalline SiC. Like Si, SiC resonators can be interfaced with

integrated SiC electronics. SiC presents exceptional acoustic properties with an Akhiezer dissipation limit approximately 60 times smaller than Si. Based on previous work in Si, bulk acoustic wave (BAW) disk resonators are ideal to attain the quantum Akhiezer limit of Q in SiC. In this effort, SiC disk resonators display Q-factors that are beyond the theoretical reach of Si with an $f.Q$ product of 1.9E13Hz (Q=3.8M and f=5MHz). The implementation of ultra-low dissipation SiC resonators required custom-fabrication of SiC-on-Insulator substrates, development of a SiC deep reactive ion etching (DRIE) process that yields very smooth vertical sidewalls, and devising a method to acoustically decouple solid SiC disk resonators from its supporting substrate. The ultra-high Q SiC resonators are 2 mm wide, completely solid disks anchored at their center by a self-aligned SiO_2 post on a Si phononic crystal (PnC). Self-aligned SiC electrodes surround the SiC disk, enabling integrated actuation and pick-off of the resonators. Fabrication constraints limit the width of the transduction gap to 5μm which is insufficient to electrostatically match and align the stiff BAW gyroscopic modes, making permanent frequency trimming desirable.

The third part of this dissertation investigates localized stiffness trimming of Si micromechanical resonators to selectively shift frequencies and reduce the frequency separation between gyroscopic modes while maintaining ultra-high Q-factors. Upon exposure to UV radiation from a laser source, isolated patches of a trimming material (e.g. aluminum, gold, germanium) diffuse into the silicon substrate; after the eutectic composition is reached, localized melting occurs. During cooling, the melt solidifies with a different Young's modulus than that of silicon or that of the trimming layer, modifying the strain energy density distribution and ultimately the frequency of the resonator.

CHAPTER 1. INTRODUCTION

1.1 Background

This thesis aims to add a stone to the collective endeavor of investigating novel fabrication methods of chip-scale ultra-high-performance resonators and resonant gyroscopes and their frequency control [1]. High-performance macro-scale gyroscopes such as the Hemispherical Resonating Gyroscope (HRG [2], [3]) have been deployed successfully in outer-space. The HRG (Figure 1) is a pedestal-supported shell-shaped resonator with gyroscopic modes that are driven and picked-off capacitively with a set of surrounding electrodes. The HRG is manufactured by transforming a solid rod of fused quartz into a shell. A publicly available video on fabrication of the HRG by SAGEM is available Video of fabrication of the HRG by Sagem, France. It is important to note that this fabrication method cannot be miniaturized directly [4]. The HRG is remarkable because it is extremely robust (1M operation hours without failure) due to the simple and balanced design while exhibiting record-low dissipation. The material choice (fused quartz

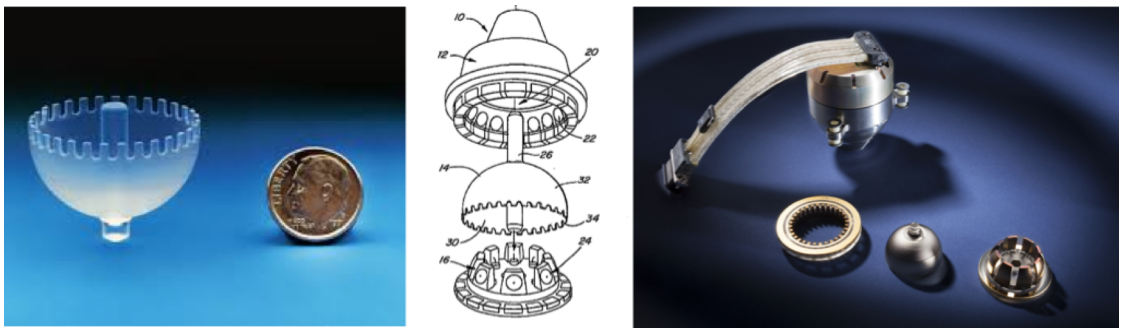

Figure 1: (left) The HRG with tines at the rim for laser-based mode balancing (center) Illustration of the HRG patent from Northrop-Grumman which shows (right) the assembled HRG with its subcomponents.

[5]) is key to minimize thermo-elastic damping (TED [6]). The 3D curved design of the HRG enables low-frequency operation while minimizing footprint. The exact shape and thickness of the HRG's shell is key to minimize acoustic dissipation via the anchor [7]. These features (material property, shell's curvature and acoustic decoupling to boost *Q*) will be discussed in more details throughout this dissertation.

The MEMS community has developed micro-scale gyroscopes for over 30 years now [8]. MEMS-scale gyroscopes that are commercially available are 2D due to fabrication limitations [9]. While introduced over half a decade ago, 3D MEMS gyroscopes are still confined to the laboratory space ([10], [11], [12], [13], [14]). Since miniaturizing the design while maintaining the same level of performance of the HRG is challenging (see discussion in CHAPTER 3), exploring novel substrate materials provides another route to improve the performance of 2D MEMS gyroscopes [15], [16]. The main advantage of this route is that proven MEMS designs can be used with minimal change; however, introducing a new material requires developing new fabrication technologies.

To compare gyroscopes of different size, design and frequency, the author will use throughout this dissertation the commonly-accepted Quality factor or *Q*-factor or *Q* ([17], [18], [19], [20], [21]). The quality factor of a resonator is the ratio of stored energy over dissipated energy per cycle of vibration [16]. In short, high *Q* values are crucial to boost performance of mode-matched gyroscopes via mechanical *Q* amplification (see 1.3). The HRG boasts a *Q*-factor in the 25M range while miniature HRGs show *Q*s under 10M [22] and 2D flat gyroscopes near 1M [23]. As a side note, the *Q*-factor is not the only relevant parameter; in addition to familiar parameters (cost, size, weight, power consumption),

robustness to shock and vibrations below 100 kHz is key [24]. In this dissertation, only Q will be discussed.

1.2 Thermal fluctuations and quality factor of a harmonic linear oscillator

Dissipative harmonic oscillators underlie many endeavors from large scale gravitational wave detectors to clocks [19], and resonant gyroscopes [17]. Fabricating resonators as lossless as possible is key. Indeed, as dissipation is more pronounced, the desired signals are masked by fluctuating forces. Thermal noise generates these fluctuating forces per the fluctuation-dissipation theorem.

In 1928, at Bell Laboratories, Johnson discovered thermal noise, which was later explained and generalized by Nyquist's fluctuation-dissipation theorem. In the absence of an applied voltage and due to the random vibration of charged carriers, thermal noise in a resistor R at equilibrium and at the temperature T generates a voltage $\langle V^2 \rangle = 4Rk_BT\Delta\nu$ where $\Delta\nu$ is the measurement's bandwidth.

More generally, the free oscillation of a linear oscillator is described by:

$$M\ddot{x} + D\dot{x} + Kx = 0 \tag{1.1}$$

where M is the effective mass, D the friction coefficient and K the spring constant. The solution to this equation is:

$$x(t) = x_0 \exp(-\delta t) \cos(\omega t + \phi) \tag{1.2}$$

where $\delta = \frac{D}{2M}$, $\omega^2 = \frac{K}{M} - \delta^2$, $\tau^* = \delta^{-1}$, $Q = \frac{\omega\tau^*}{2}$, and x_0, ϕ are determined by the oscillator's initial condition. Q is a measure of how many oscillations the resonator undergoes before its amplitude decays by a factor of e. When a linear harmonic oscillator couples to a heat bath at temperature T_0, then the heat bath exerts a random force on the oscillator. This random force has a frequency-independent spectral density of $4k_BT_0D$ per Nyquist's fluctuation-dissipation theorem. Therefore, the minimum force that can be detected by the oscillator is:

$$F_{min} \geq \sqrt{4k_BT_0D\Delta f_{EQNB}} = \sqrt{\frac{4Kk_BT_{Bath}\Delta f_{EQNB}}{\boldsymbol{Q}\omega}} \tag{1.3}$$

where Δf_{EQNB} is the equivalent noise bandwidth of the system, $k_B$is Boltzmann constant. To increase the signal to noise ratio (SNR), it is key to minimize F_{min}. While the mass M and the frequency ω are typically constrained by $\frac{M}{\omega^2} = K$ with K defined by material property, design and boundary conditions, Q is the only unrestrained parameter. In acoustic resonators, Qs can reach 10M [22] and using appropriate lossless materials even 800M at room temperature [18]. The reader is advised to consult [19] from which this sub-section 1.1 has been derived freely.

1.3 Essence of high performance high Q resonant MEMS gyroscopes

Resonant gyroscopes (Figure 2) possess a pair of resonant modes that are coupled via the Coriolis force. Upon driving one mode (namely the drive mode) to the amplitude q_{Drive}, assuming the modes possess identical resonance frequencies $\omega_{01} = \omega_{02}$ and the

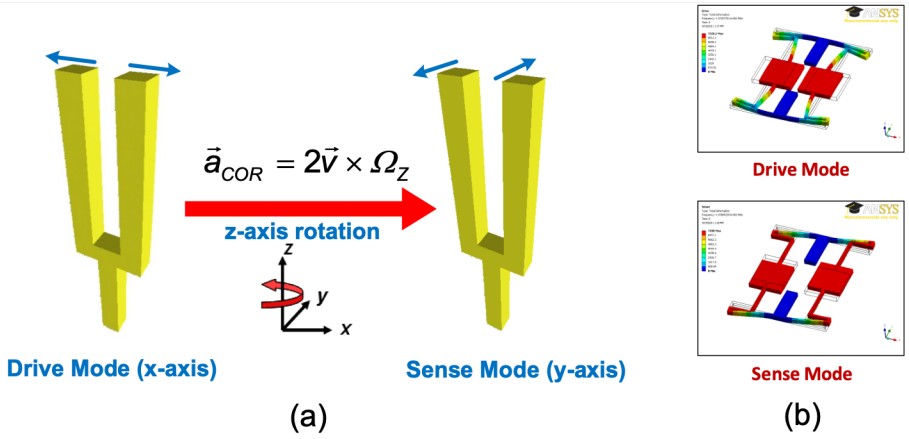

Figure 2: (a) Coriolis effect in a tuning fork, (b) Tuning-fork gyroscope operating based on this principle.

electrical noise is negligible, then the minimal rotation that can measured by the resonant gyroscope due to the Coriolis effect is given by:

$$MNE\Omega = \frac{1}{2q_{drive}} * \sqrt{\frac{4k_B T_{Bath}}{\omega_0 M \boldsymbol{Q_{Sense}}} * BW} \tag{1.4}$$

Maximizing the product $q_{Drive}\sqrt{\omega_0 M Q_{Sense}}$ is key to minimize $MNE\Omega$ and optimize the sensitivity of the resonant gyroscope. Again, it appears that minimizing dissipation (equivalently maximizing Q) is crucial in achieving high performance in acoustic sensors. However, unlike for the linear harmonic oscillator where there was no condition on the frequency ω (see 1.1), Q amplification only occurs under the mode matching conditions $\omega_{01} = \omega_{02}$ [25]. More precisely, the sensitivity $\frac{x_{Sense}}{\Omega}$ of a resonant gyroscope is given by:

$$\frac{x_{Sense}(t)}{\Omega} = \frac{a_{Cor}\cos(\omega_{01}t+\phi)+a_Q \sin(\omega_{01}t+\phi)}{\omega_{01}\times\sqrt{(2\boldsymbol{\Delta\omega})^2+\left(\frac{\omega_{02}}{\boldsymbol{Q_{sense}}}\right)^2}}, \phi = \tan^{-1}\frac{\omega_{02}}{\boldsymbol{\Delta\omega Q_{Sense}}} \tag{1.5}$$

where $\Delta\omega = \omega_{02} - \omega_{01}$ is namely the frequency split between the drive and sense modes. In essence, the performance of mode-matched resonance gyroscope is maximized if the product $q_{Drive}\sqrt{\omega_0 M \boldsymbol{Q_{Sense}}}$ is maximized and if the Coriolis-coupled resonance frequencies are equal ($\omega_{01} = \omega_{02}$). This dissertation investigates achieving high Q resonators and to develop for the subset of resonators that have Coriolis-coupled resonant modes, techniques to match the resonance frequencies without degrading Q.

1.4 Organization of this dissertation

CHAPTER 1 revealed that resonant gyroscope sensitivity benefit from Q-amplification only under mode-matched conditions. CHAPTER 2 investigates various approaches to mitigate independent dissipation paths that define the overall Q-factor. CHAPTER 3 presents HRG miniaturization efforts and their practical limitations. CHAPTER 4 exposes efforts on replacing standard silicon (Si) with less dissipative materials, particularly silicon carbide (SiC). CHAPTER 5 displays a patented frequency control technology to mode match high Q MEMS resonators and resonant gyroscopes, which is key for MEMS gyroscopes to benefit to the fullest from high Q-factors (see 1.3).

CHAPTER 2. DISSIPATION IN MEMS RESONATORS

Low dissipation MEMS resonators are far from reaching their limits [26]. Theoretically, the limit is set by intrinsic mechanisms [16], [27], [28]; practically, the limit is set by extrinsic mechanisms [20], [29], [30]. The intrinsic limit is impossible to break while the extrinsic limit can be improved with better design and fabrication (see 2.1 and Table 1).

$$Q^{-1} = \sum_i Q_i^{-1} \tag{2.1}$$

Since Q is a measure of energy dissipation rate from the resonator to the surrounding thermal bath, it is intuitive that temperature plays a significant role in most dissipation

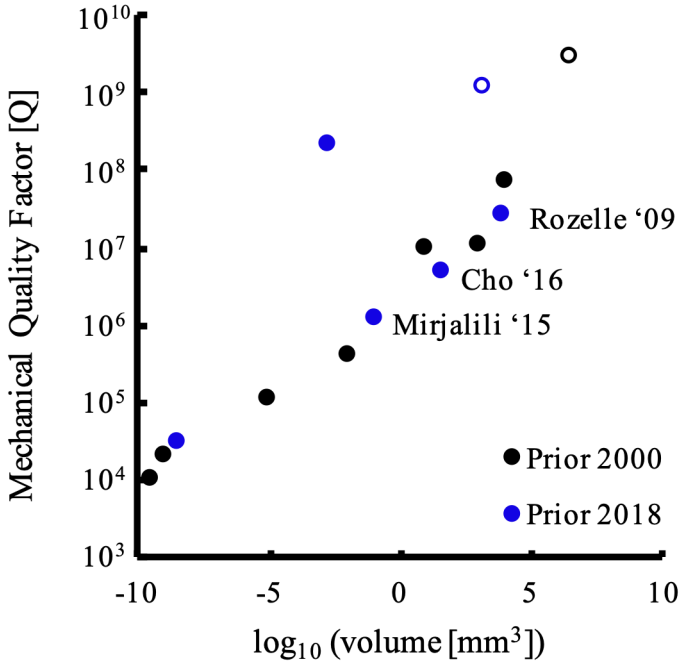

Figure 3: Dissipation vs volume in mechanical resonators up to 2018.

mechanisms [31]. Unfortunately, deployed resonators cannot be cooled down in practice to cryogenic temperatures. Moreover, as the volume of the resonators shrinks from macroscale to microscale so does the amount of energy that is stored inside the resonator's body [32]. The dependencies of Q on T and the resonator's volume are revealed in Figure 3. In this thesis, the resonators are MEMS scales with volumes near $1mm^3$ and at room temperature. Interestingly, today resonators with comparable volume and temperature show Q-factors in the 100-800M range [33]. These results show that MEMS gyroscopes with Qs in the 100k-10M range ([34], [22]) can still be greatly improved.

2.1 Sources of energy dissipation in acoustic resonators

Dissipation mechanisms (Table 1) that limit the Q-factor are either intrinsic (i.e. cannot be improved by design or fabrication) or extrinsic (i.e. can be improved by design or fabrication). In practice, extrinsic mechanisms, such as air damping or anchor loss [35], [36], [37], [38], [39], limit Q. The theoretical limit (assuming the extrinsic mechanisms are negligible by optimal design and fabrication) is set by intrinsic mechanisms such as phonon-phonon interactions (i.e. Akhiezer damping [27] and Landau-Rummer damping [28]), thermo-elastic damping (TED) [40] and phonon-electron damping [14]. Other dissipation mechanisms can occur such as charge redistribution in piezo-electric materials [41] or surface loss in high surface-to-volume ratio resonators [42], [43], [44] [45].

The ability to thermally grow a high-quality and stable (yet easy to etch in HF) oxide on Si [46], combined with the abundance of Si and of Si-compatible tools in the IC industry [8], made Si the standard material in MEMS. However, Si does not exhibit as low TED values as SiO_2 resonators [47], nor does Si exhibit an Akhiezer limit as high as SiC [18],

which are both intrinsic mechanisms. In summary, if every extrinsic dissipation mechanisms are assumed negligible, SiO_2 and SiC-based resonators have the potential to reach much higher *Q* values than Si-based resonators. The following chapters of this thesis are entirely dedicated in exploring SiO_2 and SiC MEMS resonators with the hope of reaching *Q*-factors that are beyond the Akhiezer limit of Si. As a side note, SiN resonators already show *Q* values that cannot be reached by Si resonators of similar dimensions [33].

Table 1 : Energy dissipation mechanisms in MEMS devices and classification by material intrinsicality.

Dissipation mechanism	**Symbol**	**Intrinsicality**
Phonon-phonon interaction	Q_{Ph-Ph}	Intrinsic
Phonon-electron interaction	Q_{Ph-El}	Intrinsic
Acoustic thermo-elastic dissipation	Q_{TED}	Intrinsic
Charge relaxation	Q_{CHARGE}	Intrinsic
Surface and interfacial loss	Q_{SURF}	Intrinsic
Anchor loss	Q_{ANC}	Extrinsic
Air/fluid damping	Q_{AIR}	Extrinsic

2.2 Intrinsic dissipative processes

2.2.1 Phonon-phonon damping

An ideal resonator is lossless with an infinite Q; that is zero dissipation or coupling to the thermal bath. Naturally, various physical phenomena exist to siphon energy from the device, limiting its ultimate performance by fundamental phonon-phonon interactions. When the phonon distribution is perturbed from its equilibrium distribution by an acoustic wave, normal and Umklapp scattering with thermal phonons act to bring the distribution back to equilibrium [48]. Strongly temperature and material dependent, dissipation is

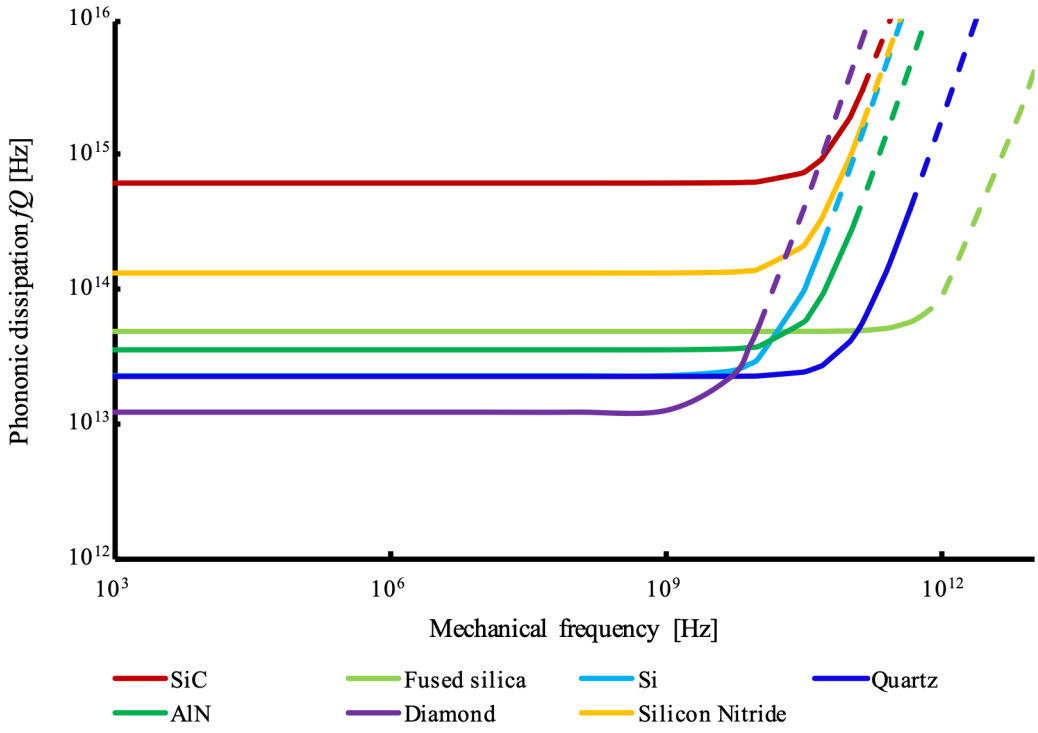

Figure 4: Phonon-phonon damping in common MEMS material. In the Akhiezer regime, SiC boasts the highest fQ product, near 10X above is close competitor SiN and almost 100X above standard Si.

minimal as lattice thermal vibrations are small; conversely, more lattice vibrations at high temperature offer more scattering opportunities [27], [28]. With a large stiffness and low average Grüneisen parameter [49], SiC is an ideal candidate for ultra-high Q sensors as it possesses an fQ_{AKE} of $6.4\times10^{14}Hz$, over 30 times higher than silicon's (Figure 4). However, other dissipation mechanisms must be addressed before reaching Akhiezer's limit. Due to the BAW disk resonator's relatively high operating frequency, in vacuum, bulk resonators typically suffer from TED and anchor losses [26]. Despite Si resonators being well-researched, there is no literature reporting on a resonator that is solely limited by Akhiezer [26].

2.2.2 Thermoelastic damping

Thermo-elastic dissipation occurs in any material that experiences thermal expansion [6]. As energy flows from hot spots in contraction to cold spots in extension, some energy is irreversibly lost via Joule heating [40]. In 1937, Zener [50] derived the expression of TED in a beam resonator for the fundamental flexural mode as follows:

$$\frac{1}{Q_{TED}} = \Delta_E \frac{\omega\tau_{th}}{1+(\omega\tau_{th})^2}, \quad \Delta_E = \frac{E\alpha^2 T_0}{\rho C_P}, \quad \tau_{th} = \frac{\rho C_P d^2}{\pi^2 \kappa} \tag{2.2}$$

where E is the Young's modulus, α the coefficient of thermal expansion, T_0 the temperature, ρ the density, C_p the specific heat capacity at constant pressure, d the average grain size, and κ is the thermal conductivity. Deriving a closed-form expression of TED for any mode in a resonator is a daunting task [51], [52]. While COMSOL (which is used throughout this dissertation) and other FEM tools can quickly and precisely compute TED

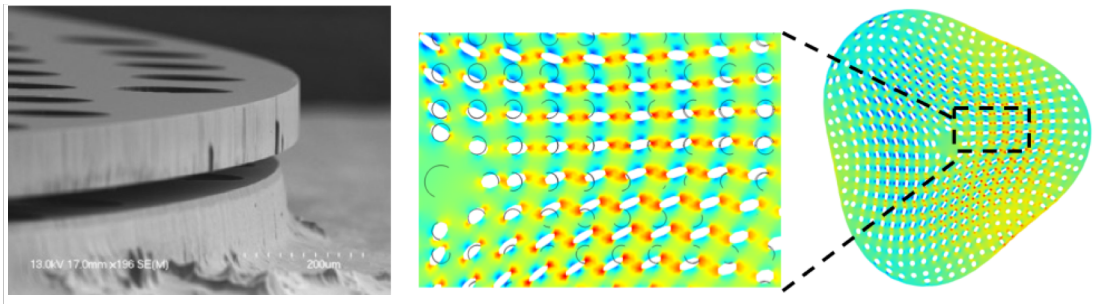

Figure 5: (left) SEM view of a gyroscope with release holes (right) Effect of release holes on the thermal paths [6].

for any resonator's shape (Figure 5), a semi-closed form expression remains of interest to guide the engineers to optimize TED [29], [53] in their resonators [54]. For this purpose, one can project the strain field on the normal thermal modes (Figure 6); compute the resulting TED distribution for each coupling; add all these contributions together to compute the total TED. Q_{TED}, as the sum of independent mechanical-thermal couplings (Figure 7), is expressed as [52]:

$$\frac{1}{Q_{TED}} = \frac{4.5}{W_{Stored}} \sum_i a_i^2 \left(T_0 \frac{B^2 \alpha^2}{c_v} \frac{\omega \lambda_i}{\omega^2 + \lambda_i^2}\right) \tag{2.3}$$

where a_i is the normalized overlap between the mechanical and thermal eigenmodes:

$$a_i \sim \frac{\int_V \epsilon(x,y,z) * v_i(x,y,z) d\Omega}{\int_V v_i^2(x,y,z) d\Omega} \tag{2.4}$$

where $\epsilon(x,y,z)$ is the strain field, ω the mechanical frequency and λ_i the thermal eigenfrequency of the normal thermal mode $v_i(x,y,z)$. Noteworthy $\lambda_0 = 0$ because there

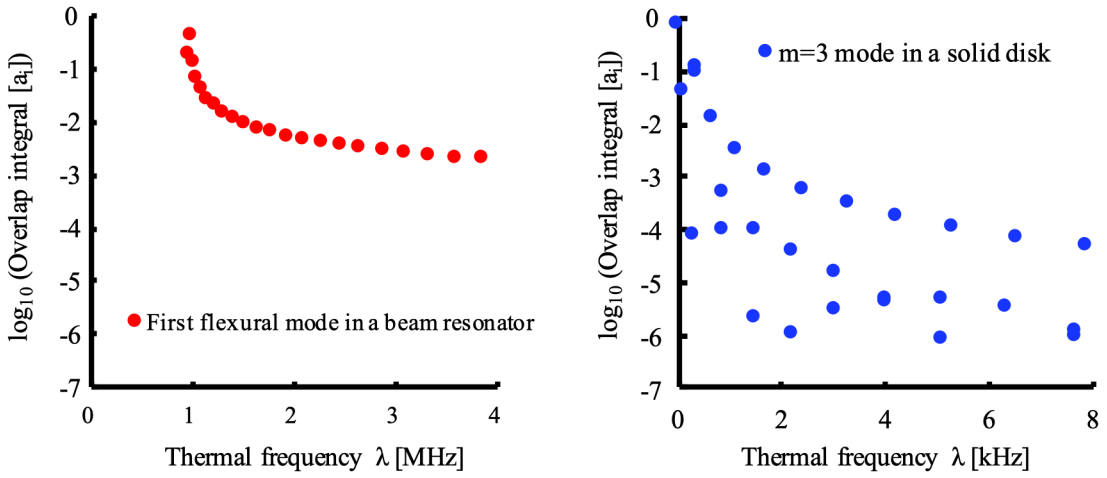

Figure 7: The mechanical-thermal overlap is much more uniform throughout the thermal eigenmodes in flexural resonators than in bulk acoustic wave resonators. Combined with a greater frequency discrepancy between their resonance frequency and the Debye peak, BAW resonators are set to be less sensitive to TED then their flexural counterparts.

are no temperature oscillations in the fundamental thermal eigenmode. A visual description of the projection of the strain field on the normal thermal eigenmodes is shown. From this semi-closed expression, separate strategies to mitigate TED emerge and will be discussed.

First, materials with minimal relaxation strength Δ_E are ideal candidates to maximize Q_{TED}. Because of its quadratic exponents, minimizing the coefficient of thermal expansion α plays a central role in reducing Δ_E. For comparison, Si shows $\alpha = 2.6 ppm/°C$ and SiC, $\alpha = 4.0 ppm/°C$. CHAPTER 3 takes advantage of the SiO_2's low CTE ($\alpha = 0.5 ppm/°C$) to fabricate high Q resonators. Some alloys, such as Invar-36 [14], also show extremely low coefficients of thermal expansion.

Second, isovolumetric modes that only have pure shear oscillations (e.g. Lamé, torsional modes) have $\epsilon(x, y, z) = 0$ and therefore do not exhibit any significant bulk TED.

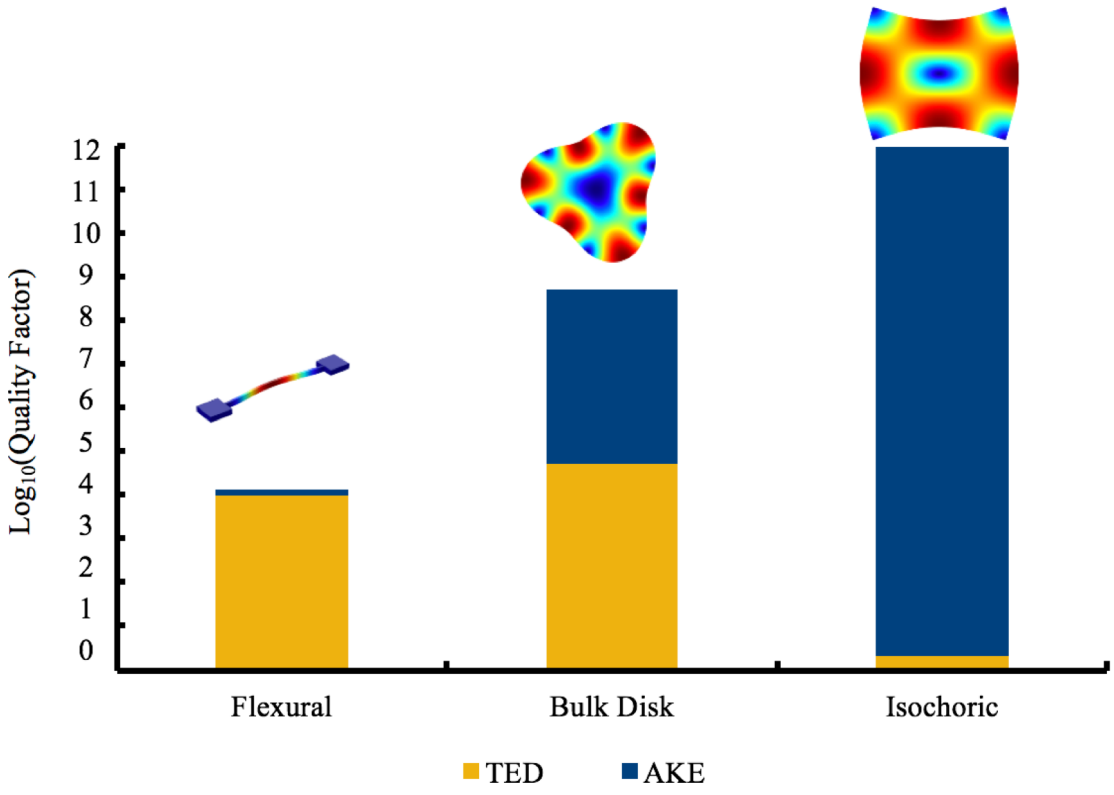

Figure 8: Relative contribution to the overall Q of TED and Akhiezer damping in beam, disk and square resonators.

Lamé mode resonators are used in this dissertation in CHAPTER 4 and CHAPTER 5; capacitive transduction of torsional modes is inefficient and these modes are not discussed further in this thesis (Figure 8).

Third, $\lambda_0 = 0$ because the fundamental thermal mode has no gradient. Thus, since $\sum_i a_i = 1$, forcing $a_o \sim 1$ and $a_i \sim 0$ otherwise, enables to optimize TED even in materials with large CTE values. For instance, bulk acoustic wave modes couple most of their strain energy to the lossless fundamental thermal mode [55]. If release holes are included [15], the strain energy will couple more and more to higher order dissipative

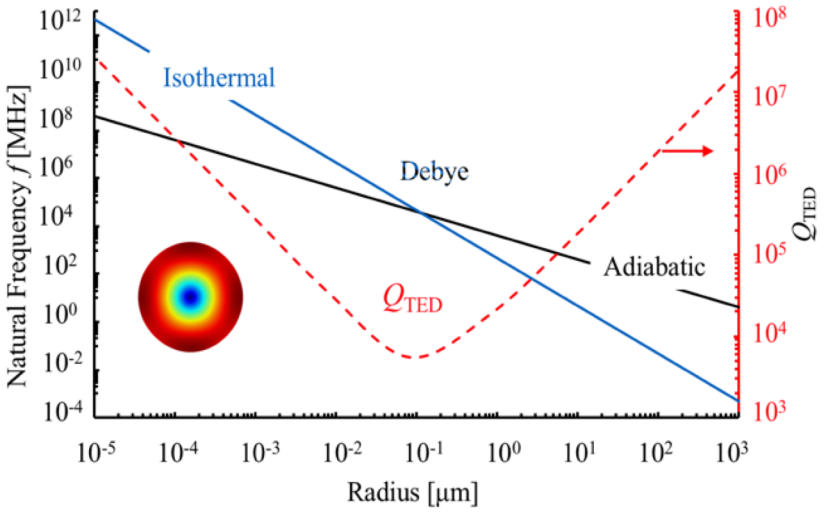

Figure 9: Bulk elliptical modes, the breathing mode in particular (star), of a 1540μm disk operate adiabatically where $f_{mechanical}$ (black)>>$f_{thermal}$ (blue). Minimum Q_{TED} (red) [158] occurs at the Debye frequency.

thermal modes [51]. Intuitively, including a release hole in an otherwise solid disk is creating new locations for hot and cold spots to emerge during oscillations inducing TED.

Fourth, and perhaps most significant approach to minimize TED ([55]), is to design the mechanical and thermal eigenfrequencies to be as disparate as possible to minimize the Debye factor $\frac{\omega\lambda_i}{\omega^2+\lambda_i^2}$ (Figure 9). Avoiding the Debye peak (maximum dissipation) and designing the resonator to operate in the isothermal or adiabatic regimes minimizes TED. SiC resonators that operate in the MHz regime such as the BAW modes are deep into the adiabatic regime with minimal TED dissipation. Inversely, flexural modes near lie near the Debye peak (typical frequency-determining dimensions are in the order of 1-10μm).

In summary, TED is minimized in materials with appropriate material properties (mostly near zero CTE) and in modes with either zero volume change (Lamé, torsional

modes) or that mostly couple to the fundamental thermal mode and deep into the adiabatic regime such as the BAW modes. SiC flexural gyroscopes [56] are doomed to exhibit low Q_{TED} values far from the limit set by Akhiezer. Bulk operation at MHz frequencies is key for SiC gyroscopes to attain the ultimate Akhiezer limit if anchor loss is mitigated for.

2.2.3 Dissipation due to phonon-electrons in metals

In conductive substrates, a strain wave set free electrons in motion. The viscous electron "gas" exchanges momentum between layers moving at different velocities, inducing friction. The resulting dissipation of longitudinal strain waves in a metal is given by:

$$\frac{1}{Q_{Ph-El}} = \frac{8}{15}\frac{\epsilon_F m_e \sigma}{\rho v^2 e^2} \tag{2.5}$$

Where m_e is the electron mass, e is the electron charge, ρ is the mass density, v is the velocity of sound waves, σ is the electric conductivity of the metal, and ϵ_F is the Fermi energy. The dissipation mechanisms described in sections 2.2.1, 2.2.2, 2.2.3 are fundamental and occur even in perfect crystals and metals. These mechanisms set the upper limit on Q regardless of design considerations or fabrication errors. Since phonon-electron dissipation occurs only in metals, non-conductive substrates typically are better candidates to exhibit high Q-factors. Other intrinsic losses that occur in piezoelectric materials such as charge redistribution [41] are not discussed in this dissertation.

2.3 Extrinsic dissipative processes

2.3.1 Dissipation due to surface loss

Even in perfect crystals, the surface is far from being ideal; it has dangling bonds [46], adsorbed water molecules, micro cracks, dislocations, and randomly oriented grains [44] [57]. In summary, the outer layer of a perfect crystal is in nature polycrystalline, viscous and dissipative [19]. An oscillation in the resonator shifts the thermodynamic balance of the surface; its restoration comes accompanied with heat generation. Although surface loss results from a relaxation process and should be characterized by a Debye peak, the vast plurality of phenomena that contribute to surface loss have different relaxation time constants. Surface loss is better approximated as a frequency independent loss [42], where t is the thickness, E the Young's modulus, E_S the imaginary component of the Young's modulus of the dissipative layer, δ the thickness of the dissipative layer and Q_S the bulk Q-factor.

$$Q_{SURF} = \frac{t}{6\delta}\frac{E}{E^S}\,Q_S \tag{2.6}$$

2.3.2 Dissipation due to air damping

A resonator loses energy to the gaseous medium by generating sound waves. Air damping is circumvented by operating in vacuum. Operating high Q BAW resonators at MHz frequencies require pressure levels in the mTorr range [9] to make Q_{AIR} negligible while low-frequency flexural shells [4] require μTorr levels to cancel Q_{AIR}. There is no closed-form expression for gas friction; however, COMSOL can accurately compute air damping. In general, air damping scales with pressure P, temperature T, the sound velocity in the resonator ν, R the gas constant, the density ρ the mean molecular weight of the gas μ as follows:

$$Q_{AIR} \sim \frac{P}{\rho v} \sqrt{\frac{\mu}{RT}} \tag{2.7}$$

2.3.3 Dissipation due to anchor loss

Anchor loss, also known as support loss, is the radiation of energy from the device to the surroundings through vibration of the supporting structure [58]. It is difficult to express a closed-form expression of Q_{ANC} as the wave that irradiates from the device may reflect on boundaries, cracks or defects and interfere either constructively or destructively with the standing wave inside of the resonator [7]. To compute an estimated value of support loss, it is usually assumed that the surrounding is defect-free, infinite and can be implemented computationally by using a perfectly matched layer (PML) [35]. Under these assumptions, the anchor loss can be computed efficiently in COMSOL.

2.4 Energy trapping to mitigate anchor loss

There exists a broad literature on acoustic engineering to mitigate anchor loss in MEMS resonators. Typically, Q_{ANC} scales with some power of L/W where L is the length and W the width of the anchor [59], [30], [37], [38]. While arbitrarily high Q_{ANC} can be designed with simple high aspect ratio ($L/W>>1$) beam anchors, these devices are extremely fragile and very sensitive to fabrication imperfections. If the beam is not anchoring the device exactly at the nodal point, then Q_{ANC} drops sharply with misalignment. Robustness to fabrication deviations is key in implementing a practical acoustic decoupling scheme. For the sake of brevity, only recent state-of-the-art approaches that rely on energy trapping will be discussed. By trapping the bulk of the elastic energy in the resonator's

body and far from the anchor's region, the following methods circumvent anchor loss without making the resonators fragile or sensitive to finite fabrication precision.

2.4.1 Energy trapping via quarter wavelength reflection

A well-established method to trap energy is to add reflectors around the resonator's anchor (Figure 10). As the acoustic energy leaks from the resonator into the substrate, the wave travels away from the resonator, reflects from the reflectors and travels back to the resonator. Constructive interference occurs when the reflectors are placed a quarter wavelength (of the propagating wave in the handle layer) from the anchor [60]. Since the wavelength scales inversely with frequency, this energy trapping approach is not compatible with low frequency resonators. Further, it reflects only in-plane waves; out-of-plane waves still travel and carry energy away from the resonator.

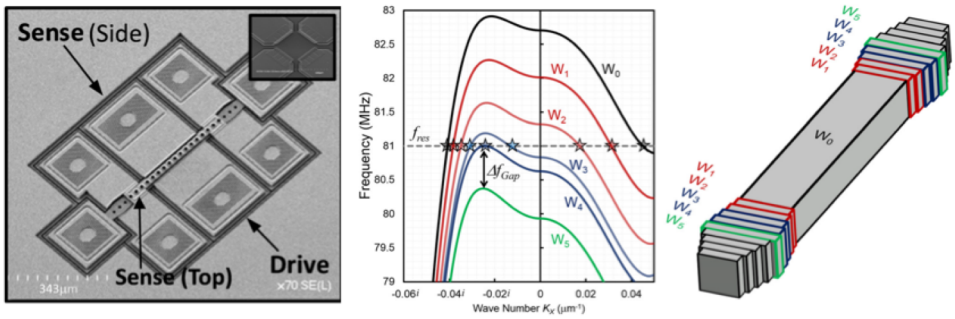

Figure 10: Energy trapping via evanescent wave engineering [61].

2.4.2 Energy trapping via evanescent waves

Acoustically engineered resonant beams (Figure 11, left) benefit from energy confinement to eliminate anchor loss. The width of the anchor is designed such that there is no propagating (green curve in Figure 11, center) nor evanescent wave (blue curve, in

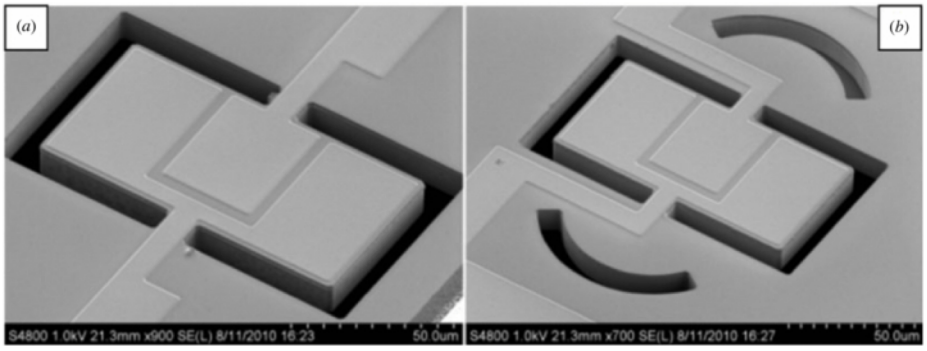

Figure 11: (a) With and (b) without in-plane acoustic reflectors that reduce anchor loss in lateral–extensional MEMS resonator [60].

Figure 11, center) at the synthesized mode's frequency (f_{res}) such that the acoustic energy is trapped in the body of the resonator [61]. Virtual cross-sections of various width are shown in Figure 11, right; fabricated devices have smooth profiles.

2.4.3 Energy trapping via embedded spokes

Another well-established approach consists in selectively removing some precise part of the resonator's body to acoustically isolate the resonator [9], [23]. This approach is

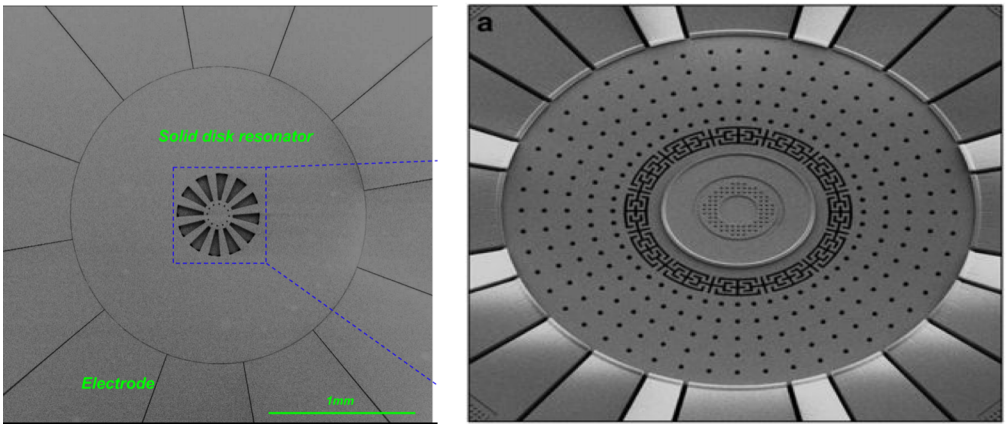

Figure 12: (Left) Substrate-decoupled silicon disk resonators having degenerate gyroscopic modes with Q in excess of 1-million [23] (Right) Substrate-decoupled, bulk-acoustic wave gyroscopes: Design and evaluation of next-generation environmentally robust devices [9].

compatible with resonators that are centrally supported (see Figure 12). The main drawback is that these straight or T-bone shaped spokes introduce thermoelastic damping (TED). While there are some benefits to resonators limited by TED rather than by anchor loss (e.g. record *Q*s in Si for gyroscopic modes near 1.3M), there are other approaches that mitigate anchor loss without sacrificing TED [62].

2.4.4 Energy trapping via curvature discontinuities

This thesis explores two completely disparate methods that traps energy in the bulk of the resonator without imparting additional damping via TED. A first approach consists in trapping the resonant mode in between points of critical curvature. Energy trapping via curvature discontinuities has first been theorized in 1992 by Scott and Woodhouse [63]. They observed that S-shaped chainsaws can produce sounds with remarkable acoustic

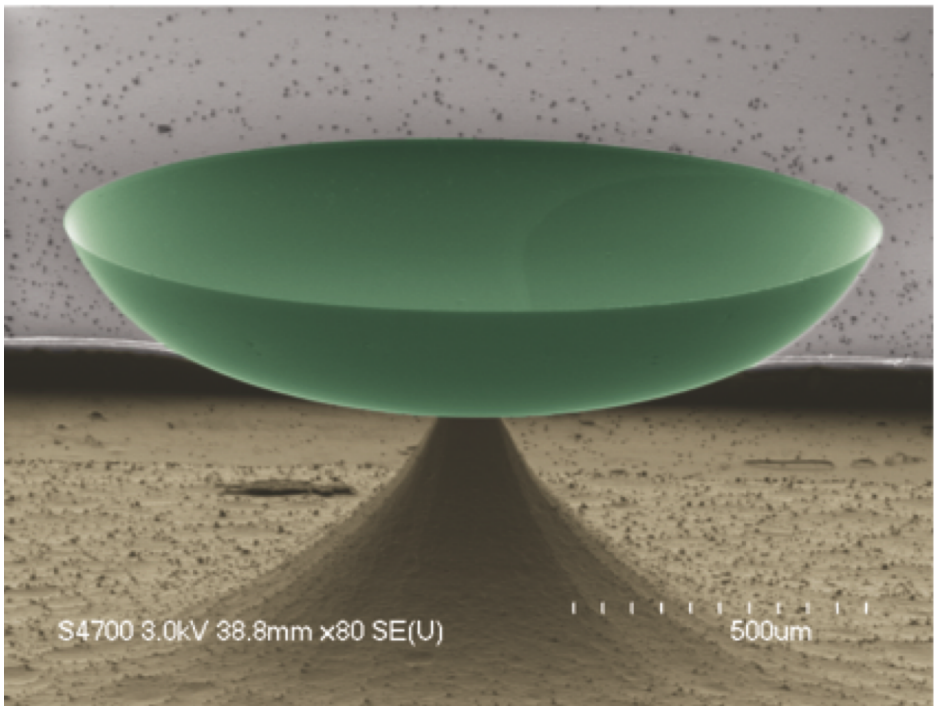

Figure 13: Highly-symmetric SiO_2 SSR with angstrom-level roughness [13].

quality because the sound waves generated by the bow reflect at points of critical curvature and do not dissipate in the anchors. Shell's with nearly discontinuous curvature (see Figure 13) benefit from this approach and will be explored further in this thesis [13], [34], [36].

2.4.5 Energy trapping via Phononic Crystals

A phononic crystal (PnC) is a structure composed of stacked acoustically mismatched layers (superlattice) or a tessellation of periodic inclusions in an elastic medium as shown in Figure 14 [62]. Analogous to a photonic crystal for electromagnetic radiation, the mismatch of acoustic impedance between the layers or inclusions reflects waves, introducing wave interference which creates the band gap of the PnC. Both one-dimensional [64] and two-dimensional PnCs have been demonstrated in the literature. However, in these 2D implementations, the PnCs are in the same plane as the resonator and their efficiency are also limited to in-plane waves (see section 2.4.1). In this thesis, the PnCs are included in a second layer (3D PnC); this novel feature enables to reflect both in-plane and out-of-plane waves and fully isolate the resonator [55].

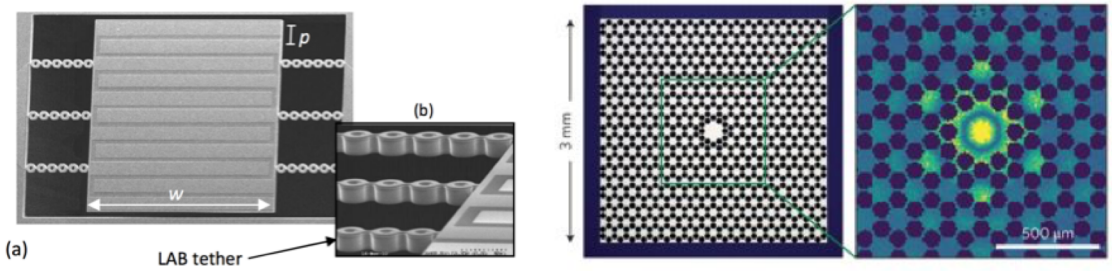

Figure 14: (Left) One-dimensional linear acoustic bandgap structures for performance enhancement of AlN-on-Silicon micromechanical resonators (Right) Ultra-coherent nanomechanical resonators via soft clamping and dissipation dilution [33].

2.5 Summary of dissipation mechanisms investigated in this thesis

Theoretically, dissipation is bounded by quantum-based mechanisms including thermoelastic damping and phonon-phonon damping. Practically, dissipation is bounded by surface loss, surface TED, viscous damping and in general by anchor loss. Recent progress, and particularly in the field of phononic crystals, made it possible to make various extrinsic mechanisms negligible compared to the intrinsic mechanisms for SiN resonators [33]. The key to reach the fundamental limit in SiN resonators was to induce tensile stress; this path towards ultra-high *Q*s is not available in single-crystals such as Si and SiC. As a result, there has so far been no Si resonator which *Q* is limited by Akhiezer damping, although some resonators are inching towards this fundamental limit [26].

CHAPTER 3. 3D SHALLOW SHELL RESONATORS

3.1 Shallow shell resonators limited by surface loss

3.1.1 Introduction

The HRG sets the 'gold standard' among acoustic gyroscopes with its simple and robust design while boosting *Q*s greater than 20M without any failure after over 1M hours of operation hours [2], [3]. However, the fabrication process of the HRG does not lend itself to miniaturization [4]. One key challenge of miniaturizing the HRG (μHRG) is to maintain its incredibly high *Q* factor while scaling down each dimension by more than 10X [13]. As seen in Figure 3, this is no simple task. In the kilo-Hertz range, Akhiezer damping is not a considerable source of damping (see 2.2.1). TED is minimized by using thermally-grown wet SiO_2 as the structural material because of its near-zero CTE. Air damping is negligible because of vacuum operation. The most significant losses in μHRGs are support loss and surface loss; these losses need to be estimated and mitigated. In brief, in this thesis, the author has been able to minimize anchor loss and shows experimentally that surface loss remains the most significant loss mechanism [34].

Anchor loss in high-frequency resonators (f≥100kHz) can be simply estimated by using the Perfectly Matched Layer (PML) method in any modern FEM (e.g. COMSOL) software for high frequency resonators (*f*≥100kHz) [35]. For Si BAW disk gyroscopes, the PML estimation is only a factor 2 away from measurements [9]. However, for high-aspect-ratio resonators operating in the low kilo-Hertz range, there is over 6 orders of magnitude

between the critical dimension of the shell (typically < 1μm) and the wavelength (typically > 1m). This discrepancy poses several challenges that have been discussed already for shells 100 times thicker than shells considered in this work [7]. When a micron thick shell is drawn on a meter thick PML, COMSOL directly considers the shell to be part of the geometrical error and the shell is not well represented. When drawn appropriately, the shell requires a meshing that is so fine compared to the PML that it overloads the author's computer's GPU. Therefore, numerically estimating anchor loss and ultimately confirming that anchor loss is negligible in low-frequency low-stiffness shells is challenging. This thesis presents a host of evidence, including both simulated and experimental, that validate that anchor loss is negligible in the fabricated shells.

Surface loss is a loss that becomes more and more dominant as dimensions shrink and the surface-to-volume ratio increases [32]. Further, surface loss depends on the thickness of the damaged layer that surrounds the resonator [19]; this layer can be cleaned away in macroscopic stiff shells [21]. Miniaturized low-frequency shells are extremely fragile and cannot be immersed without being broken, hindering any post-fabrication cleaning, making surface loss particularly challenging to address.

This chapter provides the experimental evidence that anchor loss can be circumvented to a large extent in micro-mechanical resonators and that surface loss is currently limiting the overall *Q*-factor of low-frequency low-stiffness SiO_2 μHRGs.

3.1.2 Acoustically-isolated 3D resonators in music

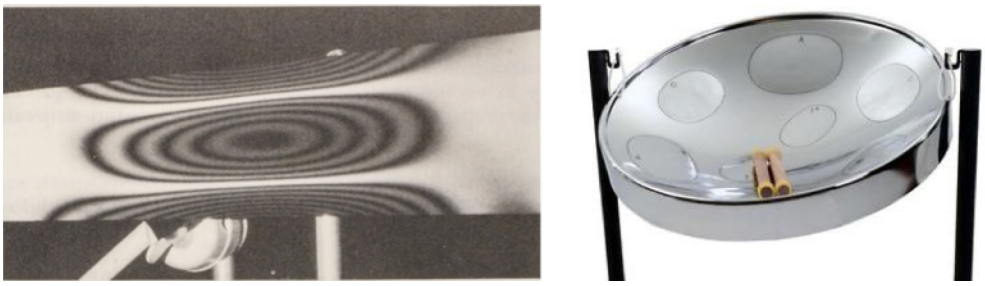

Figure 15: Musical instruments with varying curvature that confine lightly-damped resonant modes, with left a musical saw and right a Caribbean drum [63].

In a landmark paper in 1992, Scott and Woodhouse analyzed the musical saw phenomenon as shown in Figure 15 [63]. When sufficiently bent as to form an S shape, an otherwise damped saw when straight, produces a lightly damped mode of vibration. When bent beyond a certain degree of curvature, the points of inflexion of the S shape confine the mode of vibration, isolating it from the dissipative anchors. Various tones can be played from the musical saw between the inflexion points and locations where the bow touches the saw (see Video of musical saw playing Ave Maria).

Similarly, Caribbean drums produce lightly damped sounds owing to mode localization due to points of critical curvature. Since the resonance modes are localized within each cavity, multiple cavities producing separate tones can be carved into the same drum without cross-coupling (see Video of Caribbean drum playing various lightly damped modes in a single drum).

These instruments reveal an interesting approach in mitigating anchor loss. Separating the anchor from the body of the resonator via points of critical curvature ensures efficient acoustic isolation. This approach is simple, does not introduce thermo-elastic damping but requires a 3D fabrication approach that controls the out-of-plane curvature of

the resonator. Novel 3D-fabrication approaches have been recently developed in the MEMS community [22] [13].

3.1.3 Various iterations of substrate-decoupled shell resonators

SiO_2 is chosen as the structural material for its low CTE near 0.5ppm/°C, which is 10X smaller than that of polysilicon, translating to approximately 100X improvements in Q_{TED}. Further, high-quality SiO_2 can easily be thermally grown from silicon molds and if these molds are smooth, then SiO_2 shells can be mirror finished with roughness in the single digit angstrom range. Various designs to mitigate anchor loss have been explored (see Table 2). Making the shells shallow concentrates the strain energy far away from the

Table 2 Energy prone to be lost for different structures [36]

Support Structure		Fabricated samples	Estimated Q_{ANC}
Hemisphere	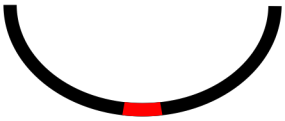	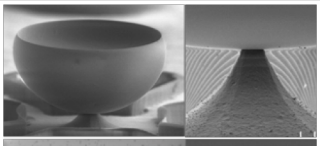	1.85k
Shallow		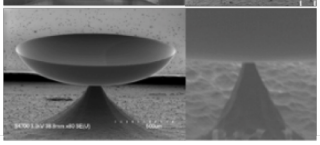	58.2k
Hemisphere w cylinder	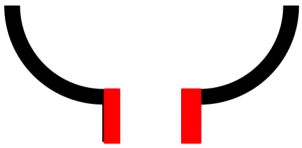	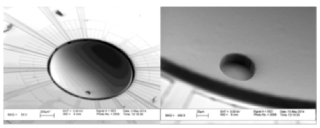	4.8M
Shallow Pierced		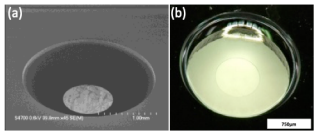	31M
Hollow Cylinder	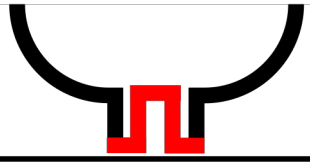	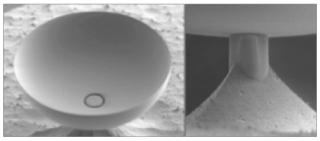	90M

pedestal as it will be discussed in the upcoming sections. In this work, for sake of brevity, only pierced shallow shell resonators and shallow shell resonators on a hollow cylinder are discussed for their potentially very high Q_{ANC} and Q_{TED}.

3.2 Fabrication of high *Q* shell resonators

Fabrication of mirror-finished SiO_2 shells have been published elsewhere [13]. Figure 16 shows the most significant steps. Step 1: 500µm-thick (100) Si wafers are purchased from Ultrasil®. Nearly 3µm-thick low-stress silicon nitride (SiN) is deposited using the nitride furnace. The regular dielectric etch recipe in Vision RIE 1 is used to pattern the SiN hard mask as well as inflict some damage on the surface of the Si layer. Introducing damage in the Si layer improves the quality of the following wet etch step. Indeed, in step 2, wet etching is used to isotropically etch Si molds. If the top of the Si wafer remains intact, then the wet etching steps starts at random locations which translates into roughness. Damaging

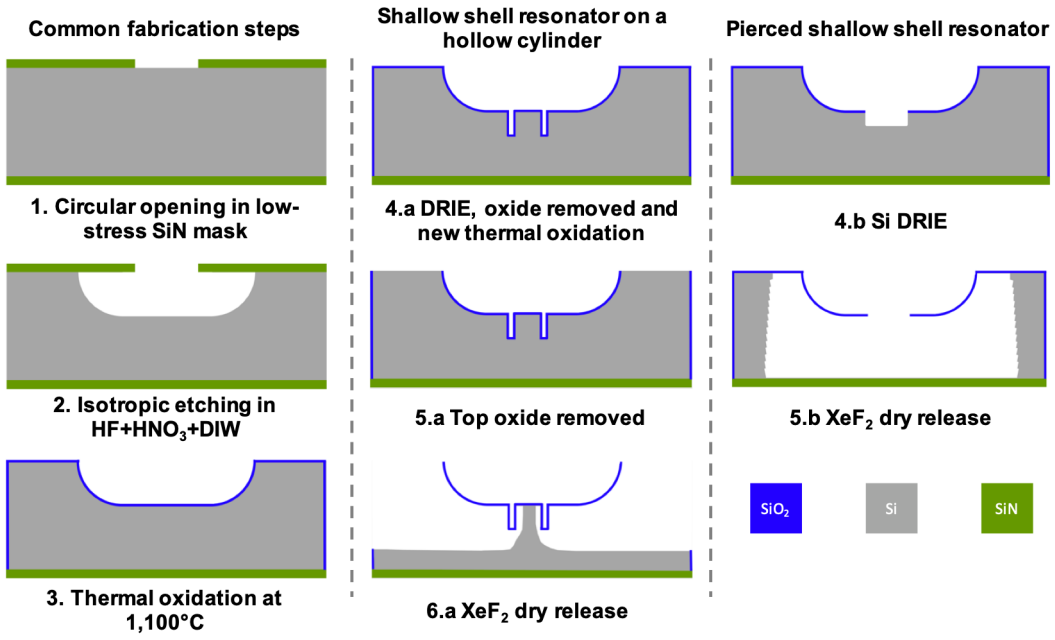

Figure 16: Schematic of fabrication process of shallow shell resonators

the surface layer enables to make the wet etching step more uniform and the resulting Si molds smoother. At the end of step 2, axisymmetric molds with atomically-smooth surfaces are carved out of the Si layer. The depth of the molds is around 300μm and the diameter around 1.2mm. For reasons explained later on, it is key for the bottom of the molds to be as horizontal as possible. In step 3, SiO_2 is thermally grown from the Si molds. In variant fabrication processes, at this step LPCVD TEOS can also be deposited. In fact, about any material that is selective to XeF_2 can be deposited at this step. For our purposes, only materials with low CTE have been investigated for the purpose of achieving high Q_{TED}. The next steps are specialized depending on the aspect of the pedestal. For shells that are anchored by a self-aligned high-aspect-ratio pedestal, the top SiO_2 is CMP'ed and then Si is removed in XeF_2. Removing the top SiO_2 layer without damaging the shell resonator is particularly tricky. Also, XeF_2 etch rate on Si is hard to control due to a lack of microscope installed on the Xactix XeF_2 etcher. Often, shells are over-released and fall from the pedestal despite careful releasing. On the other hand, resonators that are anchored at the top do not suffer from the same drawbacks and can be released in batch without any significant challenges. It is worth noticing that all the shells in this work share the same Si mold as well as the same structural material (thermally-grown SiO_2, LPCVD TEOS) and the same thickness (1 to 2.7μm) such that surface loss that will be discussed later is equivalent in all shells hereinafter considered.

3.2.1 Multi-surface shell resonators: a path towards acoustic isolation

The aforementioned musical instruments demonstrate that points of critical curvature define a region of the resonator that is acoustically isolated from the rest of the

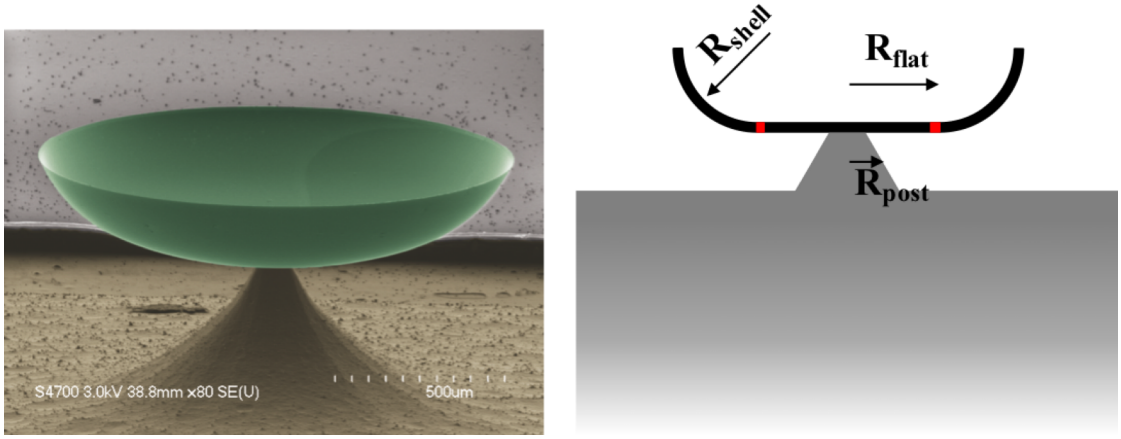

Figure 17: Shallow shell resonators are an approximation of multi-surface shells in which curvature is discontinuous. The points of discontinuous curvature confine the elliptical resonant modes far from the dissipative anchor.

body of the resonator, and particularly from the dissipative anchor points. Building up on this observation, the author has decided to demonstrate that MEMS-scale multi-surface shell resonators are acoustically isolated due to their discontinuous curvature [13]. In practice, only axisymmetric oblate shell resonators have been fabricated in this work; they approximate multi-surface shell resonators. These oblate shells are named shallow shell resonators (SSRs) due to their ellipsoid nature which confers them shallowness, in the mathematical sense of the word shallow. While mathematically correct, a more descriptive name would have been birdbath resonators but the name has already been taken [11].

For the sake of the discussion, the author assumes that the shallow shell is in fact multi-surface. The center region with infinitely large radius of curvature is named the flat region, of radius R_{flat}. The exterior region with finite curvature is named the shell region,

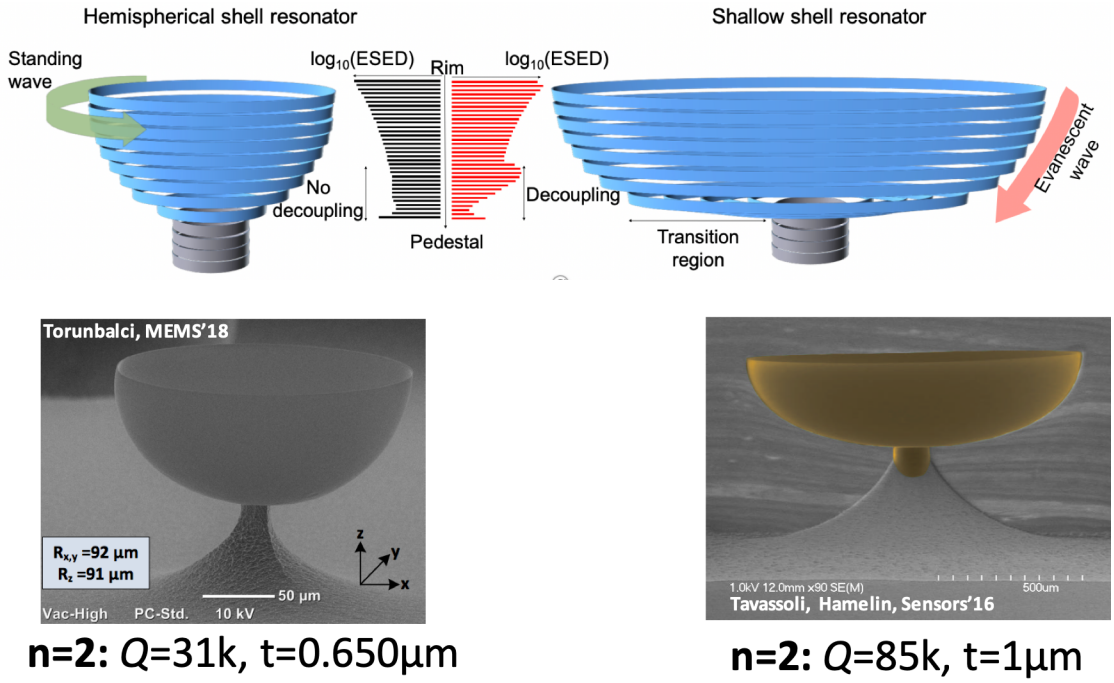

Figure 18: (top) Plotting the elastic strain energy density (ESED) in fictitious rings across the cross-section of hemispherical and shallow shell resonators indicate that ESED accumulates in the shallow shell at the junction of the curved and flat sections. This accumulation of ESED in the shell and depletion of ESED near the pedestal is a result of the unique out-of-plane curving profile of the shallow shell resonator. As a result, shallow shell resonators exhibit the highest *Q*s among published SiO_2 shell resonators (bottom).

of radius R_{shell} (see Figure 17). The points where these two regions meet are points where the curvature is discontinuous and as such provide acoustic isolation between the two regions. In practice, the curvature in the shells is slowly varying, making it difficult to pinpoint separate regions as function of their curvature. As the shallow shell becomes more and more shallow, the strain energy density concentrates near the points of discontinuous curvature, making the shells more and more acoustically isolated (see Figure 18). As an example, frequency splits between degenerate modes that are generated by pedestal imperfections are monotonically decreased with increasing R_{flat}.

As R_{flat} increases and strain energy is progressively concentrated near points of critical curvature (Figure 19), the strain energy is progressively depleted at the shell-pedestal junction. This depletion shows that the shell becomes more and more acoustically isolated. Interestingly enough, when R_{flat} reaches a critical radius $R_{critical}$, the confinement

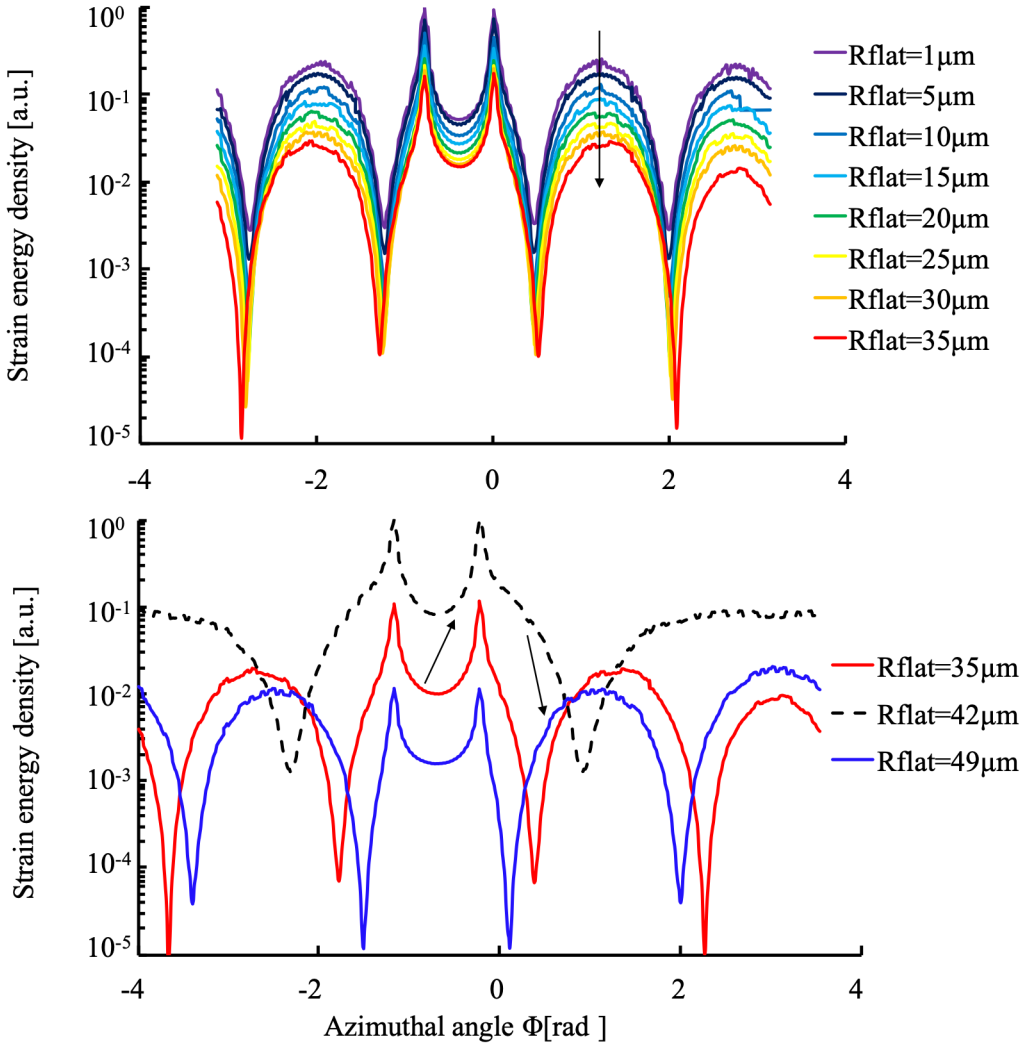

Figure 19: (top) While energy confinement in shallow shells deplete the shell-pedestal junction of strain energy with increasing Rflat (the curves shift downwards), the mixed eigenmodes remain mixed in the absence of anticrossing (the relative aspect of the curves stays unchanged). (bottom) While strain energy density increases during anticrossing, the downward shift and the reduction of the peak-to-peak difference indicate mixed eigenmodes are partially unmixed via veering.

effect becomes even more pronounced. The critical radii $R_{critical}$ are defined by frequency crossings. As R_{flat} increases, the shell becomes progressively less stiff. The decrease in stiffness of the rocking modes and the breathing mode is faster than for the n=2 modes of interest. Because these frequencies decrease at disparate rates, the frequencies cross (Figure 20). These frequency crossings do not occur in the counterpart hemispherical resonator when the shell's radius is increased continuously.

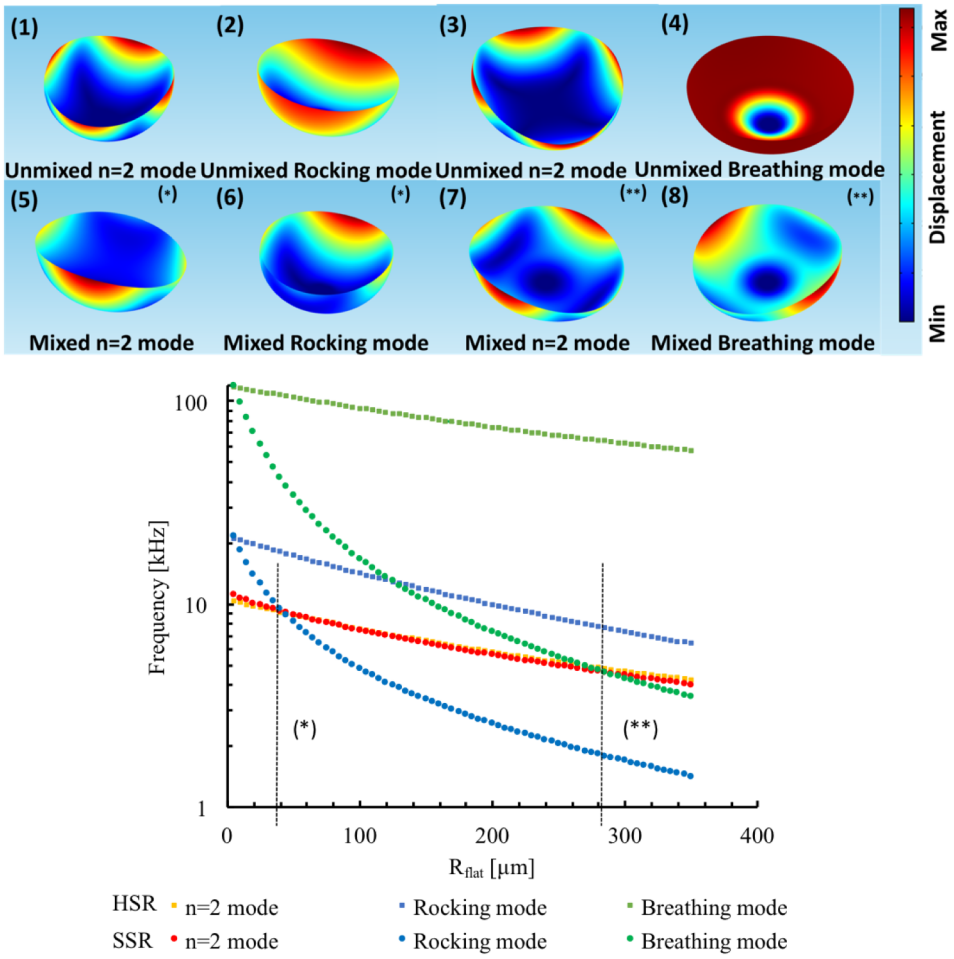

Figure 20: (Top) Modes near (mixed) and far (unmixed) from frequency veering points that are indicated in * and ** in the (bottom) graph which depicts frequency crossings is present in shallow shell resonators and not in the counterpart hemispherical shell resonator.

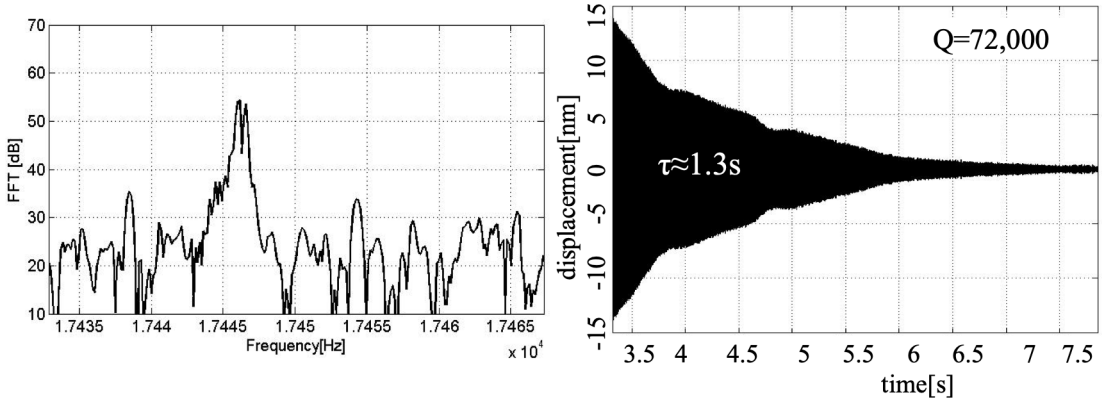

Figure 21: (bottom left) Increasing the radius of the transition region Rflat in shallow shells (or the radius of the hemispherical shell), the n=2 frequency split decreases dramatically after frequency crossings. (bottom right) Experimentally, shallow shell resonators exhibit minute frequency splits when the transition region is large enough to ensure one or two frequency crossings.

At these frequency crossings, modes veer. Mode veering is the key feature that allows the strain energy density to decrease significantly with increasing R_{flat} in shell resonators (Figure 20). Deriving a close-formed formula that relates strain energy density to frequency separation is particularly complex and as not been attempted in this dissertation. However, frequency splits as small as 1Hz are routinely measured in these symmetric resonators (Figure 21).

3.2.2 Experimental validation of anchor loss mitigation in shallow shell resonators

As discussed in reference 17, it is particularly challenging to accurately simulate anchor loss in low-frequency low-stiffness shell resonators owing to the 6 orders of magnitude difference between the critical dimension of the shell and the wavelength of kilo-Hertz sound waves in silicon. Nonetheless, the author and Dr. Tavassoli have assumed that anchor loss can be simply approximated by taking the ratio of strain energy in the body

of the resonator to the strain energy in the pedestal. While this ratio does not capture the physics of anchor loss like a PML, it does provide a trend and a way to compare different anchor designs. One can observe that shallow shells are better decoupled than

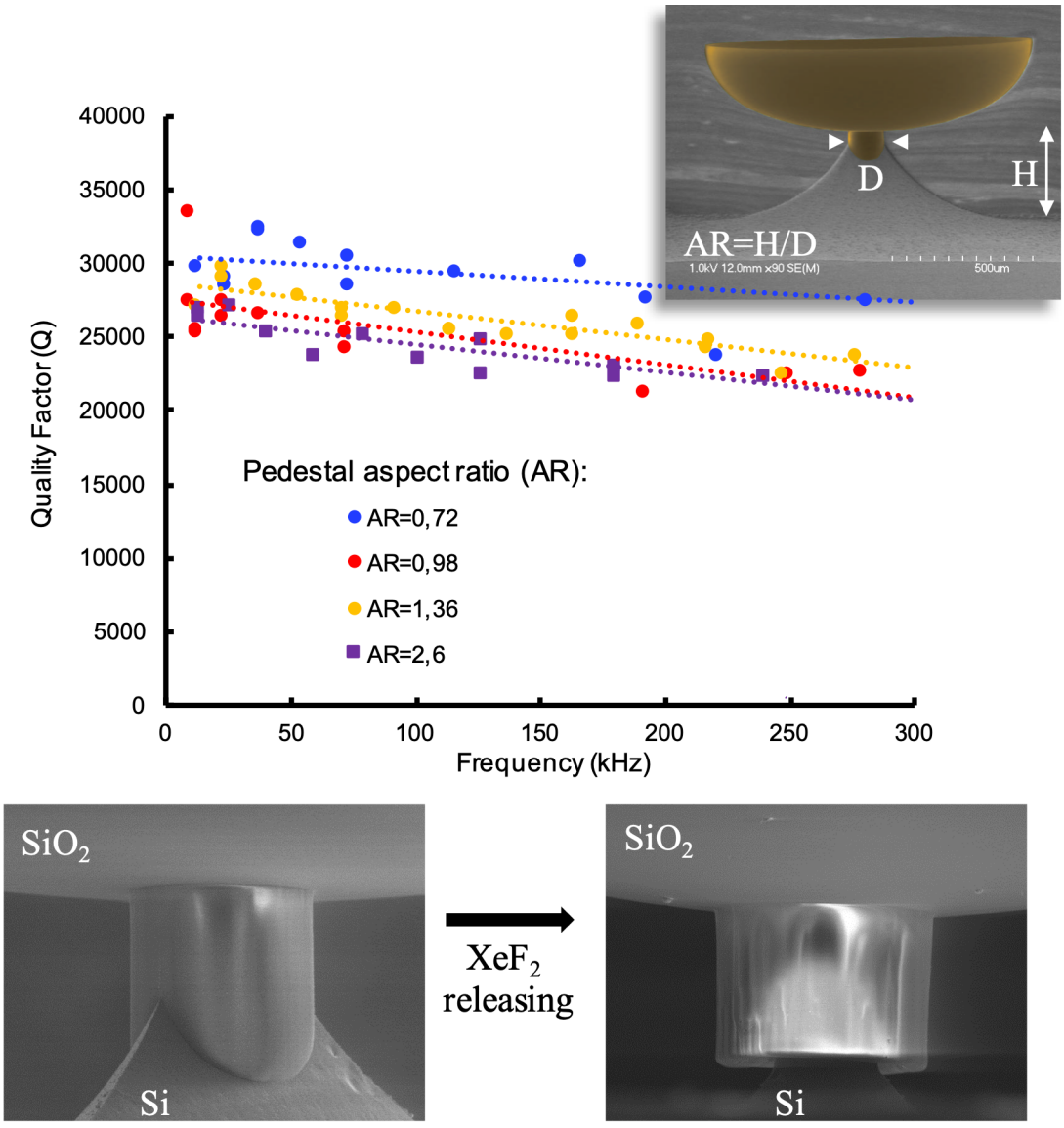

Figure 22: (Left) Shallow shell resonator anchored on a modular hollow cylindrical pedestal (right) Despite multiple releasing steps which monotonically increase the aspect ratio of the pedestal, the quality factor of all the sub-300kHz modes remain unaltered, thereby indicating that anchor loss is not a significant damping mechanism. (bottom) SEM of a device showing the diameter of the pedestal reducing during releasing.

hemispherical shells owing to the points of critical curvature that isolate the resonating shell from the dissipative anchor. The pedestal can be further engineered to add a second decoupling layer. Various pedestals designs are shown in Table 2. If the assumption that the ratio of strain energy approximates anchor loss, then the shallow shell resonator with a

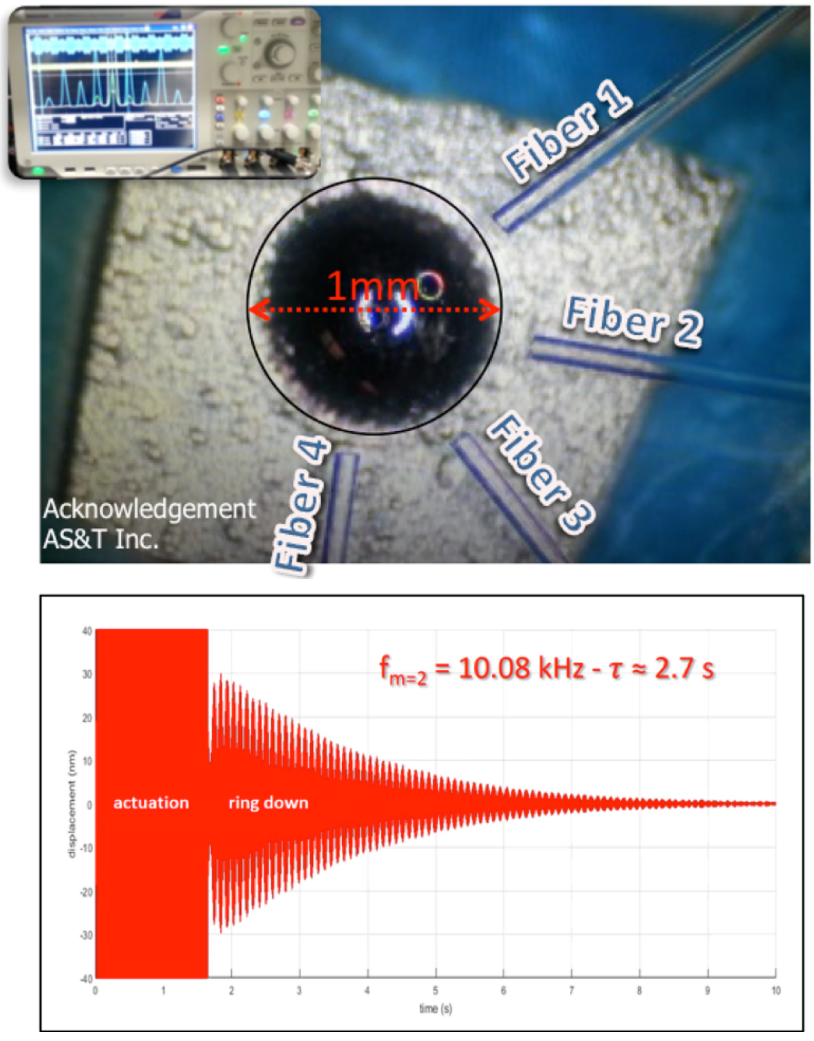

Figure 23: (top) The four-channel fiber optics conformal vibrometer setup at Advanced Sciences and Technologies (AS&T) used for the SiO_2 micro-shell resonator characterization in vacuum. [36] (bottom) Decay time of an oxide shell resonator with hollow cylinder support (thickness=1μm and diameter=900μm). The frequency of m=2 mode is 10.08 kHz and the decay time is 2.7 sec. (Q ~ 85,500)

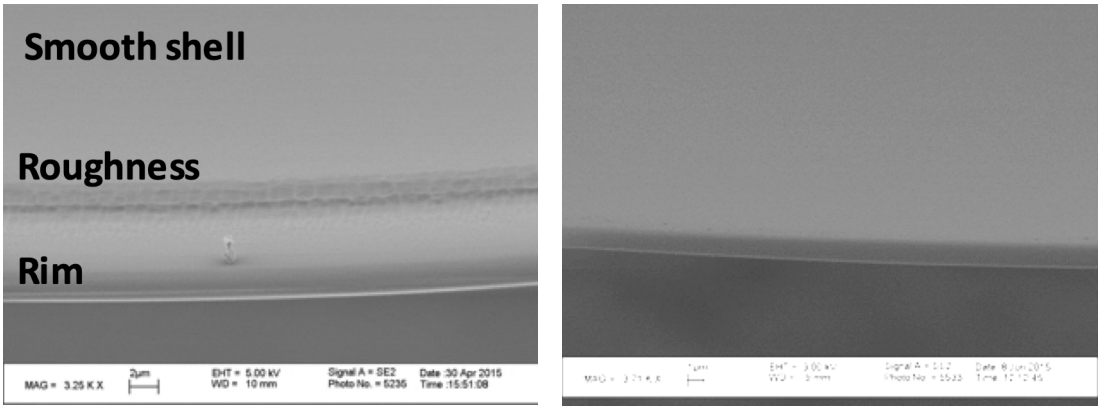

Figure 24: Effect of rim quality: (a) SEM of low quality and (b) high quality rim. [36]

downward hollow cylinder pedestal should have a much higher Q_{ANC} than the shallow shell resonator, if anchor loss is the dominating damping mechanism.

To verify if anchor loss is not the dominating damping mechanism in shallow shell resonators with a hollow cylinder, the frequency spectrum has been recorded multiple times throughout releasing (Figure 22). As the shell is progressively dry released in XeF_2, the anchor's aspect ratio increases, and with it so should Q if anchor loss is the limiting damping mechanism. Since the Qs of all the modes of frequency below 300kHz are not anchor loss limited.

The highest Q measured in a pedestal-supported shell resonator is 85k at 10kHz, far from the 26M of the HRG. The discrepancy between various Q measurements in various shells is sought to stem from the quality of the rim. A rough rim (Figure 24) reduces Q to around 30k while devices with a smooth rim have Qs in the 70 to 80k range [65] (Figure 23). While anchor loss has been mitigated by introducing points of discontinuous curvature

and the engineered pedestal, surface loss becomes a viable candidate as the limiting damping mechanism.

3.2.3 Limiting damping mechanisms in shallow shell resonators

The Q-factors of all the modes of a pair of shallow shells anchored on hollow cylinders are reported in Figure 25. For frequencies below 700kHz, the curve Q vs frequency follows nearly perfectly the fit Q=20k. This is a relatively low Q since in this

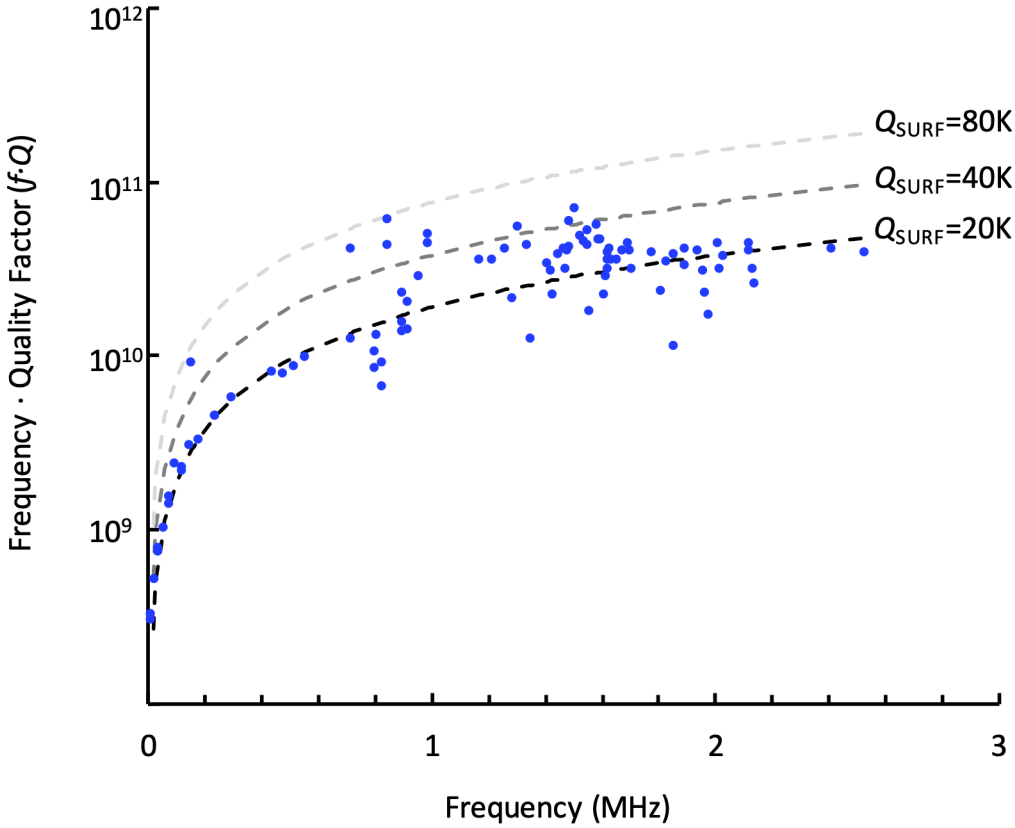

Figure 25: Typical behavior of a high Q pierced shell resonator: surface loss limits Q. The fit to Q_{SURF}=20K is excellent below 700kHz; at higher frequencies, we observe that the Qs spread out, indicating possibly that surface defects might load Q differently for disparate resonant modes. Qs below the 20K line might be loaded by anchor loss.

range we have already measured *Q*s near 80k. Interestingly, at higher frequencies, we measure a wide spread in *Q*, up to 80k. This indicates possibly that non-uniform surface effects might load Q_{SURF} disparately [46] . More measurements with higher Qs in the low frequency range are necessary to distinguish the underlying limiting dissipation mechanisms.

To study surface loss, a large number of shells need to be tested. For this purpose, pedestal-supported shells are not adequate. Indeed, the releasing step in which the pedestal is defined by dry etching the sacrificial Si is particularly cumbersome. Any over-etch makes the shell too fragile. This limitation is key in part because the etching of Si by XeF_2 is purely chemical. Thus, the etch rate is extremely sensitive to the amount of exposed Si and to the placement of the die in the chamber. Etch rates are not repeatable enough to release shells precisely. Therefore Dr. Tavassoli came up with idea of the pierced shallow design described in the following section; all work presented is by the author of this thesis.

3.3 Surface loss-limited pierced shallow shell resonator

3.3.1 Introduction to pierced shell resonators

Anchoring the shells via a high-aspect ratio pedestal presents many limitations that limit the fabrication yield. Instead of anchoring the shell at their flat bottom, the shells can also be anchored at the top (Figure 26). This new anchoring strategy enables to over-release the shells in XeF_2 with ease. The only limitation is that, if the over-etch is very significant, then the SiO_2 layer might crack or break-off; however, even in that case the shells are still firmly anchored to the substrate. Discarding one lithography step, the pierced shell and the

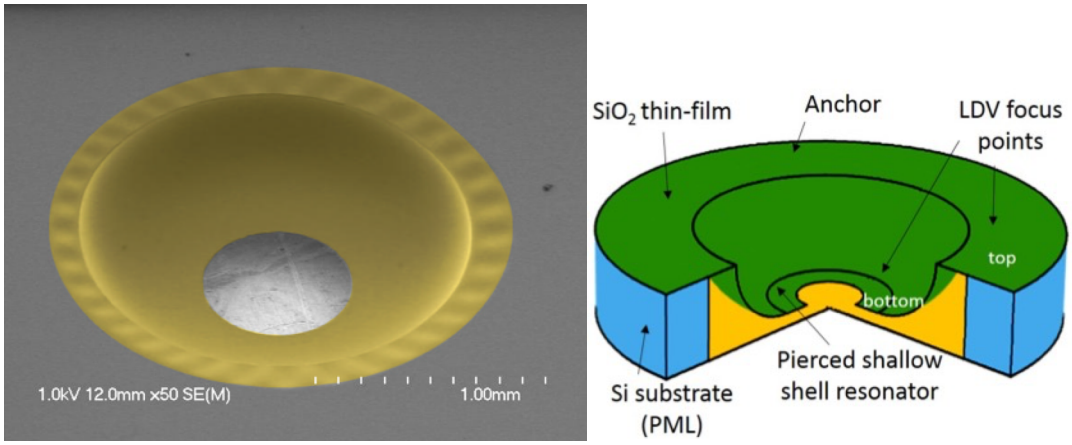

Figure 26: (Left) Colored SEM of a pierced shallow shell resonator that has been over-released, which is revealed by the wrinkles near the top anchoring section that are due to compressive stress. (right) Cross-section diagram of a pierced shell showing locations where optical measurements are taken at.

shallow shell share the exact same fabrication process described later on. As a result, these shells have the same surface loss and thus the same quality factor if anchor loss is also negligible in pierced shell resonators.

3.3.2 Anchor loss in pierced shell resonators

Pierced shells are low-stiffness low-frequency resonators as shallow shell resonators and are thereby equally challenging to simulate their anchor loss using PML. Contrary to shallow shell resonators, pierced shell resonators can be easily probed optically as both the anchoring region and the region of the shell with the largest displacement both face the same upward. LDV measurements reveal that the n=3 displacement is so small that it is below the noise floor (near 1ppm) of the LDV (Figure 27). This indicates that the n=3 modes are indeed localized and trapped in the shell, far from the dissipative anchor;

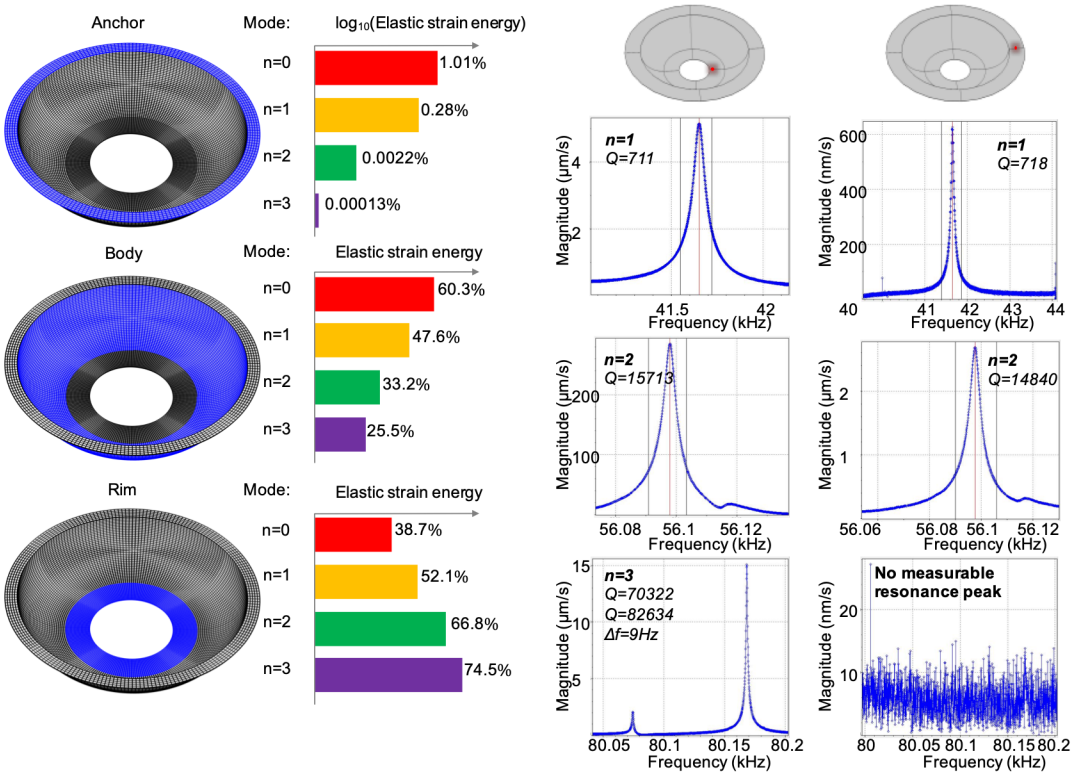

Figure 27: Laser Doppler Vibrometry (LDV) measurements reveal over a 1/100th reduction of the out-of-plane (OOP) displacement w of the n=3 elliptical mode between the resonating rim and the dissipative anchor of PSSRs, proving energy confinement of n≥3 modes. Finite element simulations (left) confirm the LDV measurements.

the n=3 and higher order modes are immune to anchor lossc and should be surface loss limited.

3.3.3 Surface loss in pierced shell resonators

Numerous SiO_2 and TEOS shells have been produced to study surface loss (Figure 28). It is noteworthy to point out that these measurements have been done over 2 years after fabricating and first testing these shells. The highest *Q* measured in this 2-year interval are basically the same, noting barely a 10% decrease from 96,000 to 84,000. All sub-1 MHz modes have been measured in 20 shells, and then truly surface-loss limited resonators

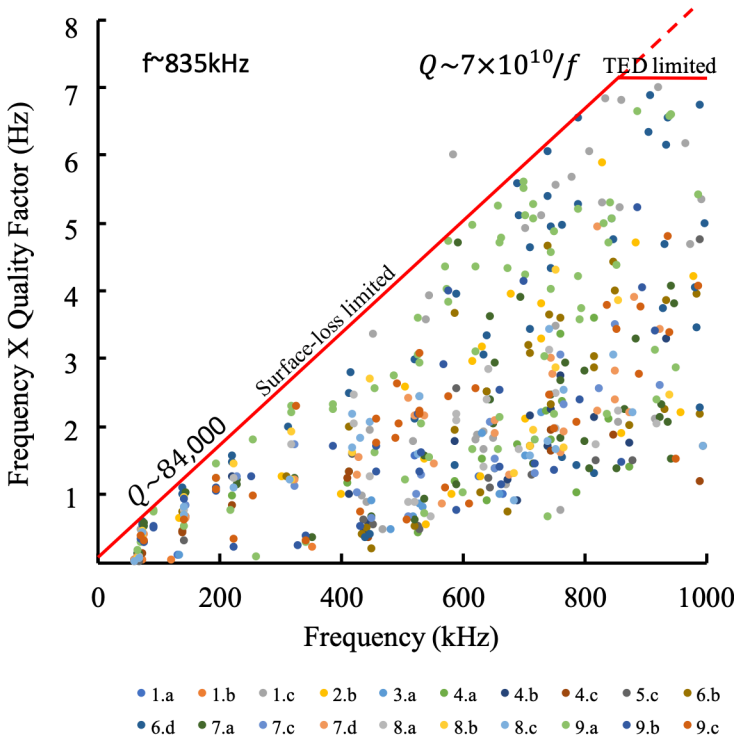

Figure 28: Collective behavior of 20 pierced shells up to 1MHz.

have been measured up to 3MHz (limits due to the piezo-stage not transducing properly beyond 3MHz). It appears that a surface loss limited shell has a constant Q behavior up to 1 MHz and then in between 1 and 3MHz a constant fQ behavior. This indicates that beyond a certain frequency (near 2MHz), far from the frequency range of interest (sub-100kHz), surface TED becomes a dominant loss mechanism.

3.3.4 Engineering surface loss in pierced shell resonators

Pierced shell 8a is used as a reference shell (Figure 29). It is annealed in a RTP chamber for 5min and the quality factors of all the modes below 1MHz have increased in averaged by about 50%. 4 shells on the same single die have then been exposed to various plasma conditions; it is clear that plasma exposure induces surface loss. Even thermal

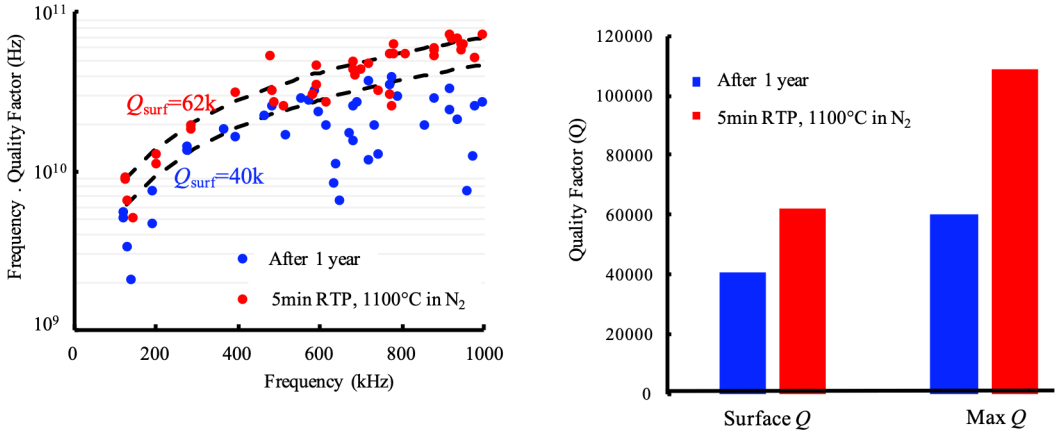

Figure 29: Thermal annealing improves both the average Q and the maximum of sub-1 MHz modes in pierced shell resonators.

annealing does not suffice to recover the Q-factor degradation due to plasma damage. As a result, it is likely that the main source of surface loss in pierced shell resonators is surface damage due to exposure to plasma (Figure 30). Reducing plasma exposure and thermal annealing can both improve surface loss by a factor near 2, which is consistent with previous literature on surface loss [43].

3.3.5 Comparison with literature

Wet-etched SiO_2 shell resonators, anchored upon a pedestal or at the top, are limited by surface loss. Interestingly, other shells with greater or reduced stiffness, exhibit respectively greater or smaller Q-factors. Therefore, to date, the lowest damped shell resonators are limited by surface loss regardless of the fabrication method or of the choice of structural material (Figure 31). Moving forward, and without degrading TED, higher Qs could be achieved by migrating to materials that are impervious to surface loss because they are chemically inert like SiC. Because of processing challenges, SiC shells have not

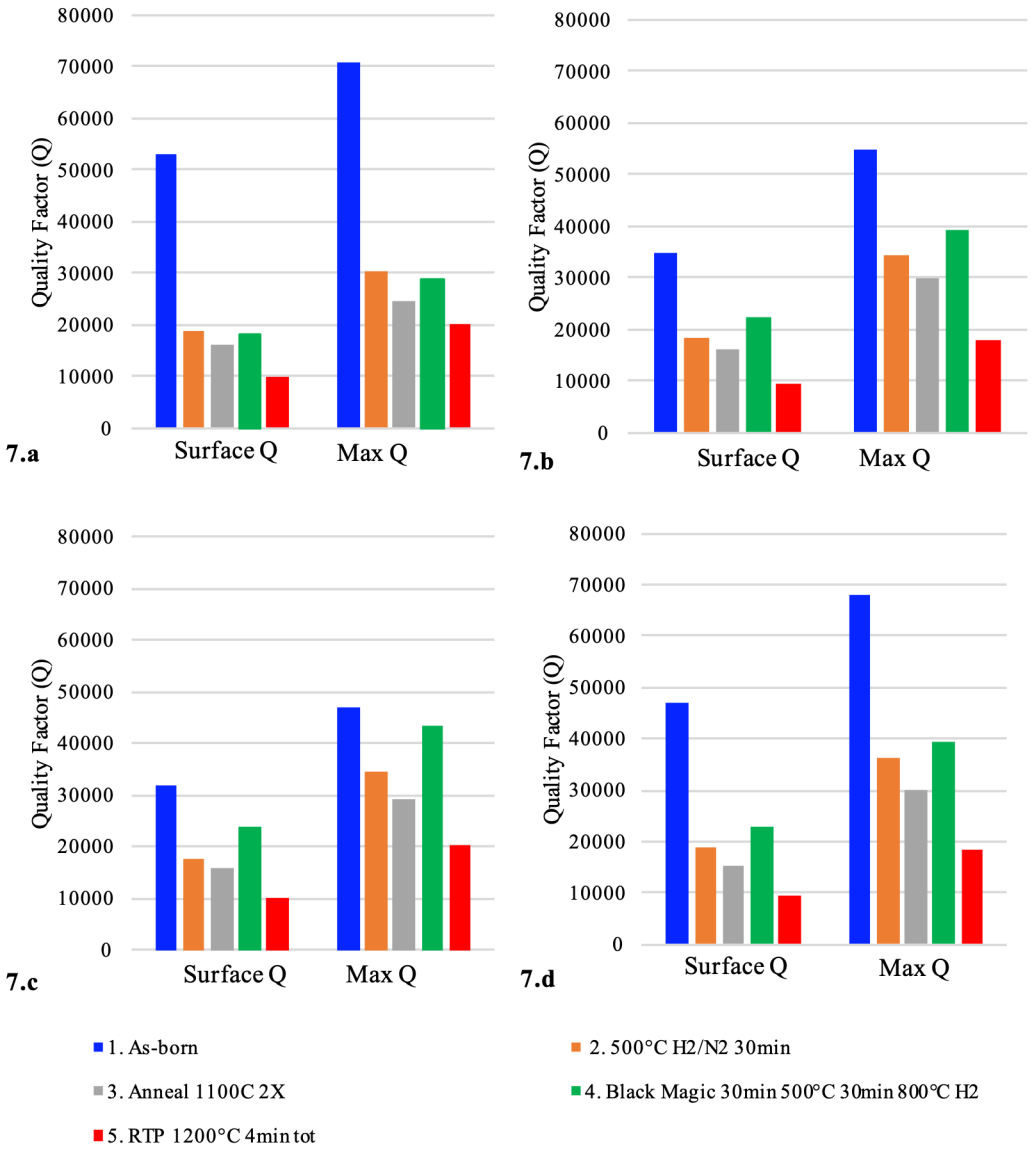

Figure 30: Exposure to plasma degrades surface loss permanently, even thermal annealing after plasma exposure degrades surface loss. Achieving higher *Q*s in low-frequency low-stiffness shells require lesser exposure to intense plasma and more thermal annealing.

been investigated in this thesis, only 2D geometries. Reverting to 2D geometries enable to improve surface loss by decreasing the surface to volume ratio. Future work may focus on fabricating ultra-high SiC shell resonators.

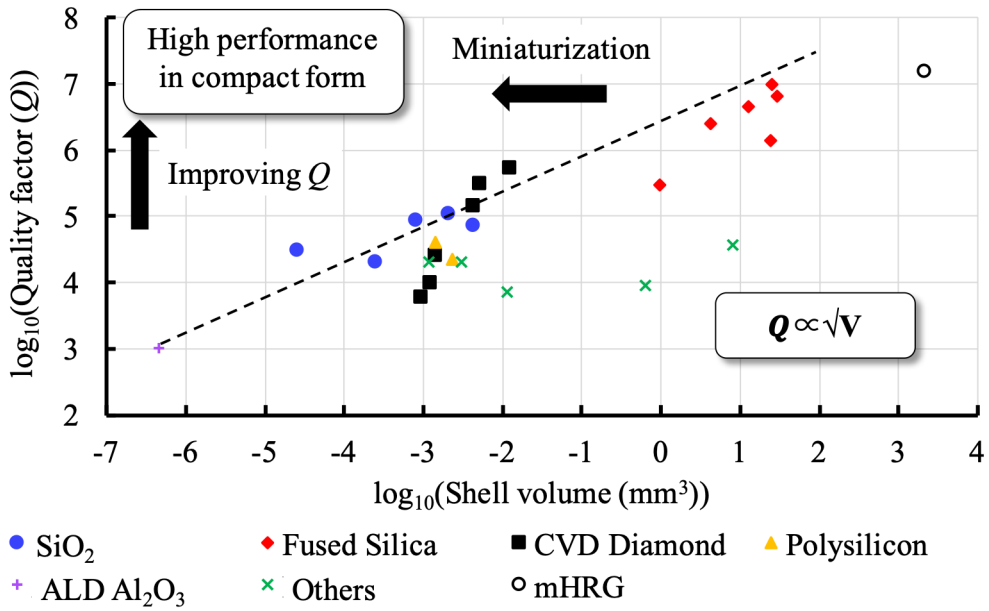

Figure 31: Q factors of low-frequency shells scale with the shell's thickness and more generally with the shell's stiffness

CHAPTER 4. ULTRA-HIGH-*Q* SIC BAW DISK RESONATORS

4.1 Background on SiC MEMS

4.1.1 SiC, a promising MEMS material

The chemical inertness and large Young's modulus (E=400GPa) render SiC immune to surface loss especially when micro-machined into a disk resonator with ultra-smooth surfaces and low surface to volume ratio (Table 4). SiC is not only immune to surface loss, it displays lowest amounts of phonon-phonon damping (Akhiezer damping,

Table 3: Material properties of 4H-SiC vs (100) Si

Property	(100) Si	4H-SiC
Density [kg/m^3]	3230	3216
Young's modulus [GPa]	130-169	500-550
CTE [μm/m·K]	2.6	3.15
Resistivity [Ω.cm]	>0.001	0.02
Wafer bonding fabrication	✓	✓
Nanogap fabrication	✓	✓
***f.Q* [10^{13} Hz]**	**2.3**	**64**

2.2.1) in the MHz regime. Since SiC is a wide-band gap semiconductor, robust SiC-based electronics can be integrated around the SiC MEMS device which enables ultra-high performance in harsh environments and ultra-low power sensors and particularly inertial sensors. Therefore, SiC can replace advantageously Si as a platform for ultra-high performance MEMS sensors for harsh environment applications. This thesis tackles two hurdles that must be overcome before SiC can be widely used: wafer-level SiCOI fabrication and SiC DRIE. Once these hurdles overcome, SiCOI substrates with nanoscale gaps will be a versatile technological platform for the realization of capacitively-transduced MEMS sensors. To this date, only surface micro-machined SiC MEMS resonators have been published due to the above limitations. Only one bulk micro-machined SiC gyroscope has been published [56]; however, this device uses flexural gyroscopic modes which are low *Q* by essence, thereby not using SiC to its full potential (see 2.2.2). Indeed, flexural modes in SiC resonators are crippled by TED because the frequency of operation is near the Debye peak. In practice, SiC resonators are free from TED only in the adiabatic regime (MHz range) in which only the BAW modes live in at MEMS scale.

4.1.2 State-of-the-art SiC resonators

Because bulk micromachining of SiC is a nascent field, nearly all the published resonators are surface micromachined, with thicknesses less than 5-7μm. Because of this thickness constraint, only flexural resonators have been published to the exception of one paper that investigated bulk acoustic wave in SiC at the gigahertz range [66]. As a result, although SiC is promised to deliver higher *Q*s than Si by a factor near 60, no paper so far demonstrates *Q*s in SiC that even reach that of Si (Figure 32). Prior this thesis, the highest

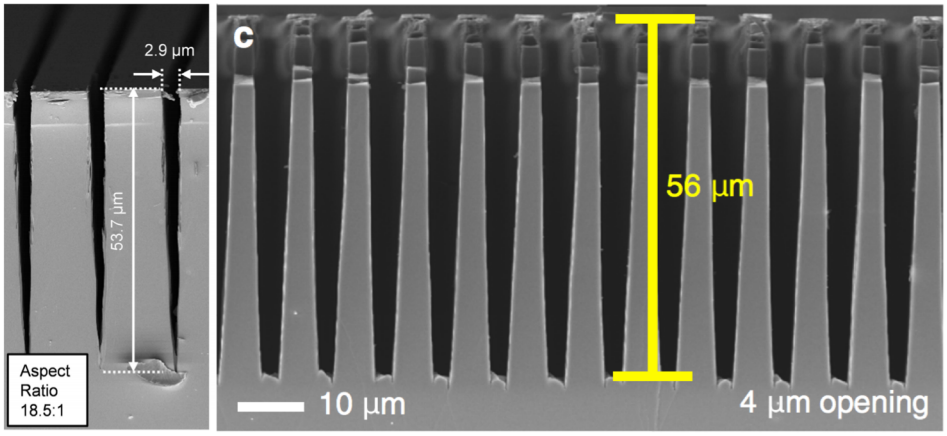

Figure 32: State of the art of SiC DRIE in 2017 with non-vertical and non-smooth profiles, far from the state-of-the-art of Si DRIE left: [71], right [72]

Q reported in a highly-stressed SiC resonator was 1M [67]. Although SiC is a promising substrate for ultra-high *Q* MEMS resonant sensors, it has so far been underperforming. In this dissertation, *Q*s beyond reach by Si are presented. The main reason SiC resonators have not shown high *Q*s, prior this work, stems from the fact that SiC DRIE is a nascent field, that needs to be improved upon.

4.1.3 Bulk micromachining of SiC, a nascent field

The chemical inertness of SiC renders its micro-machining stringent. Until 2015, the aspect ratio of SiC trenches never exceeded 10:1 [68]. In 2017, the first 20:1 aspect ratio SiC trenches have been published [69], [70]. Despite these accomplishments, the field of SiC DRIE is still not established as these trenches are not vertical nor smooth (Figure 33). Several challenges plagued the research of SiC DRIE, including the high cost of SiC, the lack of high density plasma etcher in university cleanrooms and the physics of SiC DRIE [69].

4.1.4 Pedestal-supported SiC BAW disk resonators

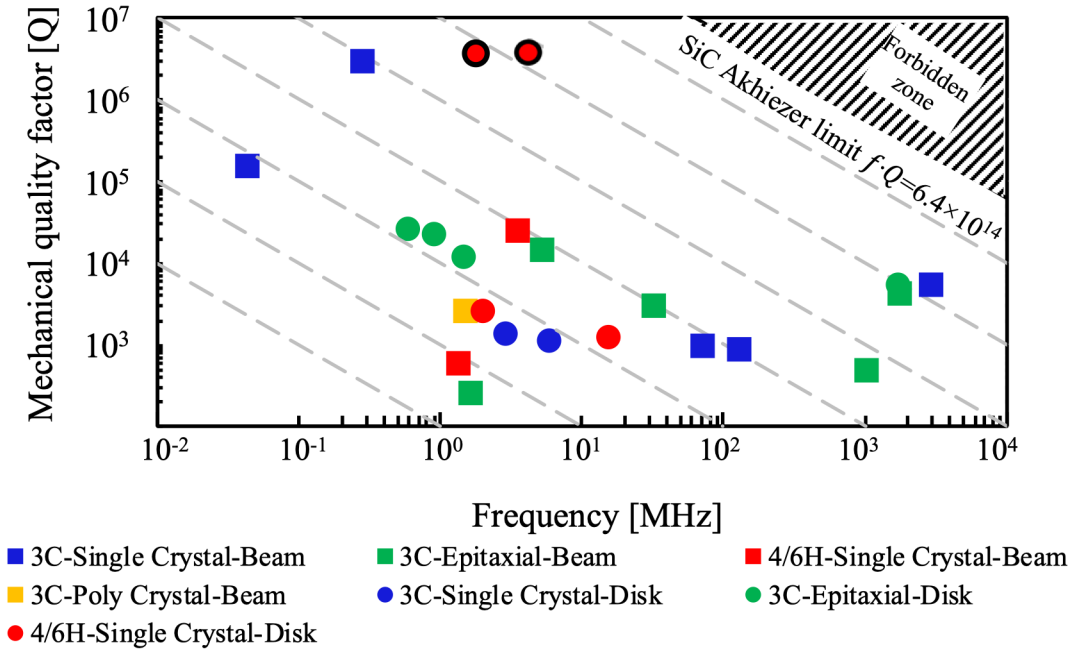

Reference	*f*	*Q*	**Material**	**Design**
Huang, X. (2003)	1.01E+09	5.00E+02	3C	Beam
Ekinci, K. (2004)	3.20E+07	3.00E+03	3C	Beam
Wiser, R. (2005)	1.47E+06	2.60E+03	poly-3C	Beam
Perisanu, S. (2007)	4.20E+04	1.59E+05	3C	Beam
Mastropaolo, E. (2009)	1.43E+06	1.20E+04	3C	Disk
Gong, S., (2012)	1.75E+09	4.25E+03	3C	Beam
Lin, C.-M. (2012)	2.92E+09	5.00E+03	3C	Beam
Mastropaolo, E. (2012)	8.90E+05	2.30E+04	3C	Disk
Svilicic, B., (2012)	1.59E+06	2.63E+02	3C	Beam
Boubekri, R. (2014)	5.20E+06	1.45E+04	3C	Beam
Kermany, A. (2014)	2.80E+05	2.90E+06	epi-3C	Beam
Wang, Z. (2014)	5.78E+06	2.30E+04	3C	Disk
Yang, R. (2014)	1.50E+07	1.28E+03	6H	Disk
Zhao, F. (2014)	1.33E+06	6.12E+02	4H	Beam
Lu, X (2015)	1.69E+09	5.59E+03	3C	Disk
Lim, A. (2016)	3.40E+06	2.50E+04	4H	Beam
Lee, J., (2017)	2.81E+00	1.40E+04	3C	Disk
Ko, S.-D. (2018)	8.43E+05	2.10E+05	4H	Disk
Yang, J. (2018)	5.00E+06	3.8E+06	4H	Disk

Figure 33: Mechanical *Q*-factors of most published SiC resonators to date

Even if SiC DRIE is established and SiCOI wafers can be manufactured, not all SiC gyroscope designs can take advantage of the extraordinarily high Akhiezer limit of SiC [49]. Section 2.2.2 established that MEMS resonators need to operate at the MHz frequency to be far in the adiabatic regime and make TED a negligible loss mechanism. At MEMS scales, only BAW modes live in this frequency range, making them ideal candidates for gyroscope applications. Among the various symmetric structures that exhibit Coriolis-coupled modes, disks maximize the surface to volume ratio, which enables to reduce surface loss drastically compared to other symmetric geometries. As observed in Si, disks need to be anchored by a pedestal that is self-aligned to the center of the disk. Any misalignment between the disk and the pedestal will generate undesirable anchor loss. Moreover, even if the pedestal is perfectly self-aligned to the disk, there will still be anchor loss due to coupling between in-plane waves in the disk and out-of-plane stress waves in the pedestal due to the anisotropy of SiC. Not only does the anisotropy of SiC generates anchor loss, it also generates frequency splitting in modes that have inappropriate crystalline symmetries. In this section, the author establishes that among the commercially available SiC wafers, n-doped on-axis 4H-SiC wafers from Cree® are ideal substrates to support the n=3 BAW elliptical modes in disk resonators anchored by a self-aligned pedestal. In this configuration, SiC gyroscopes can exhibit *Q*-factors unheard of in Si.

4.2 SiC bulk micromachining for ultra-high *Q* SiC resonant MEMS

4.2.1 Anchor loss in various SiC polytypes

Among the various SiC polytypes, single-crystal 3C-SiC has been traditionally pursued because it can be heteroepitaxially grown on SiO_2, making fabrication of thin

Table 4: Anchor loss in various SiC polytypes

3C-SiC	4H-SiC	Polycrystalline SiC
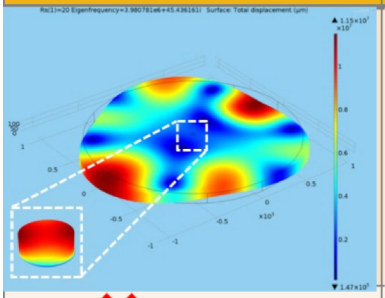	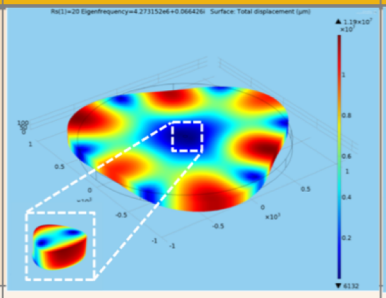	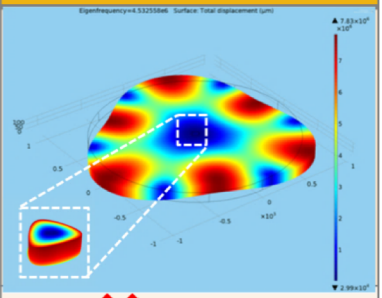
✗ Q_{ANC} = 50k	✓ Q_{ANC} = 10M-1B	✗ Q_{ANC} = 1B
• Cubic crystal symmetry • Highly anisotropic • High anchor loss	• Hexagonal crystal symmetry • Moderately anisotropic • Low anchor loss	• Entirely isotropic • No anchor loss • Difficult to manufacture, grow oxide and bond

SiCOI substrates straight forward [71]. However, 3C-SiC is a highly anisotropic substrate. 3C-SiC does not support ultra-high *Q* BAW disk resonators due to its high anisotropy. Crystal anisotropy favors the coupling of in-plane waves with out-of-plane waves that travel through the anchor and are dissipated into the semi-infinite Si substrate [59]. On the other hand, polycrystalline SiC is perfectly isotropic, which lends itself to extraordinary acoustic decoupling between the resonator and the anchoring pedestal. Anchor loss is negligible in polycrystalline substrate as long as the anchor is sufficiently narrow. However, fabricating polycrystalline SiCOI is challenging and, to this date, has never been demonstrated. The main challenges in fabricating polycrystalline SiCOIs stem from 1/ the difficulty to polish polycrystalline SiC to sub 0.5nm 2/ the large thermal stress that are generated by randomly-oriented SiC grains. Moreover, TED in polycrystalline SiC is

unknown and could be a limiting factor [57]. Finally, single-crystal 4H-SiC is commercially-available in 4" and 6" substrates. 4H-SiC offers a good compromise between low anchor loss through astute designs and SiCOI manufacturability (Table 5). In this dissertation, SiC refers to on-axis n-doped 4H-SiC. The C-face of the SiC wafer is bonded to the BOX layer and the Si-face is the face that is patterned during DRIE.

4.2.2 Custom manufacturing of SiCOI wafers

Although they have already been lackadaisically demonstrated. SiC-on-Insulator, similar to SOI substrates, are not commercially available. The lack of SiCOI wafers is a major hurdle in realizing SiC MEMS resonators. Just manufacturing a single SiCOI wafer takes a month and several thousands of dollars. This is in part due to the high cost of single-crystal SiC wafers (nearly $1,000 per 4" wafer) and the low volume of SiCOI wafer parts for academic research. As a result, the expensive SiCOI wafers are custom manufactured. The SiC wafers are bought from Cree®, are oxidized and are shipped for polishing. In this

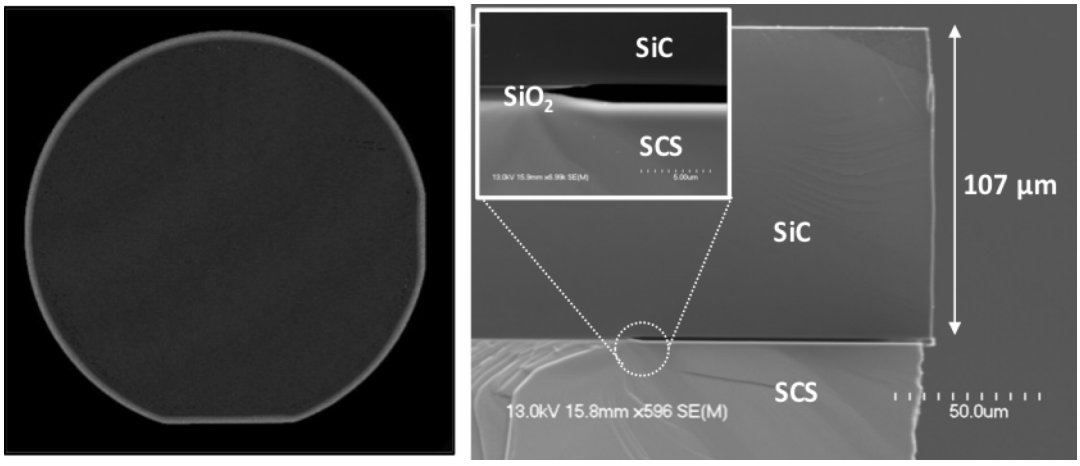

Figure 34: (Left) Scanning Acoustic Microscope (SAM) of a SiCOI wafer without any bubbles. (Right) Cross-section image of a SiCOI wafer where the BOX is revealed after exposure to HF.

work, the SiC wafers are 4H on-axis and the C-face is bonded to a Si wafer. Similarly, Si wafers are bought from Ultrasil®, are oxidized and are shipped for polishing. After polishing, a pair of Si and SiC wafers are brought in close contact. If the surface roughness of the SiO_2 layers are below 0.5nm, then the wafers bond without any significant pressure at a moderate temperature (~400°C). The SiCOI wafers are ultimately annealed at 1,100°C for 10 hours to improve the bond strength. The oxide layers that serve to bond the Si wafer to the SiC wafer can be thermally grown wet SiO_2 or TEOS with thicknesses ranging between 2 to 10μm. The SiC device layer is lapped down from 500μm to 40-100μm. This lapping and polishing step requires that there are no trapped bubbles in the BOX; otherwise, these over-pressured bubbles can burst if the SiC layer becomes too thin which can shatter the very expensive SiCOI substrates (Figure 34). Because of fabrication limitations, the edges of the SiCOI substrates are not well-bonded which appears as a grey color in Figure 34. If there was a bubble, a grey spot would appear in the body of the wafer in the SAM.

4.2.3 Ni hard mask preparation

SiC is a hard-to-etch material; masking material for SiC DRIE include Ni, Cu, ITO, AlN [72]. Photoresist and SiO_2 etch far too quickly to be used as mask material to etch deep SiC trenches. The LIGA process enables patterning Ni with smooth and vertical profiles. Additionally, the selectivity of Ni to SiC ranges from 30 to 100 to 1 which is sufficient for SiC DRIE. Therefore, Ni will be used as a mask for SiC DRIE throughout this thesis (Figure 35).

However, micro-masking constitutes a major drawback of metal hard masks in general. During processing, small Ni particles are etched off and redeposited in the SiC

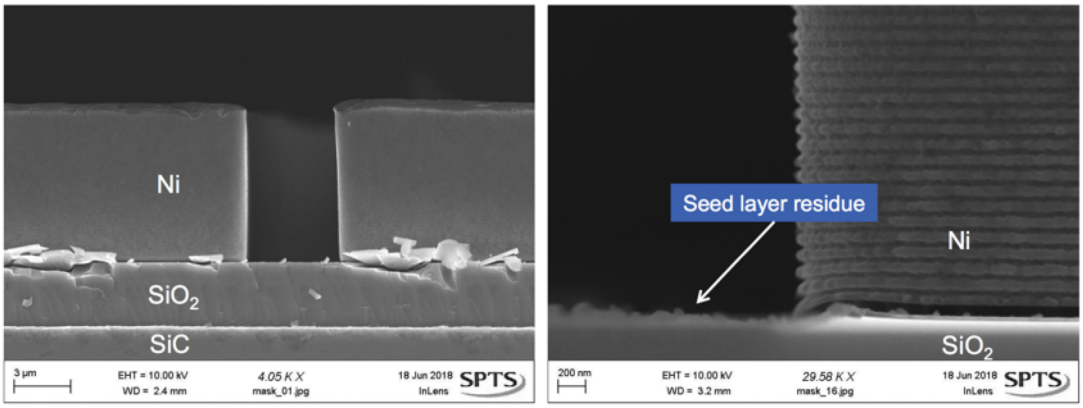

Figure 36: (Left) Vertical and smooth Ni mask patterned on SiC via the LIGA process (Right) Zoom-in view.

trench, creating a local micro-mask [73]. A Ni particle that falls into the trench generates a micro-pillar. Because of its high aspect ratio, the micropillar is significantly hotter than other surrounding features. Polymerization, which will be discussedin the next paragraph, is enhanced due to the temperature increase. This leads to the micro-pillar to be covered with a thick passivation. Upon further etching, the Ni micro-mask is removed and the SiC below as well, leaving a hollow micro-pillar which mostly consist of un-etched SiC and polymer. These features distort SiC trenches and in the worst case can merge both sides of

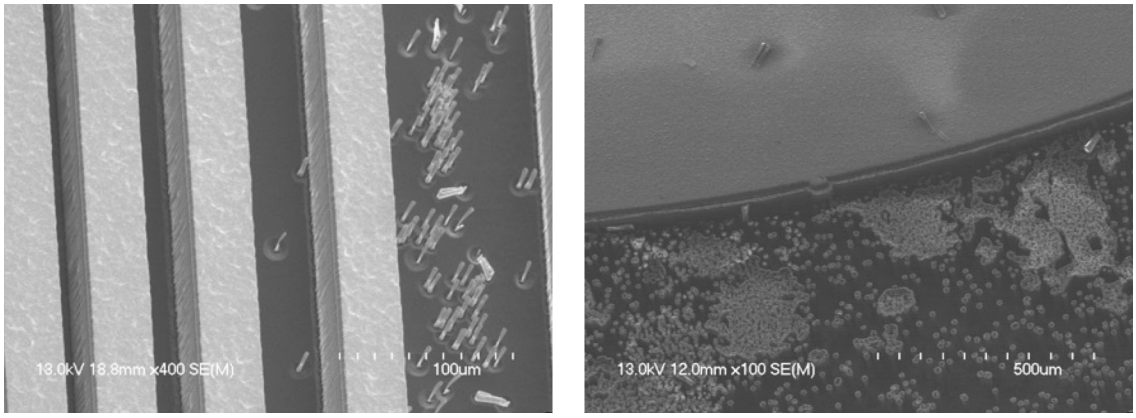

Figure 35: (left) Ni micro masking is prevalent only in trenches more than 10um wide (right) When etching mesas, the micro-pillars self-assemble and stop the etch altogether.

a trench, shorting otherwise two electrically-isolated SiC regions (Figure 36). Micro-masking is common to all metals that are used as masks for SiC DRIE (e.g. Cu and Al). Micro-masking can be greatly alleviated by argon milling the etched samples prior etching the SiC trench, which cleans the Ni streets from any undesirable residues.

4.2.4 STS AOE: a not so robust SiC etcher at Georgia Tech

In recent years, both Oxford (Oxford PlasmaPro 100 Polaris 100), ULVAC (NE550H) and STS (STS Synapse) have developed etchers designed to process reliably hard to etch materials such as SiC, GaN, InP at wafer level. However, these tools are not deployed in universities in the USA that are made available to the author. As a result, an outdated, refurbished, 20-year old STS AOE is used instead (Figure 37). While this tool is made readily available by a dedicated IEN staff, it is not designed to etch SiC, bringing to the author a lot of misery between 2015 and 2018 (fun fact: the misery is still ongoing for the next generation of AOE users). The main challenge is the passivation that forms the micro-pillars also accumulates on the sidewall of the chamber and on the ceramic

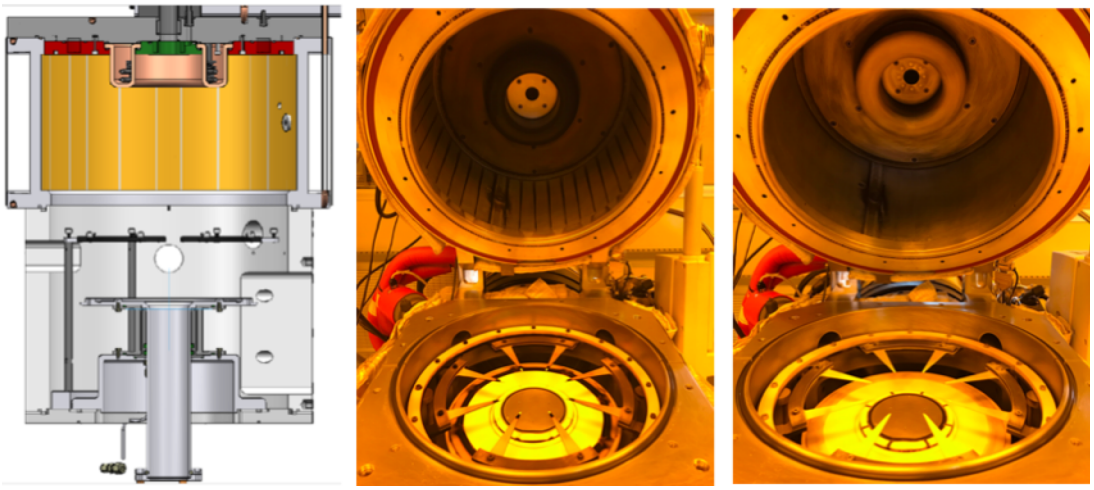

Figure 37: STS AOE (left) schematic (center) after SiC etching (right) after manual cleaning.

hardware. The STS AOE must be cleaned manually every 30 RF hours in average at room temperature while by design the chamber's wall's temperature is set at 120C. This ongoing temperature cycling generates significant stress on a refurbished tool. Further, the SiC etch recipe is so powerful that it consumes the ceramic hardware and the lip seal. Etch repeatability is challenged by this constant hardware degradation. More recent tools have higher etch rates, longer mean time between cleans but cost near $1M.

4.2.5 SiC etching recipe using STS AOE

It is important to note that STS AOE at GT is unconventional. The chuck has been downsized from 6" to 4" and some of the fused quartz hardware has been replaced by ceramic hardware. Further, the chiller is old and perhaps 10 feet away from the chamber, generating an unknown thermal resistance between the chiller and the chuck. Although the chiller temperature is set to 0°C during etching, the temperature of the chuck is probably near 5 or 10°C. For example, if the tool is moved from Petit to Marcus cleanroom, this thermal resistance can change, and with it the recipe altogether. Temperature is key.

Another issue is the o-ring that surrounds the chuck gets constantly degraded by the high-power plasma. Its constant degradation lets He flow inside the chamber at a variable rate, somewhat masking the true gas composition during any etch run. Making SiC DRIE repeatable as it is for Si in a Bosch process is challenged by the constant degradation of the hardware and the passivation that quickly builds up on the chamber's sidewall (table 6).

Table 5: SiC etching recipe in STS AOE at GT

Parameter	Value	Comment
O_2 gas flow	7sccm	Low value to generate F* radicals
SF_6 gas flow	30sccm	Flow rate depends on the exposed area %
Ar gas flow	70sccm	
Coil power	500W	High power to break SiC bond but too high power induces secondary trenching
Platen power	200W	
DC bias voltage	270-300V	
He backside cooling	9500mTorr	o-ring degrades constantly, always shifting these values
He backside cooling	23sccm	
He LUR	Near 40mTorr/min	
Chiller temperature	0°C	See prior comments
Pressure	8mTorr	Lower pressure is preferred but limited by gas flow rate

4.2.6 Passivation in SiC DRIE

The SiC etching recipe uses Ar to make single-crystal SiC locally amorphous, SF_6 to chemically react with Si, O_2 to enhance the formation of F* and to react with C. Unlike the Bosch process and its close parents, SiC is etched continuously without cycling between passivation, passivation removal and etching. To the author's best knowledge, the passivation cannot be removed by plasma etching. The passivation is a mixture of Ni, S, F, C. This passivation gradually builds up at the top of the trench and ultimately pinches the gap; this is the mechanism that predominantly determines the ultimate aspect-ratio of the SiC trench (Figure 39). After etching, the passivation can be easily removed in diluted HNO_3; since the Ni mask is also removed, this cleaning step cannot be used to selectively remove the passivation to carry on the etch (Figure 38). A major step in SiC DRIE would consist in finding a way to quickly and selectively remove the passivation layer, either using dry etching (unknown to this day) or wet etching (room temperature EKC 265 removes the passivation with poor selectivity to Ni).

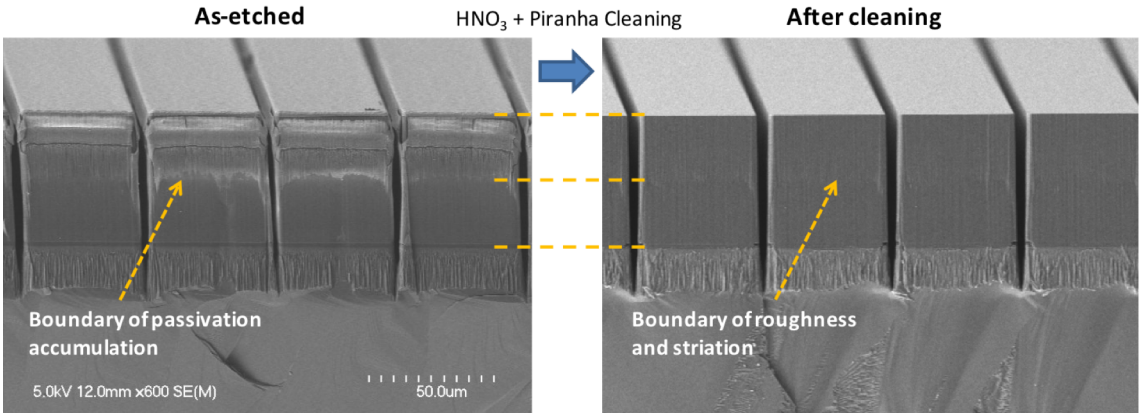

Figure 38: Wet cleaning of passivation and Ni mask reveals vertical and smooth trenches in SiC on Insulator

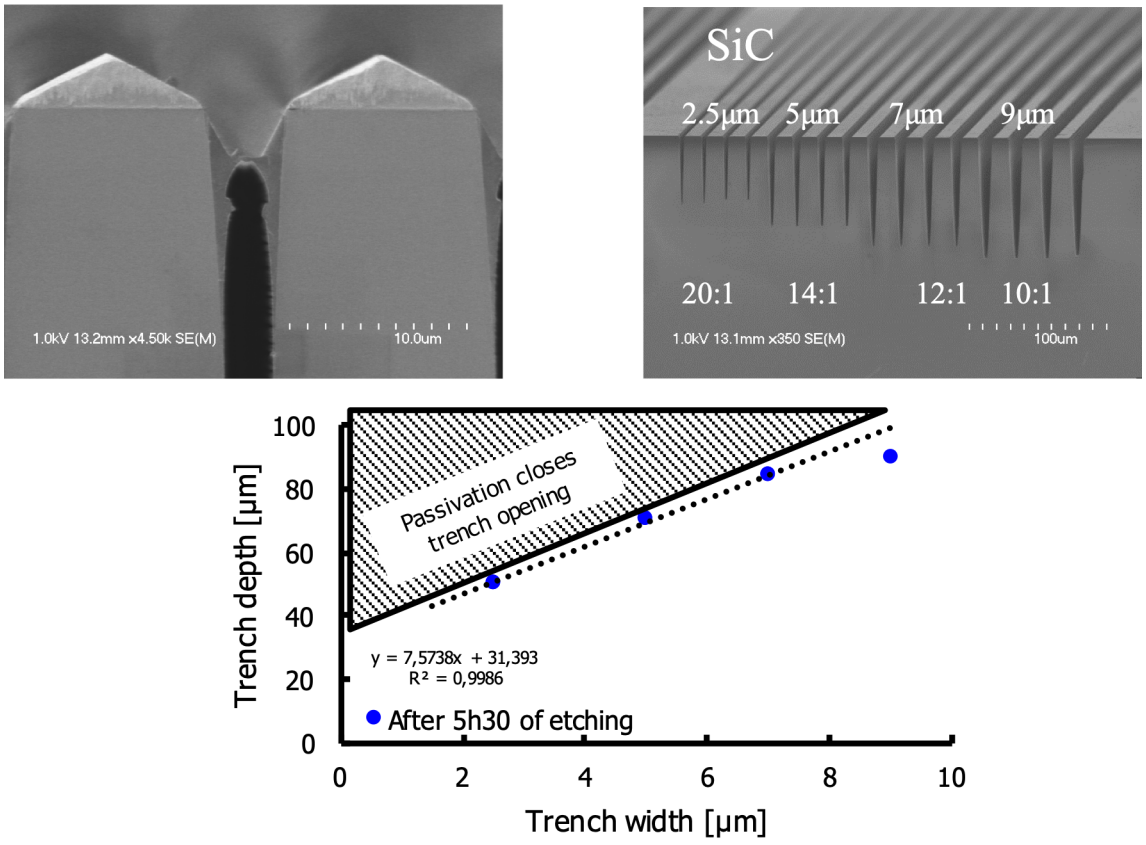

Figure 39: $NiC_xF_yS_z$ passivation accumulates, throughout etching, at the top of the trench; ultimately, the passivation closes the trench which limits the maximum achievable aspect-ratio.

4.2.7 SiC DRIE optimization parameters

Since SiC DRIE is a nascent field and given the cost of SiC, most of the SiC DRIE process trends have been measured on 2 by 2 cm wide SiC dies (Table 7). Under these conditions, edge effects are dominant. These process trends might vary when the dies are scaled up to wafer level, in particular uniformity and trench quality.

Table 6: SiC DRIE process trends

Process parameter	Etch rate	Selectivity to Ni	Uniformity	Sidewall quality
Bias power	↑↑	↓↓	↑	↑
Comment	Too little power does not break SiC bonds; too much power induces secondary trenching			
Ar addition	↑	↓↓	↔	↑
Comment	In literature, Ar addition decreases sidewall quality; in our work, we found an opposite trend.			
Pressure	↑↑	↑	↓	↑
Comment	Pressure is currently fixed throughout etching; in future work, recipes with varying pressure to accommodate for the trenches' aspect-ratio will be investigated			
Chiller temp.	↑↑	↓	↔	↑
Comment	At lower temperature, the passivation is denser and closes the gap less quickly which improves the maximum achievable aspect-ratio			
Total exposed area	↓	↓	↔	↓↓
Comment	When increasing the total etch area, gas flow must increase and chiller temperature must decrease accordingly			

4.2.8 SiC DRIE with variable gap size

Trench quality during SiC DRIE depends on the width of the cross-section. For a given recipe, if the trench is too wide then, secondary trenching can occur (Figure 40). Also, even if the trenches etch well, their intersection – which has a larger effective cross-sectional area – might not etch well due to excessive accumulation of passivation which, in turn, generates roughness. While these issues can be circumvented with clever designs, proper recipe optimization for any mask and total exposed area is necessary.

4.2.9 SiC DRIE with nanoscale roughness

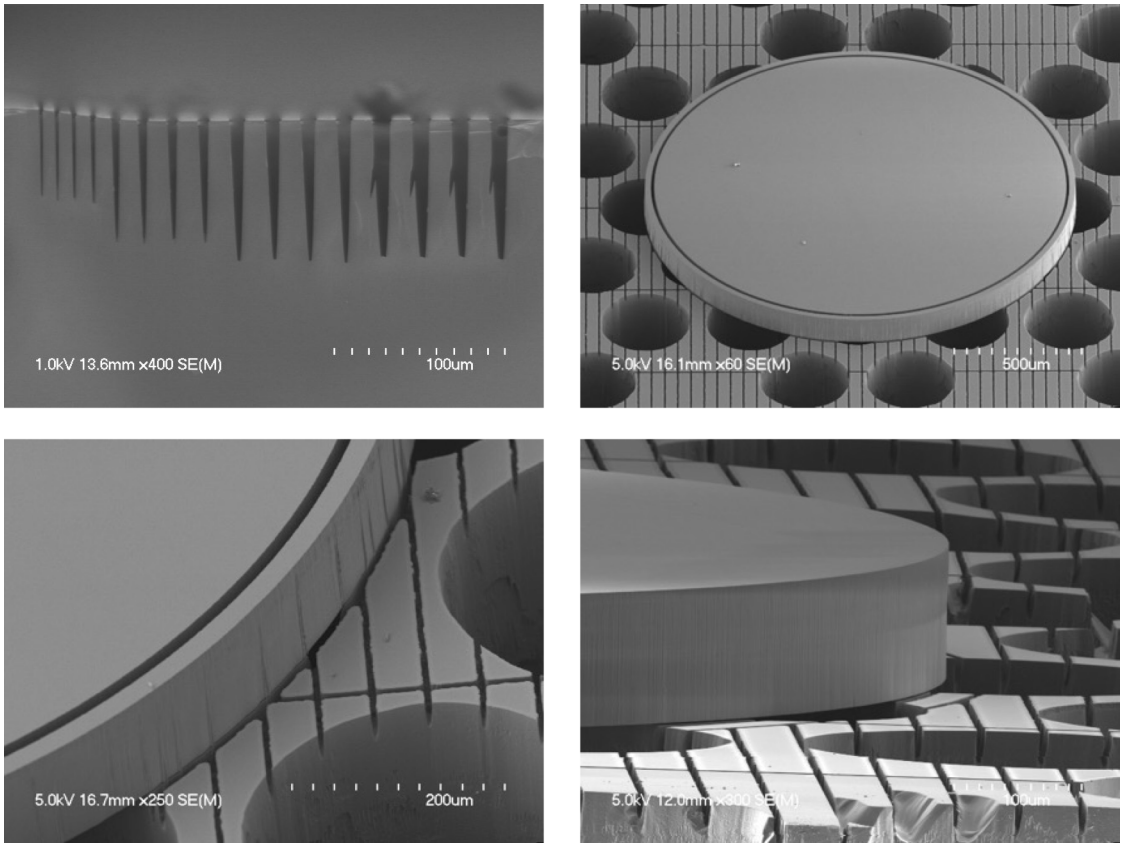

Figure 40: Trench quality depends strongly on the width of the trench. Secondary trenching can occur in relatively large trenches. Similarly, roughness is increased at the intersection of two trenches because the local cross-section is larger; this effect can be alleviated by designing a single trench around the disk.

Under optimized conditions, STS AOE can etch 6μm vertical trenches in 60μm thick SiCOI in under 6 hours (Figure 41). Because there is no cycling between etching and removing passivation, SiC trenches are free from scallops. The main source of roughness in SiC trenches come from imperfections in the Ni mask due to photolithography and the finite wavelength of the light source.

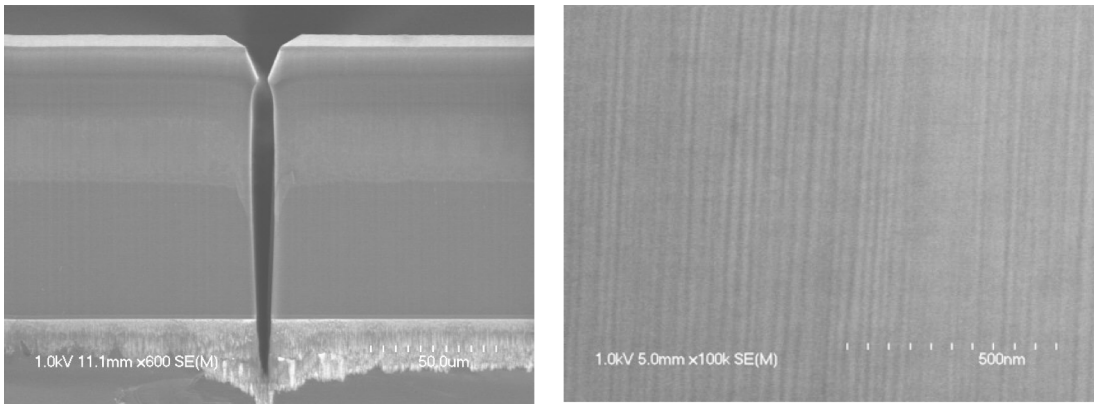

Figure 41: Vertical SiC trenches with near 50nm roughness

4.3 Ultra-high *Q* SiC solid disk resonators with BAW gyroscopic modes

The previous section shows that SiC exhibits a fantastic *fQ* product, far beyond the reach of Si (see 2.2.1) and that bulk micromachining of SiC is feasible using commonly-available etchers (see 4.2). This section shows that interestingly SiC is an excellent substrate for gyroscopic application and particularly for z-axis gyroscopes. As shown in section 1.3, high performance gyroscopes need to have high *Q*s and be mode matched. The mode matching conditions require that both Coriolis-coupled modes have nearly identical frequencies and quality factors.

4.3.1 4H-SiC: an appropriate substrate for mode-matched resonant MEMS gyroscopes

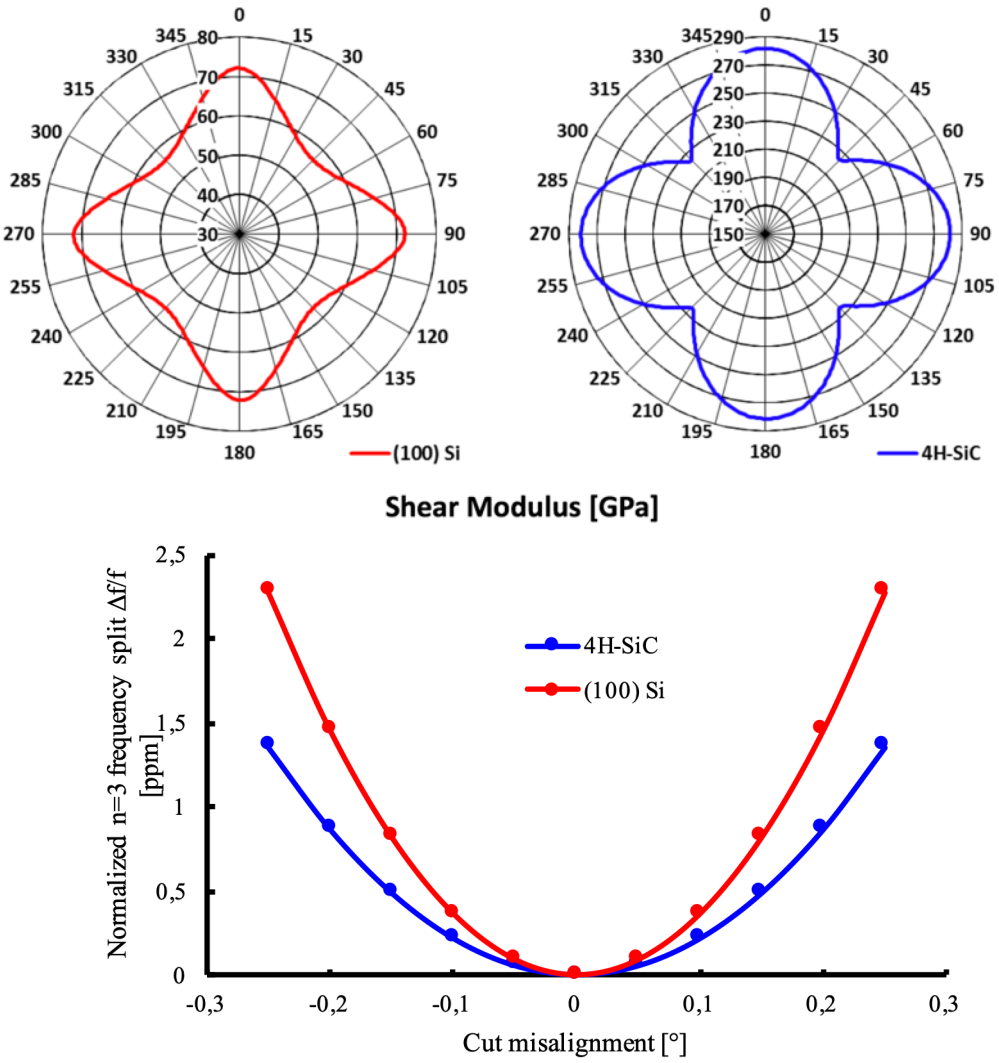

Figure 42: (top) Shear modulus of (right) 100 Si and (left) 4H-SiC (bottom) frequency splitting of=3 modes in Si and 4H-SiC

Section 2.2.1 established that SiC resonators can reach extremely high *Q*-factors; however, high *Q*s is only one of several requirements for gyroscope applications. The second requirement that sticks out from the equations (see 1.3) is modal degeneracy. Alike (100) Si, 4H-SiC supports modal degeneracy for odd higher order elliptical modes (n=3, 5 etc.). This is a direct consequence from the symmetry of the shear modulus of SiC (Figure

42). Experimental results provided further in this section shows that odd-order elliptical modes can have frequency splits as small as a few ppm while even-order elliptical modes have frequency splits that in the several thousands of ppm range. Thus, a SiC disk resonating in the n=3 elliptical modes is an appropriate resonator design for gyroscope applications. Throughout this section, except if mentioned otherwise, the modes of interest in SiC disk resonators are the degenerate n=3 modes. In the quest of demonstrating higher *Q*s, other modes including the breathing n=0 mode are also investigated.

4.3.2 A path towards capacitively transduced high Q SiC disk resonators

Fabrication of capacitively transduced high *Q* SiC disk resonators has been divided into several steps. The first generation of SiC resonators are transduced using a piezoelectric stage and measured using an LDV (Figure 43). These devices are not surrounded by high aspect ratio trenches, which simplifies fabrication greatly. The second generation of disk resonators are driven capacitively and sensed using an LDV. Optical

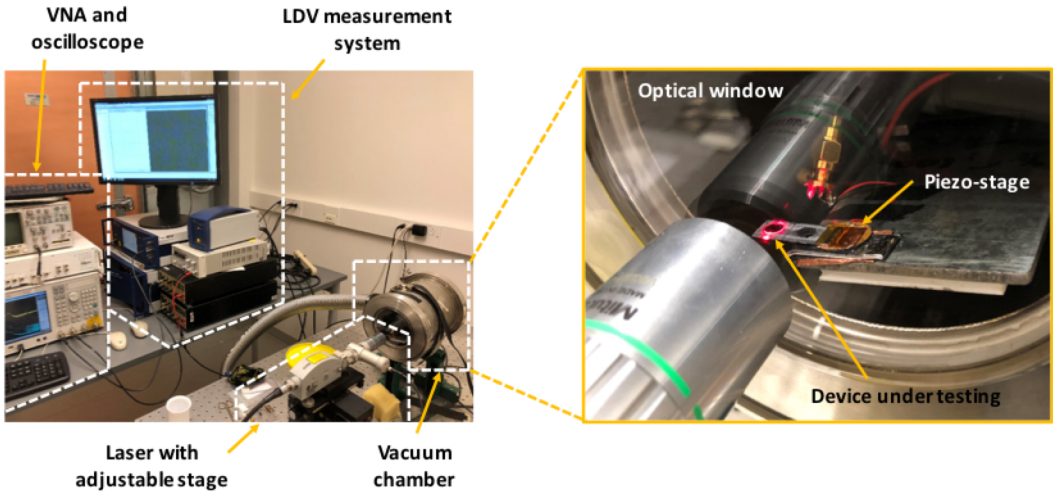

Figure 43: LDV set-up; the SiC disk resonators are actuated using a piezo-electric stage and the displacements are measured using the LDV

sensing being extremely sensitive requires the displacement of the disk to be on the order of several femtometers. Therefore, the transduction gap is large in the second generation of SiC resonators, on the order of 9 to 11µm. The third generation of SiC disk resonators have gaps between 3 to 6µm. These devices are driven and sensed entirely capacitively. In future work, the fourth generation of SiC disk resonators will benefit from the HARPSS process which will convert the gap's width from between 4 to 6µm to between 300 to 600nm.

4.3.3 Generation 1: SiC disk resonators without any electrodes

Generation 1 of SiC disk resonators came in two flavors. The very first devices were 9 mm wide and had release holes to facilitate releasing [15]. As expected by FEM, TED is the dominant loss mechanism; these devices have *Q*s in the 120k range and large frequency splits (250Hz at 840kHz or 2,900ppm). These large frequency splits arise from the release hole distribution that did not match the symmetry of the shear modulus of SiC (Figure 44). The next generation 1 devices had no release holes. With similar dimensions as the devices with release holes, releasing 9mm-wide solid SiC disks took over 8 hours

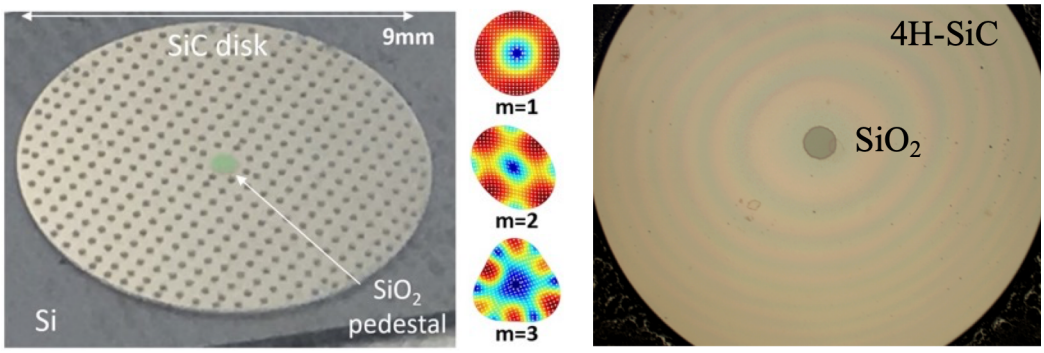

Figure 44: SiC disk mounted on a SiO_2 pedestal with (left) release holes and (right) without release holes [15]

compared to under 30 minutes. The main difficulty in releasing disks without release holes relies in making sure the releasing stayed self-aligned which is key for both high *Q* and small frequency splits. The highest *Q*s measured in the first generation of SiC disk resonators (Q=3,8M) is beyond any values published in the field of SiC MEMS resonators [67], which is focused on 3C SiC (Figure 45). A phononic crystal is embedded in the Si to further isolate the SiC disk from the Si substrate (Figure 46). There is a lot of engineering

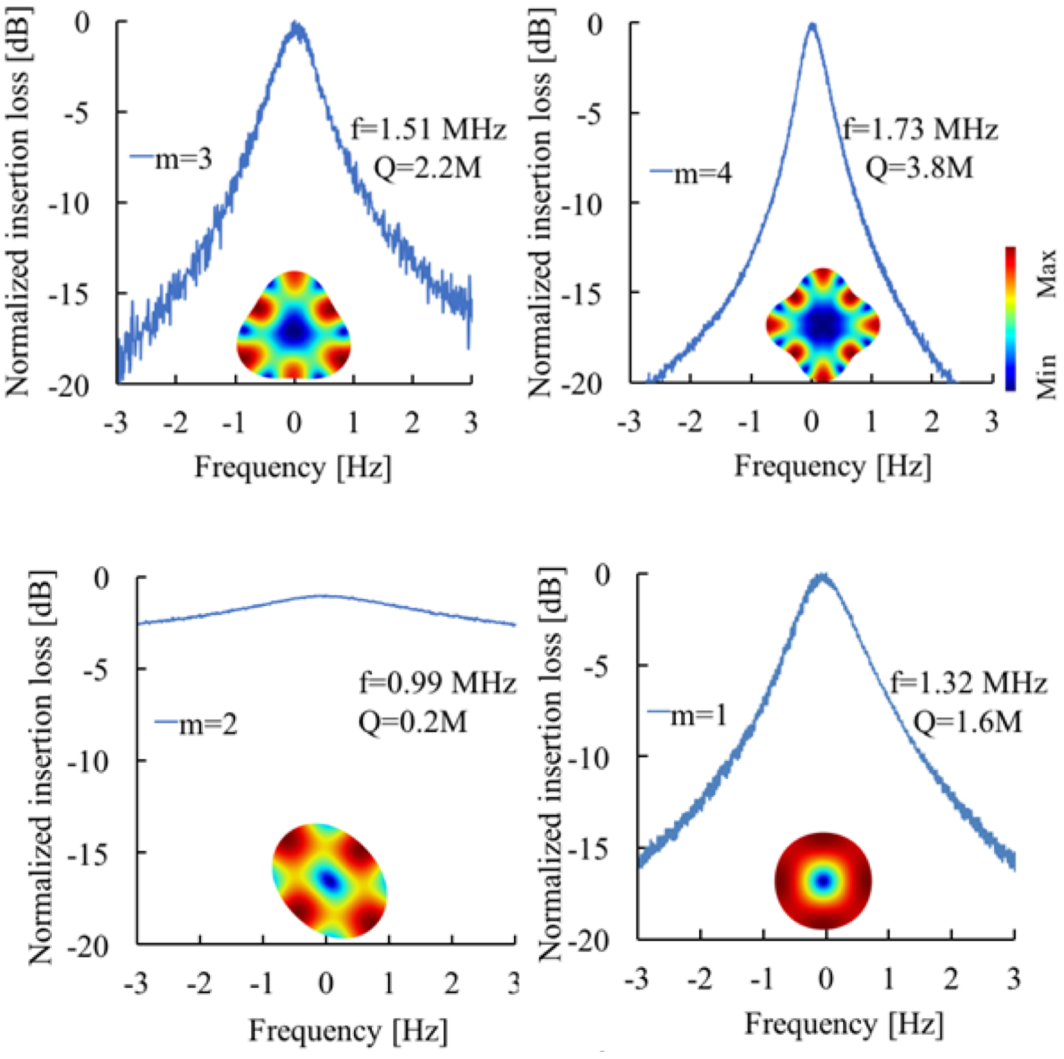

Figure 45: High *Q*s in solid SiC disks anchored on Si via a SiO_2 pedestal

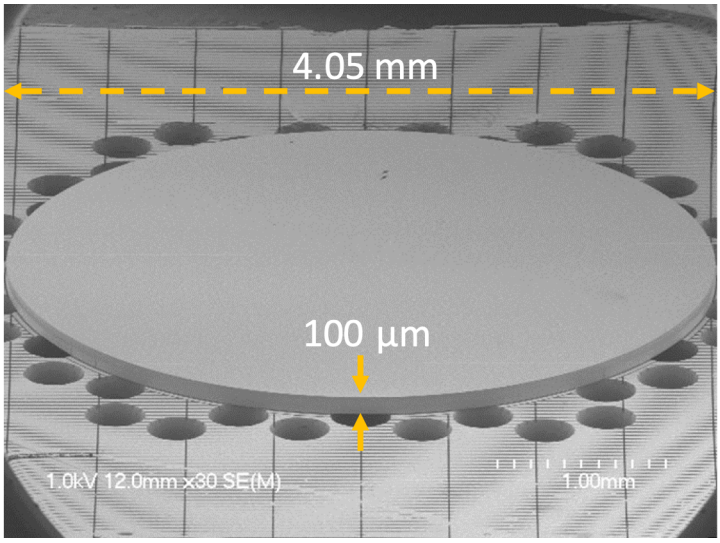

Figure 47: (left) Ultra-high *Q* SiC disk resonator on a Si phononic crystal

that goes into designing phononic crystals. For the sake of brevity, the modeling of phononic crystals is not included in this thesis. Alike for the disks with release holes, the location of the Si vias constituting the phononic crystal can also contribute to the frequency split. Careful designing ensures that these Si vias respect the structural symmetry of SiC. Frequency splits as small as 3ppm have been measured in generation 1 SiC disk resonators (Figure 47). The quality factors of generation 1 devices are limited by surface TED which

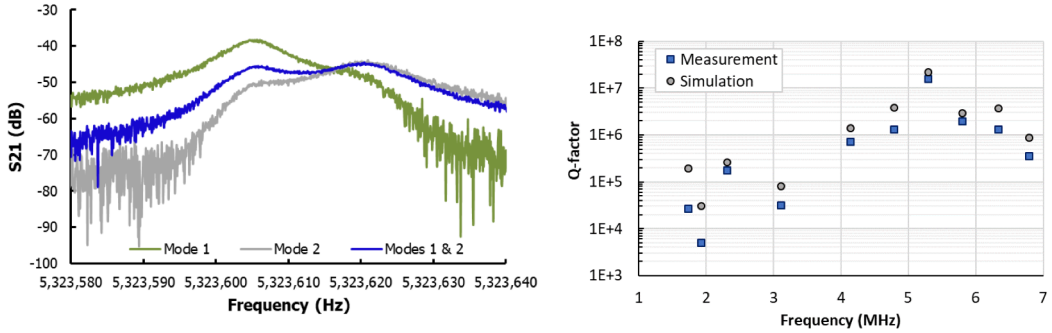

Figure 46: Generation 1 SiC disk resonators on PnC have (left) frequency splits that could be electrostatically tuned with electrodes nearby (right) the *Q* measurements match simulations

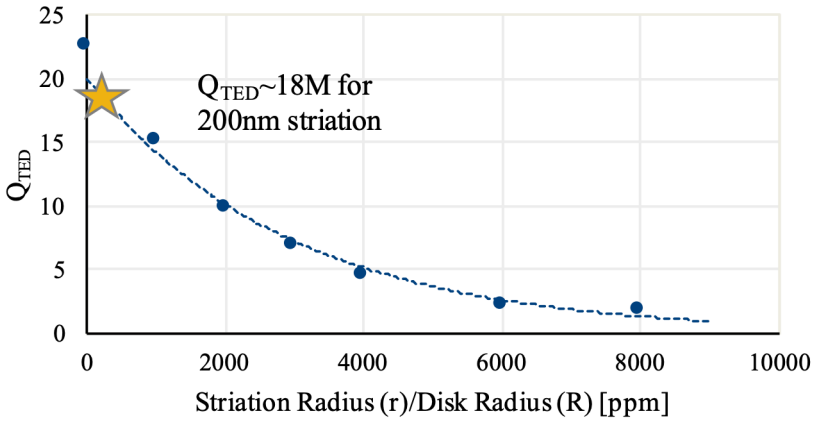

Figure 48: Surface roughness generates surface TED which is the dominating loss mechanisms on generation 1 SiC disks on PnC

is generated by surface roughness (Figure 48). The vertical roughness on the SiC originates from imperfections from the Ni massk; these imperfections in turn come from the finite wavelength used during photolithography (355nm). Improving photolithography or using other patterning methods are necessary to further decrease the surface roughness of SiC trenches. However, per FEM simulations, even with such surface roughness, *Q*s beyond 100M are still in reach. Interestingly, simillar roughness on shell resonators limit *Q* to around 100k; this shows just how robust to fabricaton imperfections BAW modes in disks are compared to flexural modes in shells.

4.3.4 Generation 2: SiC disk resonators with distant electrodes (d>9μm)

The second generation of SiC disk resonators are surrounded by self-aligned SiC electrodes (Figure 49). These electrodes are far away from the SiC disk with an approximate gap width between 9 and 12μm. The main reason is that the SiC thickness of the SiCOI wafer is 100μm which is too great to etch instead 4-6μm wide trenches. The

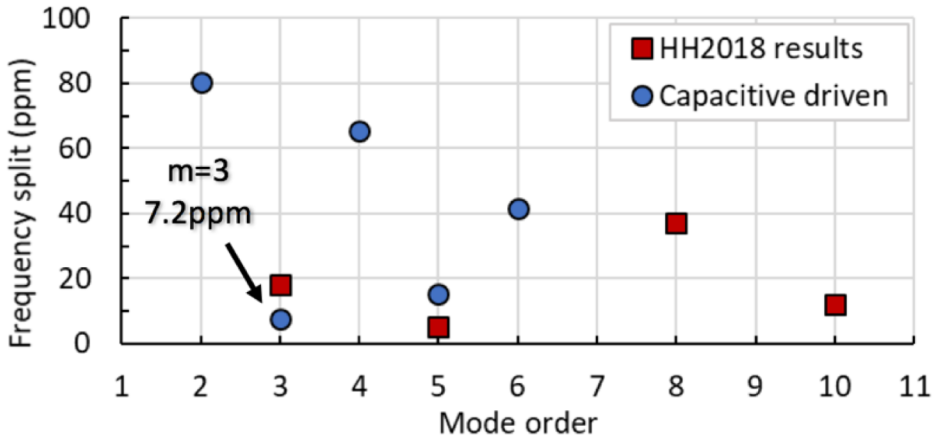

Figure 49: As-fabricated frequency split measurement

introduction of electrodes enables to drive the disk electrostatically and to sense optically. The gaps are too wide and the motional resistance too large to sense the modes capacitively, except for the m=4 mode which has a *Q* of 1.1M. As expected, *Q* measurements using either capacitive or optical readouts produce similar values. Moreover, frequency splits in generation 2 disk resonators are in good agreement with generation 1 disk resonators (Figure 50).

4.3.5 Generation 3: SiC disk resonators with nearby electrodes (d<6µm)

The third generation of SiC disk resonators are driven and sensed capacitively with 6µm wide gaps (Figure 51); the SiC thickness is about 55-60µm. Under these conditions, the motional resistance is between 1 to 10MOhms. The phononic crystal that isolate the SiC disk from the Si substrate is defined in the Si layer; the SiC layer remains un-etched around the electrodes as can be observed in Figure 51.

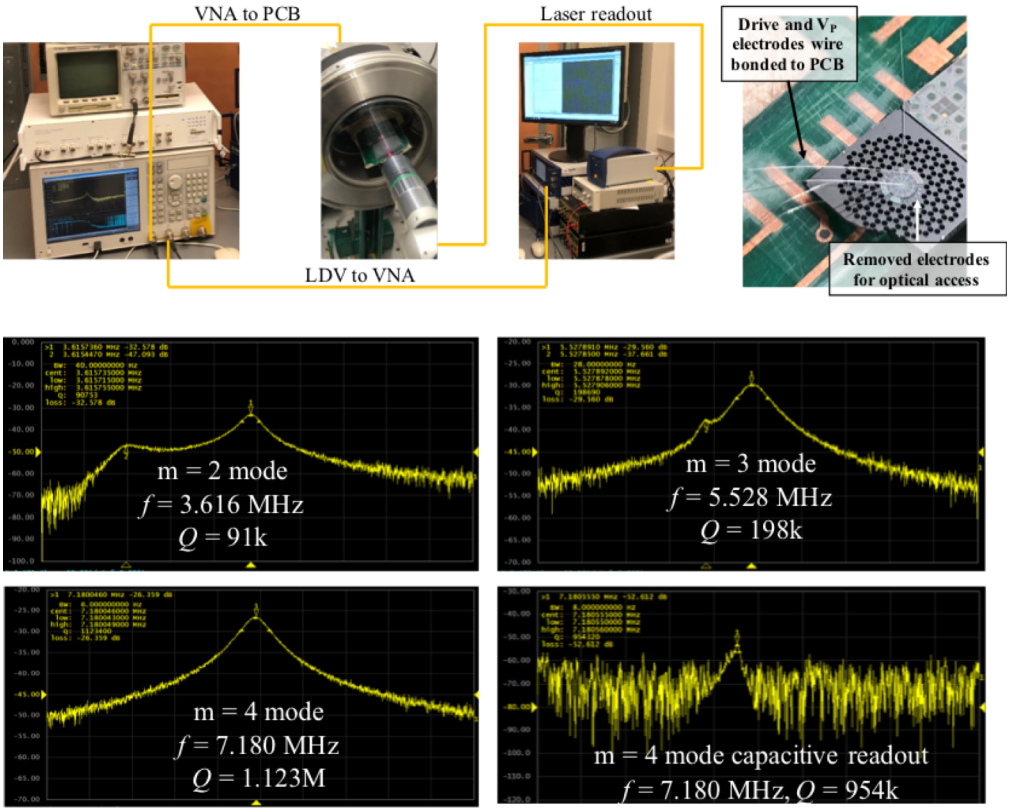

Figure 50: (top) Capacitive actuation optical readout measurement setup (bottom) Frequency response of several in-plane BAW modes in generation 2 disk resonators

Currently, the SiC trenches are etched in one single run and, as explained in 4.2.6, the deposition of the passivation at the top of the trench limits the aspect-ratio. Until a way to remove the passivation or a way to drastically limit its deposition rate is found, the trenches cannot be less than 6µm wide assuming a 60µm depth. Even under these conditions, the passivation closes the gap, which leads to undesirable trench pinching towards the bottom (Figure 52).

In generation 3 SiC disk resonators, polycrystalline silicon is deposited on the SiC electrodes and towards the center of the SiC disk resonators. Poly-silicon on bare SiC forms an ohmic contact when annealed at 1,200°C after 3-4min. It is not possible to directly

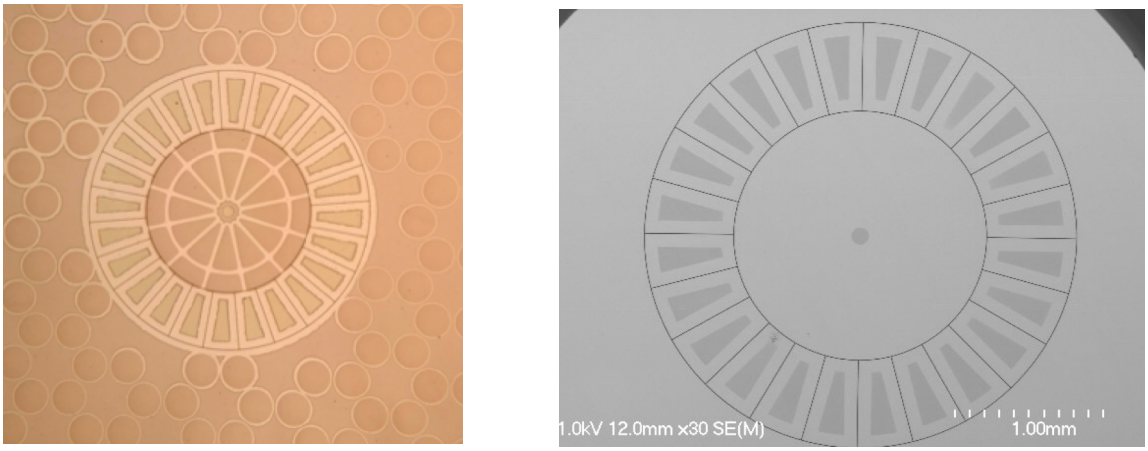

Figure 51: (left) optical and (right) SEM pictures of gen. 3 SiC disk resonators with nearby electrodes.

wirebond to SiC, the contact would be in the mega-ohm range while after annealing poly-Si on SiC, the ohmic contact is in the 700Ohm range. Assuming proper fabrication and well-sought designs, thermal stress due to CTE mismatch between SiC, polySi, SiO_2 and Si does not deflect the SiC disk resonator (Figure 53).

Because the trenches are not etched uniformly in the last 2-3µm (Figure 52), the generation 3 SiC disk resonators are particularly sensitive to feedthrough. To date, the author could measure one pair of n=3 modes in a generation 3 SiC disk resonator with nearby electrodes. The *Q* value isn't close to the one measured in generations 1 and 2. It is possible that there are some debris that remain in the SiC trench that dampen the disk (Figure 54).

To assess the fabrication challenges faced by generation 3 SiC disk resonators, Lamé mode resonators with narrower gaps (d=3µm) have been built (Figure 55). The passivation had to be removed during etching, otherwise the trenches would have never

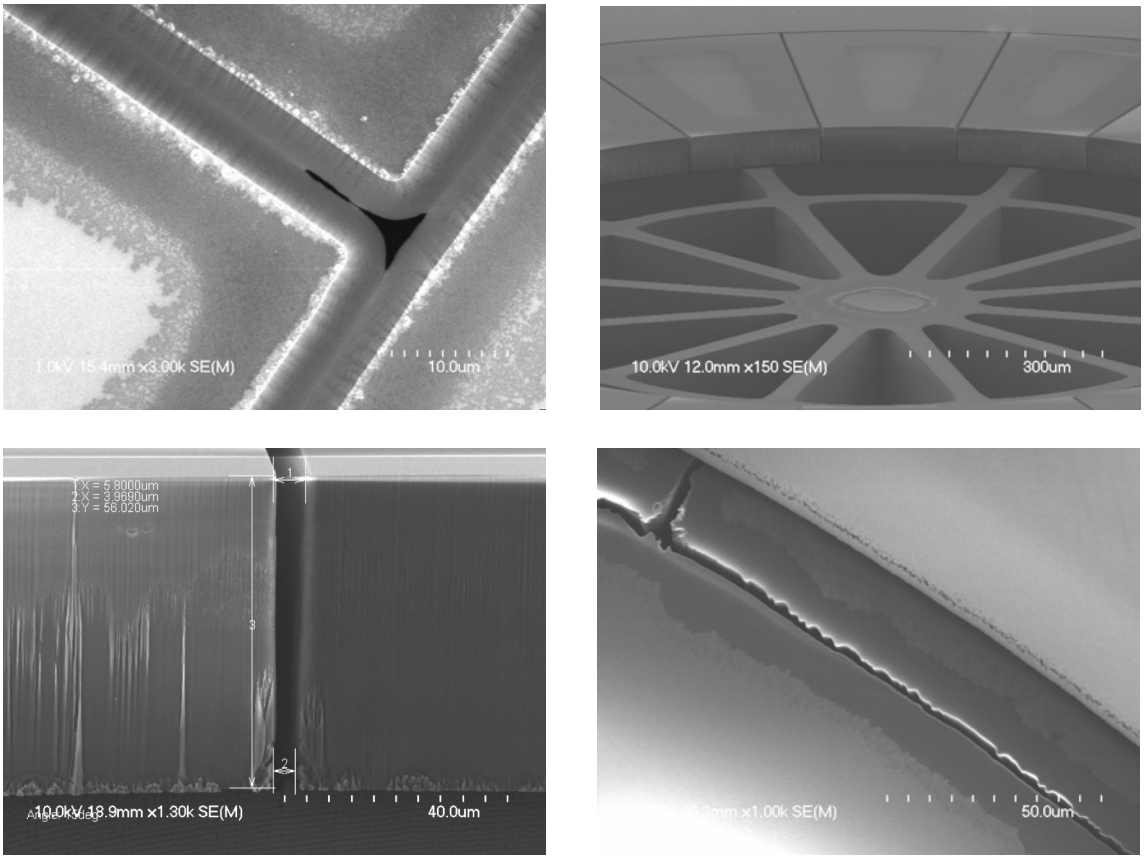

Figure 52: (top left) Trench closing due to passivation build up. (top right) SiC electrodes surrounding a removed SiC disk (bottom left) SiC trench with un-etched bottom 3µm (bottom right) Bottom view of SiC trench showing non-uniform gap, favoring feedthrough

been etched through. EKC 265 at room temperature partially etches the passivation layer as well as the Ni mask. As a result, the top of the SiC trenches are damaged because the Ni mask recessed. Interestingly, the fabrication yield of SiC Lamé mode is relatively low a many tethers cracked during release. This seems to suggest there are some internal stress gradients in the SiC wafer due to SiCOI fabrication (bonding, grinding and polishing) or due to the Ni mask patterning. Further studies are required to determine the e xact cause of the low Lamé resonator fabrication yield. Despite these challenges a Lamé mode with

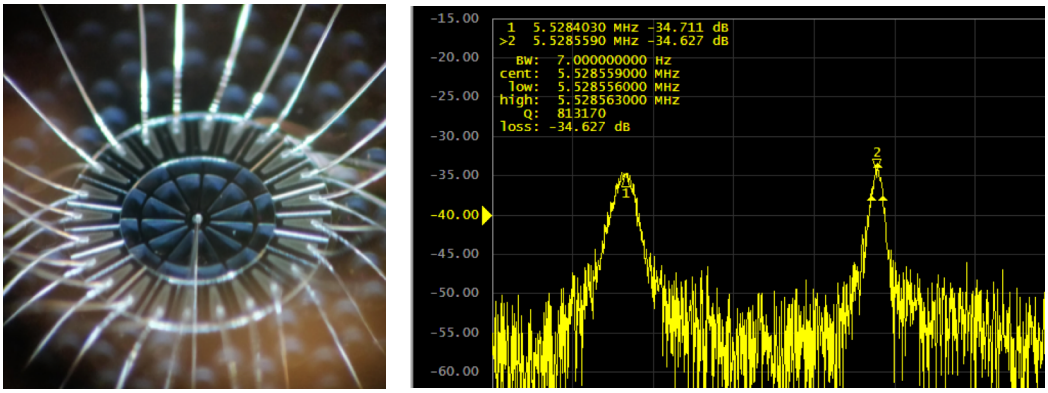

Figure 54: (left) Electrostatically measured SiC disk resonator (right) frequency response.

a quality factor near 300k with no feedthrough has been measured from -50°C to room temperature. The thermal coefficient of frequency (TCF) of a Lamé mode oriented along the major flat on a n-doped 4H-SiC wafer is -11ppm (Figure 56).

4.4 Conclusion and future work

Bulk micromachining of ultra-low dissipation resonators has been shown in this chapter. Building on this work, SiC DRIE at wafer level must now be developed to the

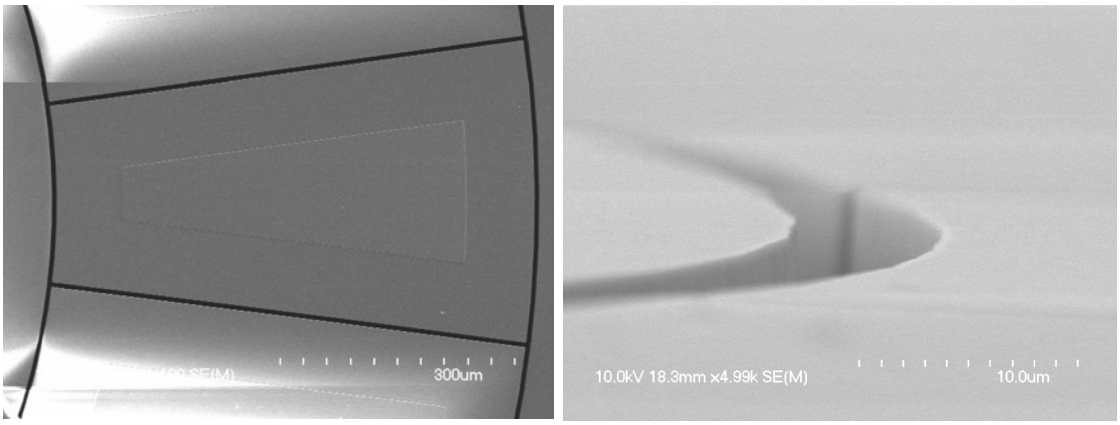

Figure 53: (left) Poly-silicon on SiC to form an ohmic contact after annealing at 1,200°C for 4 minutes (right) the SiC disk does not deflect even after annealing

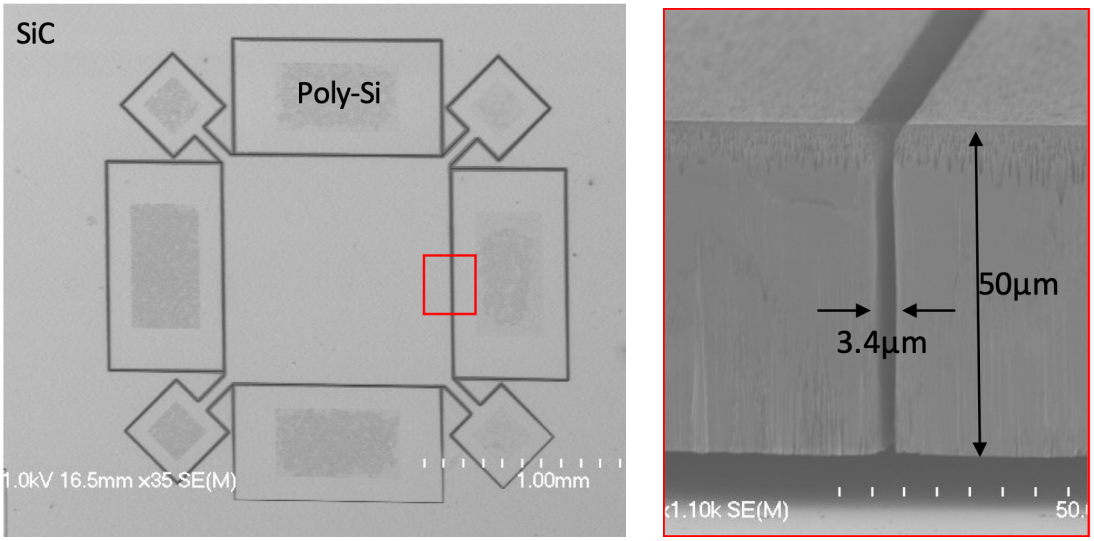

Figure 55: (left) SEM of capacitive Lamé mode resonator (right) cross-section of the SiC trench

same maturity level as Si DRIE. The growth of the passivation layer and micromasking from the Ni mask introduce significant challenges. New etchers for hard-to-etch materials are now commercially-available but are too expensive to date to be purchased in university cleanrooms. Until these etchers become commonly available, cleaning the trenches during etching to remove the passivation and careful monitoring of Ni particles to avoid excessive micro-masking will be instrumental in streamlining SiC DRIE.

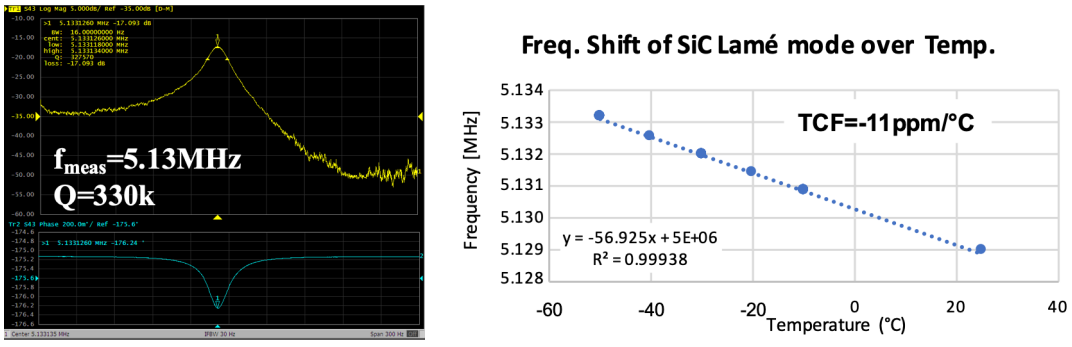

Figure 56: (left) Frequency response of a SiC Lamé mode at room temperature and (right) across the temperature range -50 to 25°C. The extracted TCF is -11.2ppm/°C.

CHAPTER 5. STIFFNESS TRIMMING OF HIGH *Q* RESONATORS AND RESONANT GYROSCOPES

5.1 Background

System level tuning methods use the residual quadrature error to maintain perfect mode-matching conditions at the cost of large, complex and contiguous CMOS-implemented architectures that consume power continuously. To reduce power consumption during the numerous hours of operation, system level methods must be complemented by other less power-hungry approaches. For example, mode-matched gyroscopes must be designed such that the different modes have identical frequency of resonance to avoid trimming large amounts of as-born frequency splits. In particular, some designs are more robust to fabrication errors than other designs and yet still show frequency splits as large as 1%. To achieve the ambitious objective of mode-matched conditions with 1ppm of frequency split, many device-level methods have been prospected and are reported in the next section.

5.2 Fundamentals of frequency control

5.2.1 Literature review

Because the literature is too important, only a few approaches will be discussed to describe most frequency control techniques (Table 8).

Table 7: Frequency control literature review

Publication	Method	Range	Resolution	Highest Q	Mode-matching compatible	Drawbacks
Sharma, 2009	Residual quadrature error	8-15Hz	Near 0Hz	36,000	yes	Bandwidth limitation
Sonmezoglu, 2012	Residual quadrature error	1kHz	Near 0Hz	Not reported	yes	Time consuming for high Qs
Fan, 2005	Robust design	1.66%	Not reported	Not reported	no	Precision
Ha, 2006	Robust design	1%	Not reported	Not reported	no	Precision
Lee, 2008	Electrostatic forces	55%	Not reported	Not reported	yes	V_P =150V
Lee, 199	Electrostatic forces	3.3%	Not reported	Not reported	yes	V_P =20V
Adams, 1998	Electrostatic forces	-7.7% + 146%	Not reported	Not reported	yes	nonlinearity
Cabuz, 1994	Electrostatic forces	±8Hz	Not reported	Not reported	yes	Fatigue in torsion bar
Chen, 2012	Electrostatic forces	0.5%	83.3ppm/V	2,000	yes	Composite structures
Eun, 2014	Electrostatic forces	3.2%	Not reported	112 (air)	yes	V_P =30V
Piazza, 2003	Electrostatic forces	0.8%	Not reported	6,200	yes	V_P =20V

Le, 2013	Electrostatic forces	89%	Not reported	Not reported	yes	nonlinearities
Hsu, 2007	Laser ablation	5%	2.6ppm	Not reported	yes	Re-deposition
Abdelmoneum 2004	Laser ablation	2%	21ppm	14,000	yes	Resolution, quality factor
Chiao 2004	Laser deposition	1.2%	0.5%	Not reported	yes	*Q* degradation, resolution
Courcimault 2005	Mass deposition	11%	90Hz/nm	25,000	no	Precision, annealing
Syms 1999	FIB ablation	-5%	Not reported	Not reported	yes	*Q* degradation
Enderling, 2007	FIB deposition	-15,5%	6.4%/μm	7,000	yes	*Q* degradation, resolution
Chang, 2013	FIB-CVD	-12%,+7%	Not reported	Not reported	To be demonstrated	Prepackaging
Joachim, 2003	Polysilicon CVD	+1.96%	Not reported	Not reported	no	Prepackaging, control
Wang, 1997	Localized annealing	2.7%	16ppm	41,000	To be demonstrated	prepackaging
Hajjam 2012	Oxidation	3.7%	Not reported	Not reported	no	prepackaging
Remtema, 2001	Thermal stress	+6.7%	0.2%/mW	Not reported	To be demonstrated	*Q* degradation
Svilicic, 2015	Electrothermal	.13%	Not reported	415 (air)	To be demonstrated	Stress/Resolution

Syms, 1998	Thermal expansion	-25% +50%	Not reported	Not reported	To be demonstrated	Power consumption
Jun, 2006	Electrothermal	+10%	3%/μW	2,000	To be demonstrated	Stress
Manca, 2013	Phase change materials	+1.9%	475ppm/ μA	Not reported	To be demonstrated	Exotic materials
Challa, 2008	Magnetic forces	±20%	1%/μW	Not reported	To be demonstrated	Complicated fabrication
Sung, 2014	CNT Rope Synthesis	24%	0.5%	Not reported	No	Prepackaging
Enderling, 2005	Electrodeposition	±10%	2.5Hz/V	Not reported	No	Prepackaging
Peters, 2008	Mechanical stiffening	±15%	3.5Hz/V	Not reported	To be demonstrated	*Q* degradation
Leland, 2006	Compressive preload	-24%	Not reported	Not reported	To be demonstrated	*Q* degradation
Hosseinzadegan, 2013	Tip-based mass removal	0.4%	13ppm/μm^2	Not reported	To be demonstrated	*Q* degradation
Samarao 2011,	Metal diffusion	0.4%	Not reported	75,000	No	*Q* degradation

5.2.2 Tuning

Perhaps the most researched active frequency control method is the electrostatic tuning method [74, 75, 76, 77, 78, 79, 80, 81] which uses the electrostatic stiffness

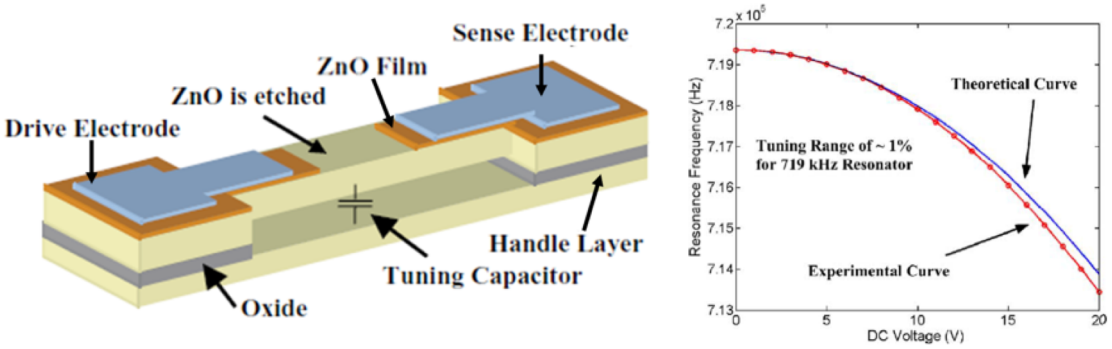

Figure 57: (left) *Q*-enhanced voltage-tunable piezoelectrically-transduced SCS resonator showing (right) downwards electrostatic fine-tuning characteristics

dependency on the applied voltage. This method is commonly used in MEMS owing to the high-aspect ratio (40:1) capacitive gaps that can be uniformly etched in single crystal silicon (SCS) [82]. This tuning technique has been applied successfully both to capacitively and piezoelectrically actuated devices [80]. However, small capacitive gaps are used to maximize the sensitivity of this frequency tuning method. While submicron gaps require stringent fabrication processes, small gaps increase squeeze-film damping and are not compatible with large dynamic range and large motion amplitude typically found in low-stiffness, high-*Q* devices. Other frequency control methods have been considered in the past decade to overcome the limits of the electrostatic tuning method (Figure 57).

5.2.3 Laser trimming: ablation and deposition

Another usual frequency trimming method consists in modifying the mass distribution of the resonator by either ablating or by depositing mass on the surface of the resonator. Laser-based mass modification methods [83, 84, 85] either increase or decrease the resonance frequency. In addition, these methods have a large trimming range (5%) and can show very small resolution, in the ppm range. Finally, laser-based trimming methods

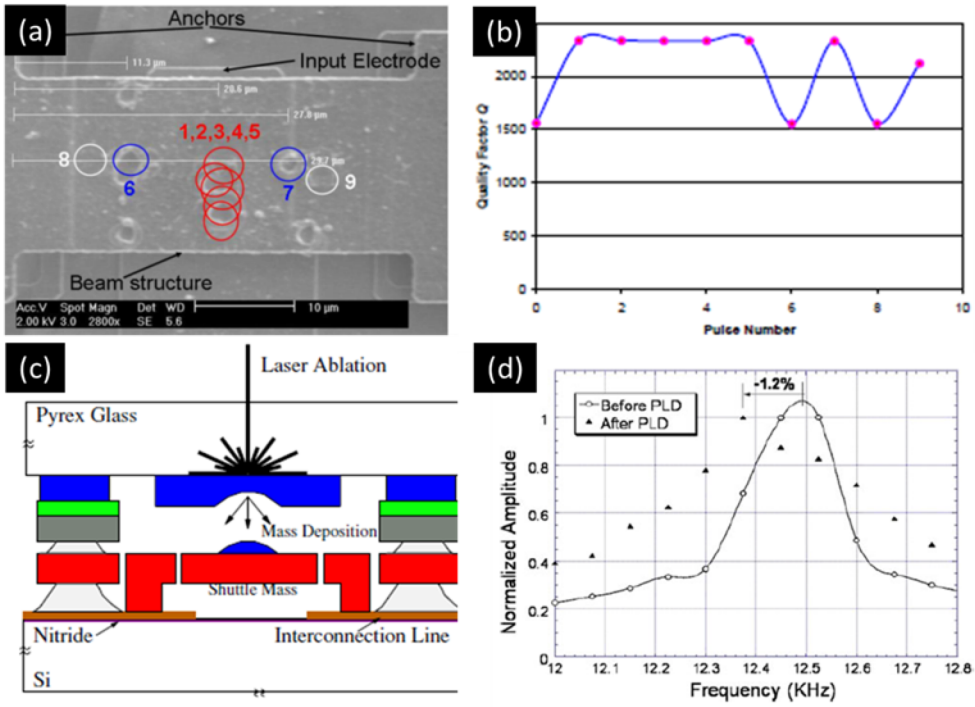

Figure 58: (a) Laser ablation of a MEMS resonator (b) Q-behavior through-out trimming. (c) Pulsed laser deposition of materials on a MEMS resonator with (d) frequency shift and *Q*-degradation

are location-dependent, and geometry-independent, making these methods versatile and universal. However, *Q*-degradation is a frequent drawback of these methods. While the quality factor *Q* can stay relatively constant if trimming is done in some precise locations, laser-based trimming of high-*Q* resonators is yet to be demonstrated (Figure 58).

5.3 Pulsed Laser Stiffness Trimming

5.3.1 Prior art

While this proposal has briefly covered previous work on the electrostatic tuning and on laser mass trimming, there exist a wide variety of other trimming techniques ranging from mass deposition and annealing techniques [86], FIB deposition and ablation [87,

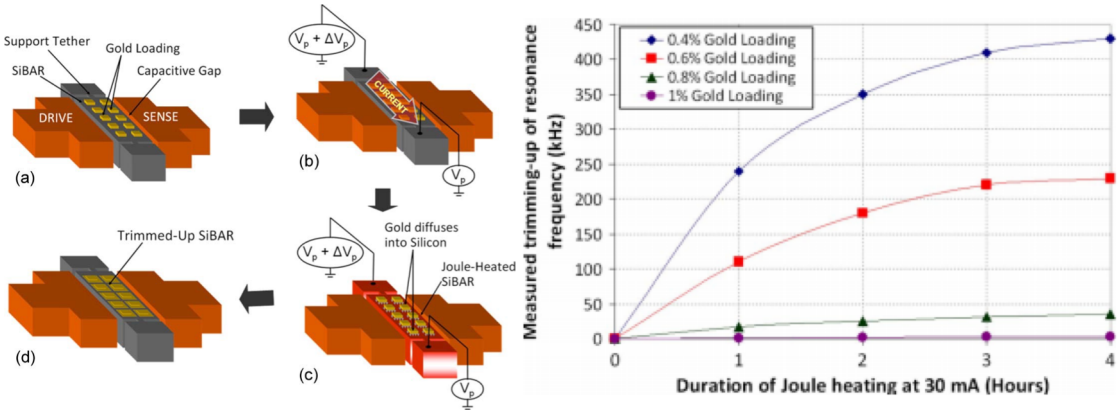

Figure 59: (left) Metal diffusion trimming via Joule heating (right) Permanent upward frequency trimming

88], CVD-based methods [89, 90], localized annealing and oxidation [91, 92] to thermal-based methods [93, 94, 95, 96]. In addition to these well-established methods, in the recent years, various other trimming methods have been investigated. Phase change materials [97], magnetic forces [98], CNT synthesis [99], electro-deposition [100], mechanical stiffening [101], compressive preloads [102], tip-based mass removal [103], and metal diffusion [104] are amongst these newly researched trimming methods. Table 8 presents a clear summary of the strength and drawbacks of each frequency trimming method.

Metal diffusion [104] is one particular new method which holds a great potential to trim high *Q* MEMS resonators and gyroscopes (Figure 59). Frequency trimming via metal diffusion-based is achieved by thermally diffusing a metal loading layer into the bulk of SCS. Upon cooling, after reaching high enough temperatures, formation of eutectic bonds between the diffused metal layer and SCS occur. These bonds have different mechanical properties compared to the Si-Si bonds that they replace. In particular, the Young's modulus of the eutectic alloy metal-SCS is usually different than the Young's modulus of

SCS. For example, if the loading metal is Al, then the Young's modulus is decreased in locations where the alloy Al-Si is formed, which will shift downwards the resonance frequency of Al-loaded SCS resonators trimmed by this method. Interestingly, the formation of eutectic bonds is a low temperature process in comparison to ablation. Ablation of SCS requires temperatures as high as the melting point of SCS (1414°C) whereas Al-Si bonds are formed at only 660°C. While irradiating the resonator with a laser only locally heats the material, it is challenging to ablate very small quantities of SCS at each single shot. While the resolution of mass trimming appears difficult to further decrease, the main drawback of laser-based mass trimming methods lies in the degradation of the quality factor. In comparison, metal diffusion presents a plurality of advantages owing to its low temperature process. Previous work in metal diffusion frequency trimming has used Joule heating to thermally diffuse the metal loading layer in the bulk of SCS. While this method is simple, it lacks both the flexibility and universality of laser-based heating. The preliminary research has combined the benefits of both metal diffusion and laser-based frequency trimming.

Gyroscope trimming calls for a different heating method to keep the advantage of a low thermal budget while being also mode selective. In the proposed heating approach, a laser beam heats certain spots on the device locally. Although the experimental setup complexity increases compared to Joule heating, laser heating offers substantial advantages. Most importantly, the user can aim the laser beam on any accessible location on the device to selectively modify the stiffness. Consequently, using a laser provides the possibility of substantially changing the resonance frequency of one mode while having negligible effect on the resonant frequency of the other mode. As mentioned before, not all

gyroscope modes can be trimmed by a laser-based eutectic technique; the degenerate modes are required to develop strain energy distributions with orthogonal high/low energy patterns and also high strain energy locations should be selectively accessible by the heat

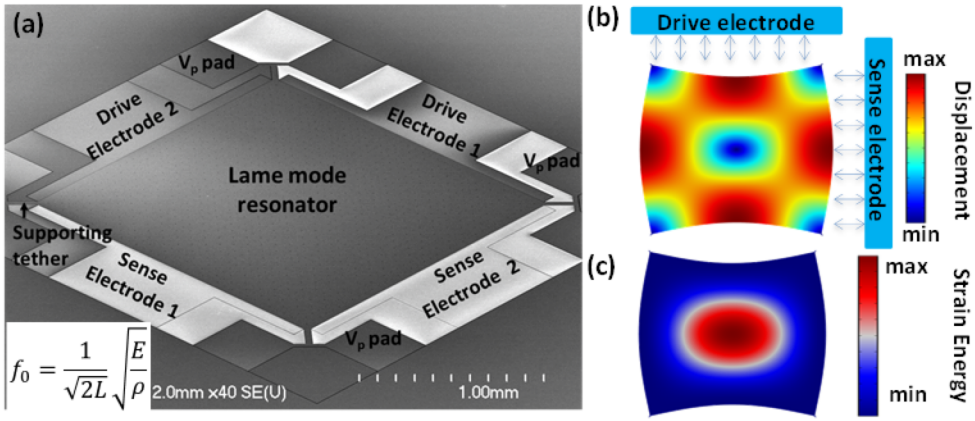

Figure 60: (a) SEM view (inset) precise frequency equation (b) actuation schematic and (c) locations with high strain energy (colored in red) contribute more to the trimming process than locations with low strain energy (blue)

source as described in previous section.

5.4 Frequency control of a high *Q* Lame mode

The literature survey indicates that there are currently few trimming methods that have been investigated and proven to maintain high Q values. Perhaps the most noticeable effort in developing a high-Q compatible trimming method is based on metal diffusion in the bulk of the SCS resonator and on the induced frequency shift due to the formation of metal-SCS bonds [104]. However, the heat source employed in the previous work (e.g. Joule heating) is not compatible with mode-matching MEMS gyroscopes. Mode-matching requires location-dependent frequency trimming [105]. Hence, a natural extension of

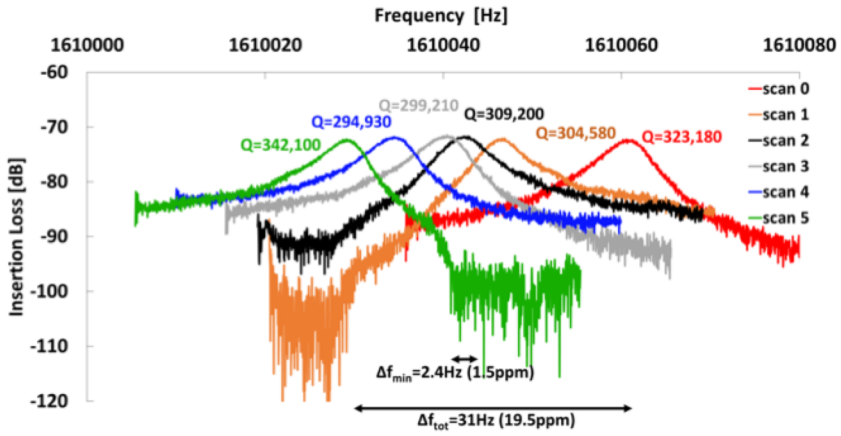

Figure 61: Precise downward trimming in the range of 1-4ppm is achieved routinely during each trimming scan. Further scanning the surface with the UV laser would extend the 20ppm frequency shift

previous work was to replace the Joule heating method by a UV laser. Laser-based eutectic trimming has the potential to mode match gyroscopes.

Mode matching of a high-*Q* MEMS gyroscope is particularly tricky to achieve. Preliminary work first focused on proving that this new laser-based method could effectively trim the resonance frequency of SCS MEMS resonators (Figure 60). Also, a new trimming material, germanium (Ge), has been introduced to further expand the properties of eutectic trimming. Pulsed laser stiffness trimming was first demonstrated on square-shape, flat Lamé mode resonators. It is well established [37, 38, 106, 51] that the Lamé mode resonators can be optimized to reach high *Q*s and concentrate the strain energy at the center of the device. The simple distribution of the strain energy facilitates the study pulsed laser stiffness trimming.

In previous work [104], stiffness was modified by metal-diffusion followed by formation of metal-SCS bonds in the bulk of SCS. In this work, a thin layer of Ge is

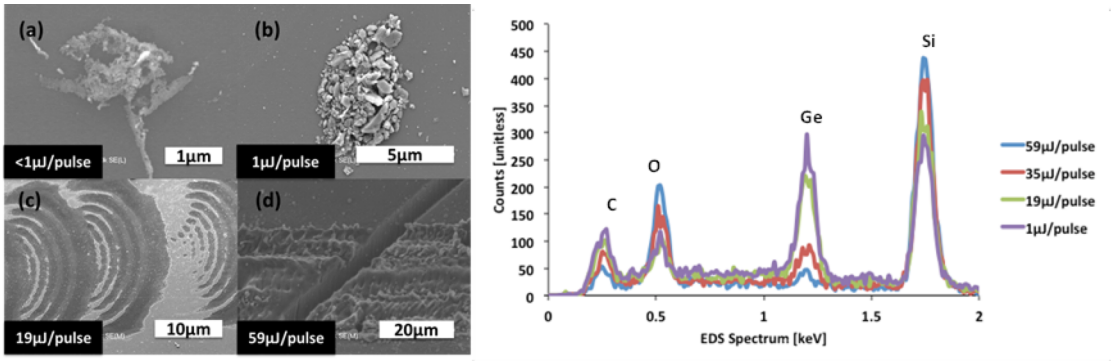

Figure 62: (left) Low laser power (a, b) induces crystallization of Si-Ge hetero-epitaxial crystals while higher power induces melt (c) and ablation (d) Stiffness trimming occurs at low laser power (a, b) while mass trimming occurs at high laser power (c, d) (right) EDX measurement show that the amount of Ge decreases with increasing laser power when melt and ablation occurs.

sputtered on the top of a released SCS resonator. Ge, like aluminum (Al), is a CMOS compatible material which forms a binary system with SCS. The microcrystal Ge-Si, like the alloy Al-Si, has a lower Young's modulus than SCS. In particular, the Young's modulus decreases proportionally to the concentration of Ge in the microcrystal Ge-Si [107].

This preliminary research has found that rough islands are formed due to the lattice mismatch between SCS and Ge. While formation of rough islands may degrade ultra-high-*Q*s, no significant degradation of high *Q* values ($Q \approx 300{,}000$) have been observed during either deposition of Ge thin films or during pulsed laser stiffness trimming (Figure 61). During pulsed laser stiffness trimming, the resonance frequency of the Lame mode decreases with the number of scans. This downwards frequency shift behavior was expected given the expression of the resonance frequency of the Lame mode and the expression of the Young's modulus of the SiGe microcrystal.

Unlike Al [104], sputtered Ge thin-film was not found to diffuse in the bulk of the SCS wafer during the trimming operation. Instead, the irradiation of the pulsed excimer

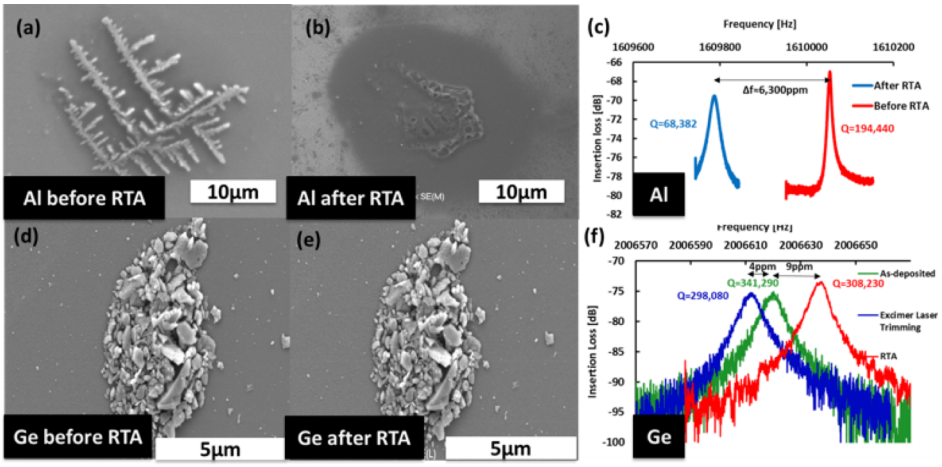

Figure 63: (a, b) Si-Al eutectics are formed during RTA (450°C for 30min) inducing (c) ~6,300ppm of undesired downward frequency shift and the severe degradation of the quality factor. (c, d) Si-Ge stayed stable during RTA

laser (wavelength of 349nm) on the 25nm-thick Ge thin film sputtered on top of a 40µm-thick SCS layer induced the formation of micro-crystals at low laser power. At close vicinity of the irradiation location, SEM observations reveal no visible alteration of the nearby Ge (Figure 63).

Stiffness trimming, contrary to mass trimming, does not redeposit any trimmed material since no material is ablated. This feature might be critical in low pressure environments (e.g. in post-packaged devices) where heated material tend to sublimate at low pressures. If the laser power is too important, then the trimming process turns into pulsed laser mass trimming. Laser fluence characterization prior trimming is necessary to operate the excimer laser at low power densities to avoid undesired mass trimming and uncontrolled ablation and material re-deposition. EDX measurements indicate that the relative amount of Ge stays stable at low laser power while it decreases at higher laser

power. The exact nature of the micro-crystals (orientation, texture) will be investigated in future work.

In particular, pulsed excimer laser annealing of Ge thin films on SCS routinely produces small (e.g. as small 1.5ppm) permanent frequency shifts (Figure 61). Additionally, this trimming technique has the potential to shift frequencies with ppb-level resolution. Indeed, in this preliminary work, the laser spot was scanned over large areas. Also, duration and power of the irradiating beam can be further reduced to decrease the formation of SiGe micro-crystals and thus to reduce the magnitude of the frequency shift during each scan. Perhaps, ppb frequency shift could be measured with this trimming method if our experimental set-up could measure even smaller frequency shifts.

Even though Al and Ge are CMOS compatible materials, Al, unlike Ge, diffuses in SCS at 450°C, the maximum allowable temperature of CMOS processes. Unlike Al, Ge does not induce any undesired trimming when heated in the RTA chamber at 450°C for 30 minutes. These processing conditions are typical of low temperature packaging processes. Under SEM observation, the micro-crystal remained completely stable after RTA (Figure 63). Capacitive measurements confirm the SEM observation; the small upward frequency shift (13ppm) is not a consequence of undesired trimming. Undesired trimming would have decreased the resonance frequency. Since this particular device is anchor-loss limited, the upward frequency shift might be due to wire-bonding after RTA.

5.5 Frequency control of shell resonators

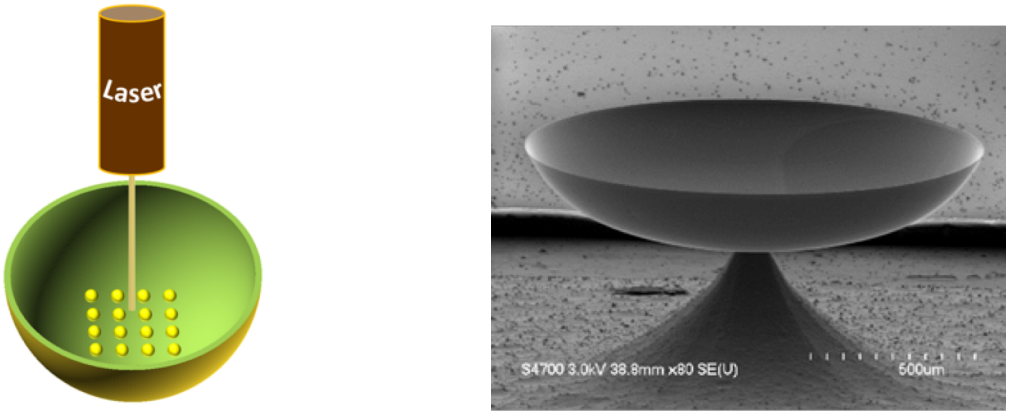

Figure 64: Representation of laser-based metal-silicon eutectic trimming method

The proposed eutectic trimming technique is founded upon the distribution of elastic strain energy on an anchored resonator, namely a hemispherical shell resonator (HSR) supported on a solid cylinder at the center. The method takes advantage of the fact that controlled modification of the Young's modulus at strategic locations with high strain energy densities would shift the resonant frequency significantly. An essential requirement for the method to work is that the strategic spots have to reside at different locations on the shell for the two degenerate modes, to ensure that the resonant frequency of each mode can be shifted individually with negligible effect on the other one. Also, these separated, high strain energy regions must be selectively accessible by a laser used as heating source.

A detailed discussion which follows, shows that the wineglass mode of an HSR (a mode with four nodal locations, also known as m=2), develops high strain energy areas around the support, which satisfy the aforementioned requirements for eutectic trimming.

5.5.1 Influence of the post on strain energy distribution

Abundant literature has studied hemispherical shell resonators mathematically and in great detail (Figure 64). But, the equation of motion and the strain energy distribution, to the best knowledge of the authors, are always derived with the assumption of no support. In this work however, finite element method (FEM) is employed to show that a significantly strong strain energy pattern is developed around the post, resulting from the interaction of the resonating shell and the solid support, which are suitable to be used for eutectic trimming.

Figure 65 depicts plots of the strain energy distribution of the m=2 wineglass mode along a nodal meridian for shells with and without support (green and blue curves respectively), using COMSOL Multiphysics FEM simulations. A hemispherical shell with a radius of 1250μm and thickness of 2μm supported on a solid post with a radius of 150μm is used as typical dimensions for a μHRG. Also, the strain energy distributions in cross-sectional view at the same nodal point are shown in the inset of Figure 65. The graphs show that although the strain energy distribution is modified only lightly around the top rim, it is significantly changed at the vicinity of the post, exhibiting a peak for the shell with a post. To take advantage of the strain energy density around the support for trimming purposes, strategic spots that offer the greatest trimming range, which will be referred to as eutectic trimming spots, should be looked for. Therefore, characteristics of the energy distribution is further studied through finite element modeling for the m=2 wineglass mode in the following subsections.

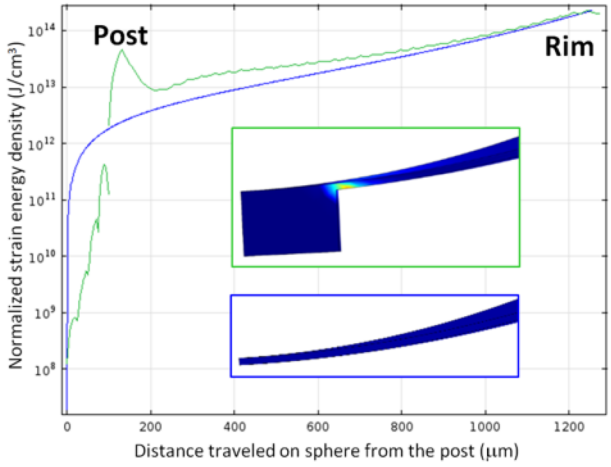

Figure 65: Strain energy distribution with a post (green) and without a post (blue) at a nodal line, inset: cross-section at a nodal-point of the strain energy distribution with a post, and without a post.

5.5.2 Strain energy patterns

The analytical description of the mode shapes of a pure hemispherical shell resonator implies that any point on an antinodal meridian would only comprise polar and radial displacements, whereas any point on a nodal meridian would only involve azimuthal displacement. The addition of a solid post ideally enforces the anchored region to be immobile. It is the interaction among atoms belonging to the mobile areas and fixed areas around the post that produces high strain density regions at the nodal and antinodal points as shown in Figure 66.

5.5.2.1 Modes of resonance

The strategic eutectic trimming spots for a given mode of vibration have been defined as the locations on the shell where large strain energy densities are developed. Figure 66 gives an insight on the patterns and polar distributions of strain energy generated

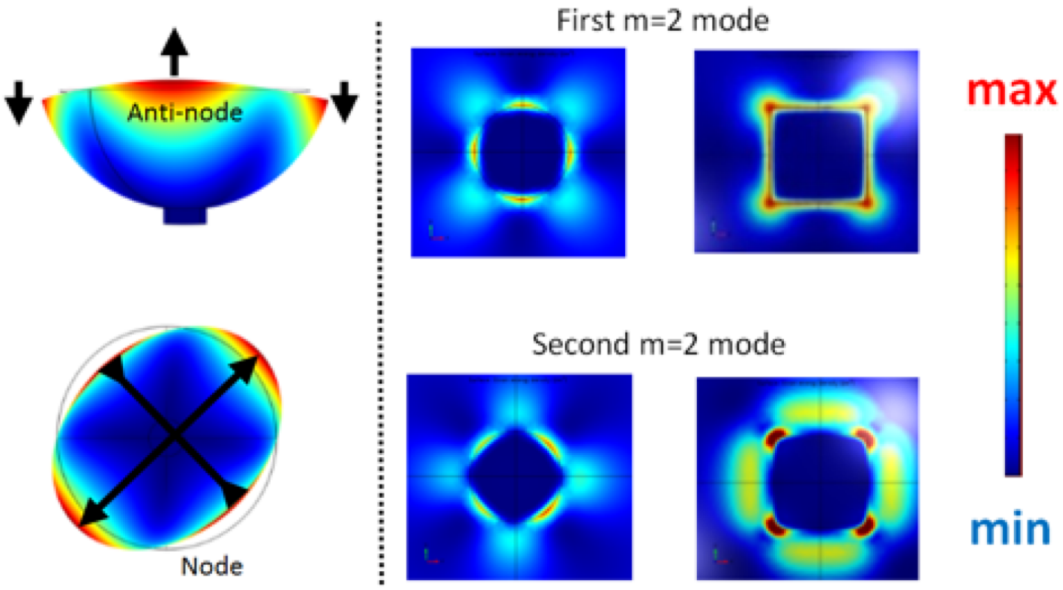

Figure 66: (left) displacement of the m=2 resonant mode at high and low frequencies, (center) Strain energy density around a circular post for both m=2 modes, (right) Strain energy density around a square post for both m=2 modes

at the antinode of the rocking mode, the m=2, 3 and 4 modes. The rocking mode generates the largest amount of strain energy and thus the strategic spots of the rocking mode are the most effective amongst all. Yet, the two degenerate rocking modes have very similar distributions, which implies that they will be equally affected by any stiffness change. Therefore, the resonant frequencies will be strongly shifted during the trimming operation, but the frequency split will not significantly change.

According to Figure 67, the wineglass m=2 mode generates the second largest strain energy density, but since it generates less strain energy than the rocking mode, the trimming sensitivity is smaller. The same conclusion applies to the m=3, 4 and higher order modes, but based on FEM simulations, these modes develop much smaller strain energy densities making them not the suitable candidates for eutectic trimming (the frequency

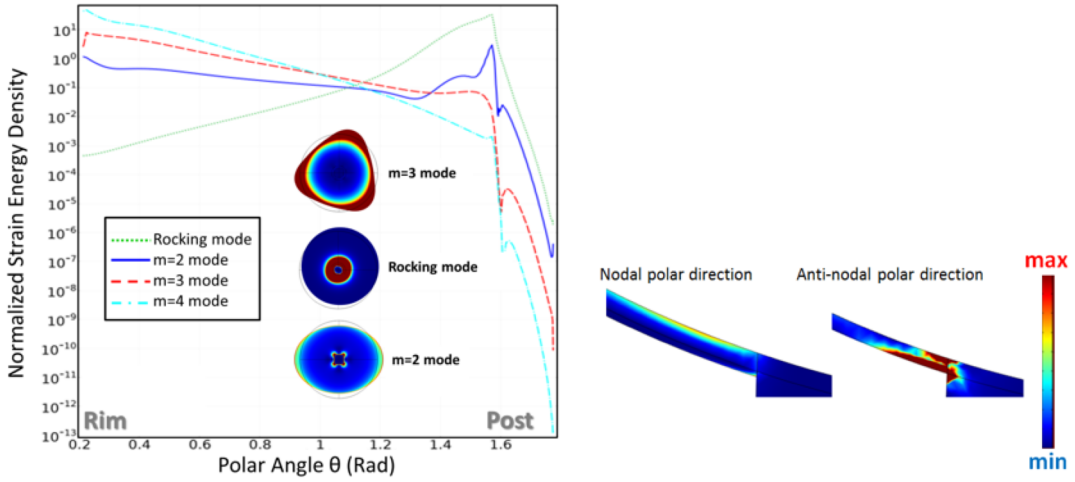

Figure 67: Normalized strain energy for different mode shapes on the same meridian. Inset: strain energy distribution at the top surface of the shell for different modes of vibration (left) Strain energy along the thickness at a node (left) and an antinode (right)

shifts are lower than the numerical error of around 0.1 Hz). Furthermore, per Figure 66, the strain energy for the pair of degenerate m=2 modes slightly overlap. Therefore, it is possible to shift the frequencies independently, and increase or decrease the frequency split between the two m=2 modes by controlled local stiffness modifications.

5.5.2.2 Fine and coarse trimming regions

The strain energy distribution is not constant over the thickness of the shell as shown in Figure 67. For example, the largest amount of strain energy is produced at the backside of the shell, at antinodal locations. Although the nodes of one of the m=2 modes and the antinodes of the other m=2 mode are located in the same azimuthal regions, the strain energy patterns generated by the nodes and antinodes are not exactly the same. Therefore, the locations of strategic eutectic trimming spots for the nodes and those for the antinodes are different; the nodes generate spots that are further away from the post

compared to the spots generated by the antinodes. Furthermore, the antinodes generate eutectic trimming spots with larger strain energy densities than what nodes do. Therefore, the most sensitive locations for eutectic trimming (the spots that generate the largest frequency shifts, suitable for coarse trimming) correspond to the backside of the shell, at the anti-nodal locations on the shell post edge.

5.5.3 Eutectic trimming spot dimensions

In Figure 68, the strain energy distribution is given with the polar angle for different support sizes. The peaks of the graphs represent the maximum energy developed at the proximity of the support, and the results imply that the peaks are approximately developed around the same polar angle away from the post for different support sizes. Furthermore, the widths of the peaks, which can be interpreted as the sizes of effective trimming regions, are also about the same for the given range of support sizes. However, the maximum strain energy density, which represents the total strain energy developed around the post vary with the support size.

The top curve in Figure 68 (green triangles) depicts the dependence of maximum strain energy density developed around the post on support size. In accordance with the results given in Figure 68, larger strain energies correspond to bigger support sizes, approximately showing an exponential dependence. The lower curve in Figure 68 (orange diamonds) gives the frequency split caused by stiffness change on the effective trimming spots. The fact that larger frequency shifts are generated for larger support sizes, confirms that the sensitivity of trimming areas are higher for larger posts. Therefore, although a larger post does not create larger eutectic trimming regions, it does create trimming spots

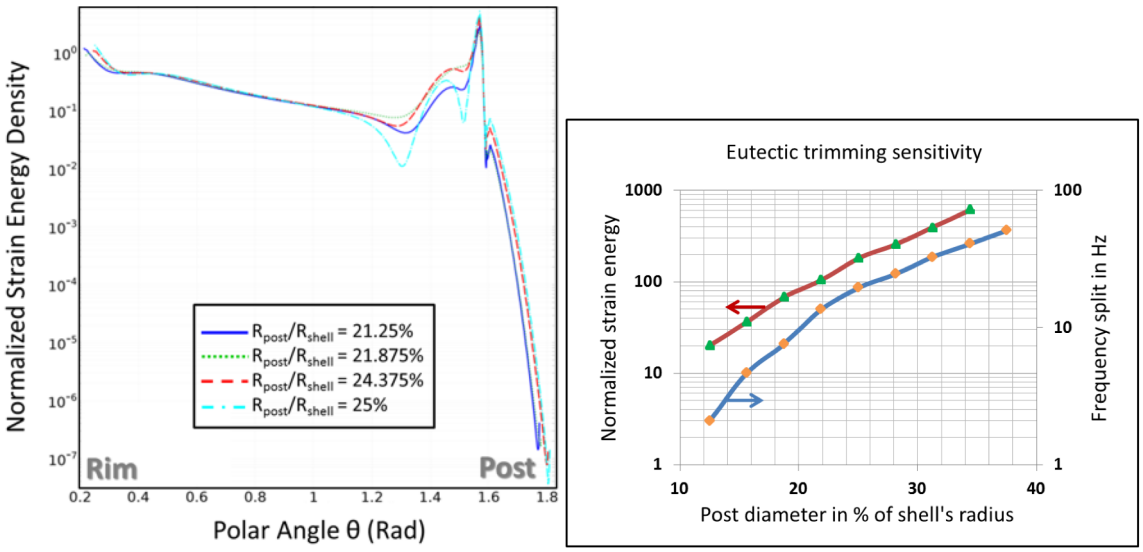

Figure 68: Evolution of trimming effective area for increasing post size, in % of the shell's fixed radius. The curves have been shifted so that the junction of the post and the shell is at a fixed angle to allow direct comparison of the strain energy curves. (right) Eutectic frequency trimming range increasing with increasing post size (diamond line) Maximum of strain energy density increasing with increasing post size (triangle line)

that are more sensitive to stiffness modification, and can potentially provide larger frequency shifts.

5.5.4 Localized eutectic trimming

Eutectic trimming of micro-resonators using Joule heating has been previously reported by our group. Laser-based eutectic trimming is based on stiffness modification and can be done over the entire resonating body or only at targeted locations. This technique builds on the well-established area of eutectic wafer bonding for MEMS fabrication and packaging. To realize eutectic trimming, a thin layer of trimming material such as gold or aluminum is deposited on the resonator surface, and is thermally forced to diffuse into the device to create eutectic bonds with the bulk material (i.e. polysilicon), at

locations where the temperature reaches a target value. The stiffness modification and the resultant frequency shifts are functions of the size and the location of these eutectic bonds. The minimum temperature needed for formation of eutectic bonds (i.e. the eutectic temperature) can be significantly lower than the melting temperatures of both materials. The thermal budget for eutectic trimming is thus much smaller compared to laser ablation trimming methods.

5.5.4.1 Frequency trimming

Based on the analysis presented in previous sections, the wineglass (m=2) mode of a μHRG develops effective eutectic trimming areas around the post with high strain energy densities for one mode and low strain energy for the other one. Additionally, a large strain energy difference befits coarse trimming, whereas a small strain energy difference is suitable for fine trimming. The strain energy patterns shown on the right side of Figure 69 indicate that there are two sets of locations around the post where large differences between the energy densities of the two modes are developed. These two sets of locations around the post are shown on the left side of Figure 69. A thick (respectively thin) ring around the metal's name represents a location that provides a large (respectively small) difference of strain energy. Accordingly, the regions around the post can be classified into two categories: one that provides large strain energy differences, which will be referred to as coarse trimming locations and another that provides smaller differences, which will be referred to as fine trimming locations.

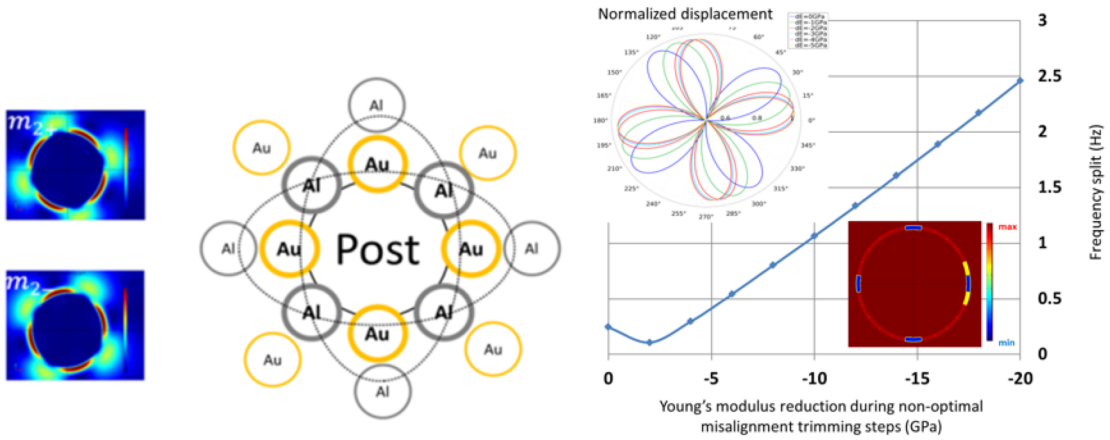

Figure 69: Relative position of gold and aluminum eutectic trimming locations (right) Non-optimal misalignment trimming after frequency split trimming by over 10X, top inset: modal displacement during misalignment trimming, bottom inset: misalignment trimming location (yellow) compared to frequency trimming location (blue)

5.5.4.2 Misalignment trimming

For maximum gyroscope sensitivity, the nodes and antinodes of the degenerate modes must be aligned with the center of the drive (actuation) and sense electrodes. Localized eutectic trimming has the capability to reduce the mode misalignment, which for example can be caused by minute tilting of the post. Our FEM analysis shows that both four-node wineglass modes are equally sensitive to any stiffness variation applied to locations around the post halfway between the nodal and anti-nodal points. And, that misalignment trimming can be done at these locations with small effect on the frequency split. In Figure 69, the Young's modulus is modified at non-optimal locations where the modes are realigned: the low frequency m=2 mode was aligned from 130° direction to the 95° direction. Due to the non-optimal condition of this example, the frequency split is also affected and increases from 0.2 Hz to 2.5 Hz for a Young's modulus variation of only

20GPa. In the next section, the same device will have its mode realigned by using optimal locations for the trimming operation and the frequency split will not increase as much.

5.5.4.3 Choice of trimming material

Since this section focuses on the trimming of a polysilicon μHRGs, gold and aluminum are considered as candidates for trimming material because they offer specific advantages when forming eutectic bonds with polysilicon. Gold-silicon has a low eutectic temperature (363°C) compared to gold's melting temperature (1063°C). The Young's modulus of gold silicon eutectic compound is higher than that of polysilicon. Aluminum-gold has a eutectic temperature (577°C) that is close to aluminum's melting temperature (660°C), and a reduced Young's modulus compared to silicon. In the proposed method, aluminum-silicon eutectic bonds are formed at the trimming spots of the higher frequency mode (Fig. 9), which would reduce the Young's modulus from 160GPa (polysilicon) to 80GPa (aluminum-silicon eutectic). Although this stiffness reduction decreases the two m=2 frequencies, the higher frequency will be more sensitive to that stiffness modification, because of the location of the trimming spots, and therefore the frequency split will be reduced. Similarly, the formation of gold-silicon eutectic bonds at the trimming locations of the low frequency wineglass mode reduces the frequency split.

5.5.5 Trimming algorithm

A simple and efficient frequency trimming algorithm is devised and is shown in Figure 70. The first step is to find effective trimming locations around the post; an area

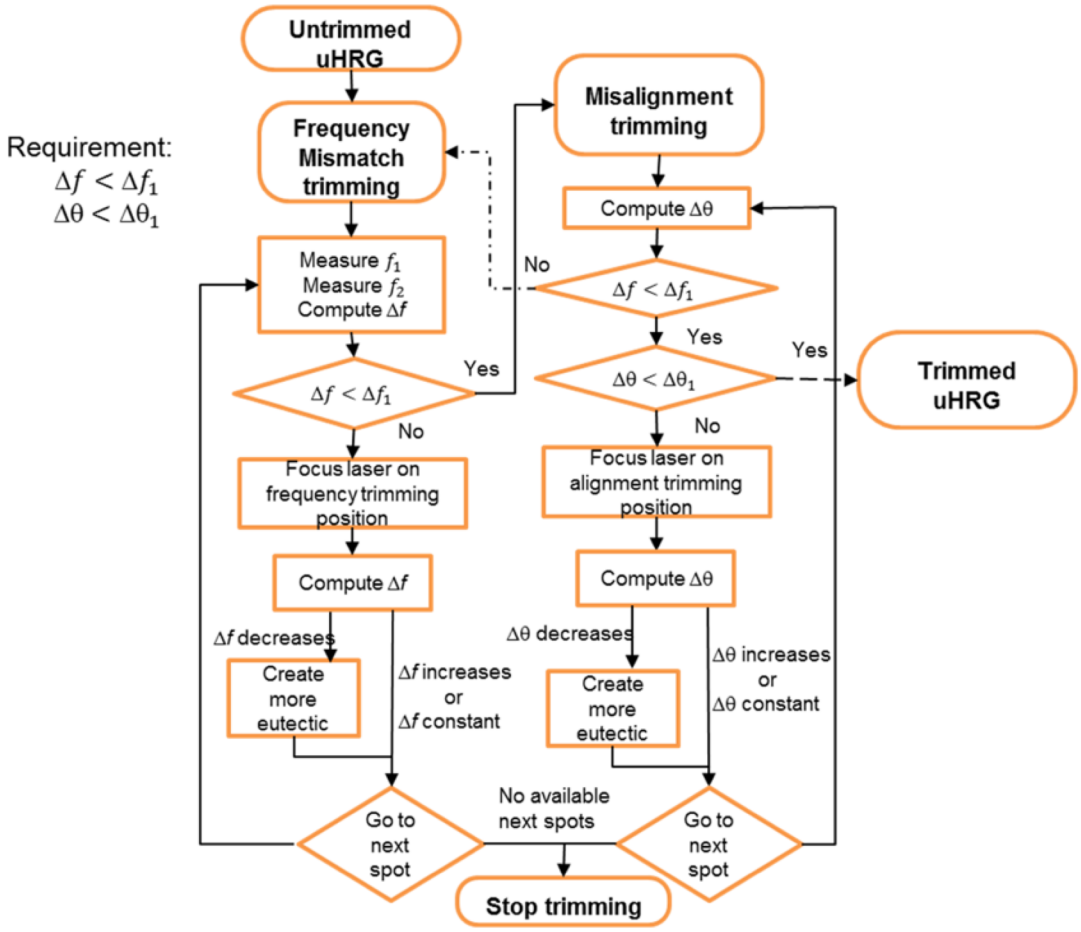

Figure 70: Flowchart of the algorithm proposed for eutectic trimming, where Δf_1 is the required frequency split and $\Delta\theta_1$ is the required misalignment angle

which is usually not accurately known since the post is not visible from the top. This will be done through a repetitive process which can be turned into an automated operation.

5.5.5.1 Finding the trimming locations

The laser is initially aimed at a location as close as possible to the center of the post from the top. Weak laser shots are aimed on the μHRG to create localized eutectics bonds, and the frequency split is recorded at each step. The trimming locations can then be found

by studying the frequency split evolution. Increasing the step resolution assures that all the trimming locations are visited. The laser scans around every trimming location to map more precisely the frequency split reduction with spatial stiffness modification. Laser shots will start creating eutectics in the middle of the post where the frequency split is not affected and then will be aimed outwards in the polar direction, until the location limits are found.

5.5.5.2 Eutectic trimming flowchart

If the measured frequency split does not meet the requirements, then the algorithm continues to the next trimming location and creates more eutectic bonds until the frequency requirements are met or until there is no further reduction. In the latter case, the algorithm will proceed to the next trimming spot. If the frequency split requirements are met, the algorithm will then trim misalignment by visiting the misalignment trimming locations. The algorithm will loop back to do frequency trimming if the frequency split does not meet the requirements anymore. The algorithm converges when the device is trimmed both for frequency split and misalignment or when all the trimming locations are used.

5.5.5.3 Numerical Results

Figure 71 shows the automatic eutectic trimming of a μHRG resulting from an FEM simulation. To simplify the numerical analysis, a uniform Young's modulus across the thickness of the shell is assumed. We consider the diameter of the effective trimming area to be 20 μm for a shell with a 1 mm diameter which is 2 μm thick. An initial frequency split of 40Hz between the m=2 elliptical modes frequencies is reduced to 0.1 Hz. The four

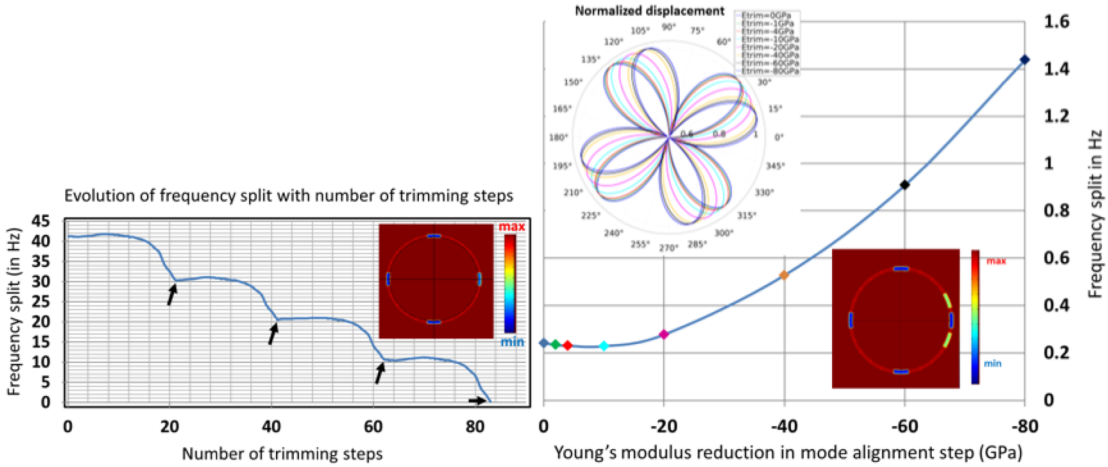

Figure 71: Reduction of the frequency split using eutectic trimming by a factor >10X (right) Optimal misalignment trimming after frequency split trimming by over 10X, top inset: modal displacement during misalignment trimming, bottom inset: misalignment trimming location (yellow) compared to frequency trimming location (blue)

strong variations of the frequency split (graph in Figure 71) are due to trimming operation on the coarse trimming locations (blue spots in the top-right image of Figure 71). When the modes are aligned, the frequency split is reduced by 10X.

CHAPTER 6. CONCLUSIONS AND FUTURE WORK

6.1 Conclusions

This dissertation has covered three main topics: 3D SiO2 shell resonators, ultra-high *Q* SiC disk resonators and precise frequency control of high *Q* Si resonators. Though these topics seem disparate, they all concur in realizing the next technological platform for micro-scale ultra-high performance inertial sensors. It is difficult not to wonder, when looking back at all this work, how much did this thesis contribute to establishing the state-of-the-art. The following paragraph is meant to concisely put forward how this thesis contributed to the state-of-the-art. The most notable conclusions from this work are that 1/ 3D shell resonators have their *Q* limited by surface loss which can be somewhat improved by thermal annealing and that 2/ it is possible to etch high-aspect ratio SiC trenches with smooth and vertical profiles which will enable integrated environmentally-robust SiC MEMS resonators. The contributions of this thesis are as follows:

1. Developed a fabrication process to make atomically-smooth shells to reduce energy dissipation in thin-film shells due to surface effects. This process is foundry-friendly and tackles the daunting task of extreme miniaturization of the HRG without sacrificing on performance. The author established that, empirically and regardless of the fabrication process, a shell's performance scales with its stiffness, making comparison of performance between large and high-stiffness shells compared to small and low-stiffness shells an unfair comparison. If the figure of

merit takes the shell's stiffness into account, then these shells are on par with their upsized counterparts.

2. Provided experimental results proving that surface effects are limiting the Q-factor of thin-film low-frequency resonators. By anchoring the shell resonators to the top rim, rather than at the bottom like it is traditionally done, this new anchoring design enabled to easily reveal how significant surface loss is in limiting the overall Q-factor in shell resonators.
3. Developed SiCOI platform (SiCOI bonding, SiC DRIE) towards Akhiezer-limited quality factors in BAW SiC disk gyroscopes. This effort has been substantial because the field of SiC DRIE is nascent and almost everything has to be done, ranging from making custom SiCOI wafers that meet fabrication specifications to developing new SiC etching recipes in a not-so-robust ICP etcher. In these efforts, I have been training and mentoring Jeremy Yang, who has been instrumental in designing SiC resonators at first and then making SiC resonator. Our work and contributions here are intermingled. He has contributed a lot to this effort. The core idea of the design behind achieving high Q-factors in SiC disk resonators is under a pending U.S. patent: U.S. Patent Application No. 62/638,494, March 5, 2018, "Method to Acoustically Decouple MEMS Devices", (GTRC Reference No.: 7843).
4. Developed a post-fabrication frequency control technology to tune the resonance frequency of MEMS sensors with record resolution. This frequency control technology tunes bulk modes with ppm accuracy and flexural modes with thousands of ppm tuning range while maintaining steady Q-factors. This frequency

control technology is patented under U.S. Patent Application No.: 15/875,943 SYSTEMS AND METHODS FOR STIFFNESS TRIMMING OF RESONATORS Filed: January 19, 2018

6.2 Future work

This work can be extended along numerous directions. The most pressing direction is to operate the SiC BAW disk resonators with ultra-low dissipation as integrated capacitively-transduced resonant gyroscopes. This work has shown both the fabrication of smooth trenches and ultra-high *Q* gyroscopic modes, indicating that SiC BAW gyroscopes are tantalizingly close. The immediate challenge is to maintain the same *Q*-factors while surrounding the SiC BAW disk resonators with nano-scale gaps using a process similar to HARPSS. Several key differences in processing (e.g. poly-silicon for ohmic contact, CTE mismatch, SiC DRIE) makes it challenging to directly apply HARPSS to SiC. The second challenge resides in mode-matching ultra-high *Q* BAW disk gyroscopes. Large transductions gaps are needed to drive the resonators sufficiently hard considering its high *Q*-factor. However, large transduction gaps limit the tuning force. Therefore, permanent trimming to augment tuning will be needed.

Permanent frequency trimming of ultra-high *Q* resonators will be a key step in future efforts. In this work, pulsed laser stiffness trimming was developed using a nanosecond laser. It is possible that femtosecond laser will crystallize the metal-silicon eutectic binary system without forming dendrites due to the short duration of the laser pulse and the lack of thermal energy transfer to locations surrounding the laser. Besides migrating from a nanosecond laser to a femtosecond laser, PLST needs to be demonstrated on a packaged

device. Some expected challenges, that have been partially addressed in this work, include: frequency trimming after packaging, selecting trimming locations on the fly depending on frequency measurements and most importantly verifying the amount of dissipation that stiffness trimming introduces.

On the 3D SiO_2 shallow shell side, surface loss has been identified in this work as the limiting loss mechanism. At least two independent routes can be explored to circumvent the limit set by surface loss. Thermal annealing and terminating the surface constitutes the first route. Based upon similar work on silicon wafers, improvement up to 5-10X could be expected, although these improvements are time dependent. After a certain amount of time, Q usually degrades back to its original value. Another route consists in using intermodal coupling to enhance the amount of stored energy. Because of their low stiffness, shallow shell resonators can be easily driven into non-linearity which enables intermodal coupling.

BIBLIOGRAPHY

[1] DARPA. [Online]. Available: http://www.darpa.mil/program/micro-technology-for-positioning-navigation-and-timing. [Accessed September 2015].

[2] D. Rozelle, "The hemispherical resonator gyro: From wineglass to the planets," in *AAS/AIAA*, 2009.

[3] A. Meyer et al., "Milli-HRG inertial navigation system," in *IEEE/ION PLANS*, 2012.

[4] P. Shao et al., "A 3D-HARPSS polysilicon hemispherical shell resonating gyroscope: design, fabrication and characterization," *IEEE Sensors Journal,* vol. 15, no. 9, pp. 4974-4985, 2015.

[5] J. Cho et al., "130 second ring-down time and 3.98 million quality factor in 10 kHz fused silica micro birdbath shell resonator," in *Solid-state sensors, actuators and microsystem workshop*, Hilton Head, 2016.

[6] R. Lifshitz et al., "Thermoelastic damping in micro and nanomechanical systems," *Phys. Re. B,* vol. 61, no. 8, pp. 5600-5609, 2000.

[7] A. Darvishian et al., "Anchor loss in hemispherical shell resonators," *JMEMS,* vol. 26, no. 1, pp. 51-66, 2017.

[8] M. Weinberg, "How to invent (or not invent) the first silicon MEMS gyroscope,," in *Inertial*, 2015.

[9] D. Serrano et al., "Substrate-decoupled, bulk-acoustic wave gyroscopes: Design and evaluation of next generation environmentally robust devices," *Microsystems and Nanoengineering,* vol. 2, no. 16015, 2016.

[10] J. Bernstein et al., "High *Q* diamond hemispherical resonators: fabriation and energy loss mechanisms," *JMM,* vol. 25, 2015.

[11] J. Cho et al., "Fused silica micro birdbath resonator gyroscope," *JMEMS,* vol. 23, pp. 66-77, 2014.

[12] J. Gray et al., "Hemispherical micro-resonators from atomic layer deposition," *JMM,* vol. 12, no. 1, 2014.

[13] B. Hamelin, V. Tavassoli and F. Ayazi, "Highly-symmetric silicon dioxide shallow shell resonators with angstrom-level roughness," *Sensor 2015,* 2015.

[14] N. Mehanathan et al., "Invar-36 micro hemispherical shell resonators," in *IEEE MEMS 2014*, San Francisco, 2014.

[15] S.-D. Ko et al., "High *Q* monocrystalline silicon carbide disk resonators fabricated using DRIE of thick SiC-on-Insulator substrates," in *IEEE MEMS 2018*, Belfast, 2018.

[16] R. Tabrizian et al., "Effect of phonon interactions on limiting the f.*Q* product of micromechanical resonators," in *Transducers*, 2009.

[17] M. Weinberg et al., "Energy loss in MEMS resonators and the impact on inertial and RF devices," in *Transducers*, 2009.

[18] A. Ghadimi et al., "Elastic strain engineering for ultralow mechanical dissipation," Science **360**, 764 (2018)

[19] V. B. Braginsky, Systems with Small Dissipation, he University of Chicago Press, 1985.

[20] S. Ghaffari et al., "Accurate modeling of quality factor behavior of complex silicon MEMS resonators," *JMEMS,* vol. 24, no. 2, pp. 276-288, 2015.

[21] A. Heidari, M.-L. Chan, H.-A. Yang, G. Jaramillo, P. Taheri-Tehrani, P. Fonda, H. Najr, K. Yamazaki, L. Lin and D. Horsley, "Micromachined Polycrystalline Diamond Hemispherical Shell Resonators," *Transducers 2013,* 2013.

[22] S. Singh et al., "Design and fabrication of high-*Q* birdbath resonator for MEMS gyroscopes," in *IEEE/ION PLANS*, 2018.

[23] R. Mirjalili et al., "Substrate-decoupled silicon disk resonators having degenerate gyroscopic modes with *Q* in excess of 1-million," in *Transducers*, Anchorage, 2015.

[24] F. Ayazi, "Multi-DOF inertial MEMS: from gaming to dead reckoning," in *TRANSDUCERS 2011*, Beijing, 2011.

[25] A. Sharma, M. Zaman and F. Ayazi, "A Sub-0.2/hr Bias Drift Micromechnical Silicon Gyroscope With Automatic CMOS Mode-Matching," *IEEE Journal of Solid-State Circuits,* vol. 44, no. 5, pp. 1593-1608, 2009.

[26] V. Gokhale et al., "Approaching the intrinsic quality factor limit for micromechanical bulk acoustic resonators using phononic crystal tethers," *Appl. Phys. Lett.,* vol. 111, p. 013501, 2017.

[27] A. Akhiezer, "On the absorption of sound in solids," *J. Ohys. (Moscow),* vol. 1, no. 4, pp. 277-287, 1939.

[28] L. D. Landau, "On the absorption of sound in solids," *Phys. Z. Sowjetunion,* vol. 11, pp. 18-25, 1937.

[29] A. Duwel et al., "Engineering MEMS resonators with low thermoelastic damping," *JMEMS,* vol. 15, no. 6, pp. 1437-1445, 2006.

[30] Z. Hao et al., "Support loss in the radial bulk-mode vibrations of center-supported micromechanical disk resonators," *Sensors and Actuators A,* vol. 134, pp. 582-593, 2007.

[31] B. Kim et al., "Temperature dependence of quality factor in MEMS resonators," *JMEMS,* vol. 17, no. 3, pp. 755-766, 2008.

[32] M. Roukes et al., "Nanoelectromechanical systems," in *Hilton Head, 2000*.

[33] Y. Tsaturyan et al., "Ultracoherent nanomechanical resonators via soft clamping and dissipation dilution," *Nat. Nanotechnol.,* vol. 12, no. 8, p. 101, 2017.

[34] B. Hamelin et al., "A test vehicle to study surface loss," in *IEEE MEMS 2017*, 2017.

[35] D. Bindel et al., "Elastic PMLs for resonator anchor loss simulation,," *Int. J. Num. Meth. Eng.,* vol. 64, pp. 789-818, 2005.

[36] V. Tavassoli et al., "Substrate-decoupled 3D micro-shell resonators," in *IEEE Sensors 2016*, Orlando, 2016.

[37] V. Thakar and M. Rais-Zadeh, "Optimization of Tether Geometry to Achieve Low Anchor Loss in Lame-Mode Resonators," *EFTF/IFC 2013,* pp. 129-132, 2013.

[38] J. Lee, J. Yann and A. Seshia, "Study of Lateral Mode SOI-MEMS Resonators for Reduced Anchor Loss," *Journal of Micromechanics and Microengineering,* pp. 1-10, 2011.

[39] L. Sorenson et al., "Effect of structural anisotropy on anchor loss mismatch and predicted case drift in future micro-hemsipherical resonator gyros," in *IEEE/ION PLANS*, 2014.

[40] L. Sorenson et al., "Bulk and surface thermoelastic dissipation in micro-hemispherical shell resonators," *JMEMS,* vol. 24, no. 2, p. 486, 2015.

[41] A. Peczalski et al., "IEEE J. Microelectromech. Syst.," *Investigation into the Quality factor of piezoelectric-on-Silica micromachined resonators,* vol. 24, no. 6, pp. 1695-1702, 2015.

[42] K. Yasumura et al., "Quality factor in micron- and submicron-thick cantilevers," *JMEMS,* vol. 9, no. 1, 2000.

[43] J. Yang et al., "Surface effects and high quality factors in ultrathin single-crystal silicon cantilevers," *Appl. Phys. Lett.,* vol. 77, pp. 3860-3862, 2000.

[44] B. Shiaria et al., "Surface effect influence on the quality factor of microresonators," in *Transducers*, Barcelona, 2013.

[45] Y. Wang et al., "Study on surface roughness improvement of fused quartz after thermal and chemical post-processing," in *Inertial*, 2016.

[46] L. Zhuravlev, "The surface chemistry of amorphous silica. Zhuravlev model," *Colloids and Surfaces A: Physicochemical and Engineering Aspects,* vol. 173, no. 1, pp. 1-38, 2000.

[47] P. Shao et al., "Electrical characterization of ALD-coated silicon dioxide micro-hemispherical shell resonators," in *IEEE MEMS 2014*, San Francisco, 2014.

[48] S. Iyer et al., "Mode- and direction-dependent mechanical energy dissipation in single-crystal resonators due to Anharmonic phonon-phonon scattering," *Phys. Rev. Appl.,* p. 034002, 2016.

[49] S. Ghaffari et al., "Quantum limit of quality factor in silicon micro and nano mechanical resonators," *Sci. Rep.,* vol. 3, p. 03244, 2013.

[50] C. Zener, "Theory of Internal Friction in Reeds," *Physical Review,* vol. 52, pp. 230-235, 1937.

[51] V. Rabinovich, R. Gupta and S. Senturia, "The Effect of Release-Etch Holes on the Electromechanical Behavior of MEMS Structures," *Transducers 1997,* 1997.

[52] S. Chandorkar et al., "Multimode thermoelastic dissipation," *J. of Appl. Phys.,* vol. 105, p. 043505, 2009.

[53] S. Choi et al., "Thermoelastic damping of inextensional hemispherical shell," *Proc. World Academy of Science, Engineering and Tech- nology,* vol. 56, pp. 198-203, 2009.

[54] R. Abdolvand et al., "Quality factor in trench-refilled polysilicon beam resonators," *J. Microelectromech. Syst.,* vol. 15, no. 3, pp. 471-478, 2006.

[55] Y. Yang et al., "Ultra-high *Q* monocrystalline silicon carbide disk resonators anchored upon a phononic crystal," in *Hilton Head*, 2018.

[56] E. Cook et al., "A high-mass, eight-fold symmetric silicon carbide MEMS gyroscope," in *Hilton Head*, 2018.

[57] V. Srikar et al., "Thermoelastic damping in fine-grained polysilicon flexural beam resonators," *J. Microelectromech. Syst.,* vol. 11, no. 5, pp. 499-504, 2002.

[58] D. Cole et al., "Phonon-tunnelling dissipation in mechanical resonators," *Nature Communications,* vol. 2, no. 231, pp. 1-8, 2011.

[59] Z. Hao et al., "Support loss in micromechanical disk resonators," in *IEEE MEMS*, 2005.

[60] B. Harrington et al., "In-plane acoustic reflectors for reducing effective anchor loss in lateral–extensional MEMS resonator," *JMM,* vol. 21, no. 8, 2011.

[61] R. Tabrizian et al., "High-*Q* energy trapping of temperature-stable shear waves with Lamé cross-sectional polarization in a single crystal silicon waveguide," *Appl. Phys. Lett,* vol. 108, no. 11, p. 113503, 2015.

[62] M. Maldovan et al., "Sound and heat revolutions in phononics," *Nature,* vol. 503, no. 7475, pp. 209-217, 2013.

[63] J. Scott et al., "Vibration of an elastic strip with varying curvature," *Philosophical Transactions of the Royal Society of London, Physical Sciences and Engineering,* vol. 392, no. 339, pp. 587-625, 1992.

[64] L. Sorenson et al., "One-dimensional linear acoustic bandgap structures for performance enhancement of AlN-on-Silicon micromechanical resonators," in *Transducers*, 2011.

[65] J. Kilpatrick, A. Apostol and V. Markov, "Characterization of 3D MEMS structural dynamics with a conformal multi-channel fiber optic heterodyne vibrometer," *Proc. SPIE,* 2012.

[66] L. Fegely, D. Hutchison and S. Bhave, "Isotropic Etching of 111 SCS for Wafer-Scale Manufacturing of Perfectly Hemispherical Silicon Molds," *Transducers 2011,* 2011.

[67] L. Sorenson et al., "3D micromachined hemispherical shell resonators with integrated capacitive transducers," in *IEEE MEMS*, 2012.

[68] X. Lu et al., "High-frequency and high-quality silicon carbide optomechanical microresonators," *Scientific Reports,* vol. 5, p. 17005, 2015.

[69] A. Kermany et al., "Microresonators with Q-factors over a million from highly stressed epitaxial silicon carbide on silicon," *Appl. Phys. Lett.,* vol. 104, p. 081901, 2014.

[70] K. Dowling et al., "Inductive coupled plasma etching of high aspect ratio silicon carbide microchannels for localized cooling," in *ASME*, 2015.

[71] K. Dowling et al., "Profile evolution of high aspect ratio silicon carbide trenches by inductive coupled plasma etching," *JMEMS,* vol. 26, no. 1, p. 135, 2017.

[72] L. Luna et al., "Dry etching of high aspect ratio 4H-SiC microstructures," *ECS Journal of Solid State Science & Technology,* vol. 6, no. 4, pp. 207-210, 2017.

[73] C. Locke et al., "Demonstration of 3C-SiC MEMS Structures on Polysilicon-on-Oxide Substrates," in *Mater. Res. Soc. Symp. Proc.*, 2010.

[74] D. Senesky et al., "Aluminum nitride as a masking material for the plasma etching of silicon carbide structures," in *IEEE MEMS* , 2010.

[75] N. Okamoto et al., "Elimination of pillar associated with micropipe of SiC in high-rate inductively coupled plasma etching," *Journal of Vacuum Science & Technology A,* vol. 27, no. 2, p. 295, 2009.

[76] K.-B. Lee, L. Lin and Y.-H. Cho, "A Closed-form Approach for Frequency Tunable Comb Resonators with Curved Finger Contour," *Sensors and Actuators A,* pp. 523-529, 2008.

[77] K.-B. Lee and Y.-H. Cho, "A triangular Electrostatic Comb Array for Micromechanical Resonant Frequency Tuning," *Sensors and Actuators A,* pp. 112-117, 1998.

[78] S. Adams, F. Bertsch, K. Shaw, P. Hartwell and F. M. N. MacDonald, "Capacitance based Tunable Resonators," *J. Micromech. Microeng.,* vol. 8, pp. 15-23, 1998.

[79] C. Cabuz, K. Fukatsu, H. Hashimoto, S. Shoji, T. Kurabayashi, K. Minami and M. Esashi, "Fine Frequency Tuning in Resonant Sensors," *MEMS 1994,* pp. 245-250, 1994.

[80] W.-C. Chen, W. Fang and S.-S. Li, "High-*Q* Integrated CMOS-MEMS Resonators with Deep-Submicrometer Gaps and Quasi-Linear Frequency Tuning," *JMEMS,* vol. 21, no. 3, pp. 688-701, 2012.

[81] Y. Eun, J. Kim and L. Lin, "Resonant-frequency Tuning of Angular Vertical Comb-driven Microscanner," *Micro and Nano Systems Letters,* pp. 1-5, 2014.

[82] G. Piazza, R. Abdolvand, G. Ho and F. Ayazi, "Voltage-tunable Piezoelectrically-transduced Single-Crystal Silicon Micromechanical Resonators," *Sensors and Actuators A,* pp. 71-78, 2003.

[83] C.-P. Le and E. Halvorsen, "Wide Tuning-Range Resonant-Frequency Control by Combining Electromechanical Softening and Hardening Springs," *Transducers 2013,* pp. 1352-1355, 2013.

[84] R. Abdolvand and F. Ayazi, "An Advanced Reactive Ion Etching Process for Very-High Aspect Ratio Sub-Micron Wide Trenches in Silicon," *Sensors and Actuators A: Physical,* vol. 144, no. 1, pp. 109-116, 2008.

[85] W.-T. Hsu and A. Brown, "Frequency Trimming for MEMS Resonator Oscillators," *Frequency Control Symposium 2007,* pp. 1088-1091, 2007.

[86] M. Abdelmoneum, M. Demirci, Y.-W. Lin and C. Nguyen, "Location-dependent Frequency Tuning of Vibrating Micromechanical Resonators via Laser Trimming," *IEEE Ultrasonics, Ferroelectrics and Frequency Control,* pp. 272-279, 2004.

[87] M. Chiao and L. Lin, "Post-packaging Frequency Tuning of Microresonators by Pulsed Laser Deposition," *Journal of Micromechanics and Microengineering,* pp. 1742-1747, 2004.

[88] C. Courcimault and M. Allen, "High-*Q* Mechanical Tuning of MEMS Resonators using a Metal Deposition-Annealing Technique," *Transducers 2005,* pp. 875-878, 2005.

[89] R. Syms et al., "Electrothermal Frequency Tuning of Folded and Coupled Vibrating Micrmechanical Resonators," *Journal of Micromechanical Systems,* pp. 164-171, 1998.

[90] S. Enderling, J. Hedley, L. Jiang, R. Cheung, C. Zorman, M. Mehregany and A. Walton, "Characterization of Frequency Tuning using Focused Ion Beam Platinum Deposition," *Journal of Micromechanics and Microengineering,* pp. 213-219, 2007.

[91] J. Chang, K. Koh, B.-K. Min, S. Lee, J. Kim and L. Lin, "Synthesis and Bidirectional Frequency Tunung of Cantilever-shape Nano Resonators Using a Focused Ion Beam," *Applied Materials and Interfaces,* pp. 9684-9690, 2013.

[92] D. Joachim and L. Lin, "Characterization of Selective Polysilicon Deposition for MEMS Resonator Tuning," *Journal of Micromechanical Systems 2003,* pp. 193-200, 2003.

[93] K. Wang, W.-T. Hsu and C. Nguyen, "Frequency Trimming and Q-factor Enhancement of Micromechanical Resonators via Localized Filament Annealing," *Transducers 1997,* pp. 109-112, 1997.

[94] A. Hajjam, K. Dietrich, A. Rahafrooz and S. Pourkamali, "A Self-controlled Frequency Trimming Technique for Micromechanical Resonators," *Hilton Hewad 2012,* pp. 74-77, 2012.

[95] T. Remtema and L. Lin, "Active Frequency Tuning for Micro Resonators by Localized Thermal Stressing Effects," *Sensors and Actuators A,* pp. 326-332, 2001.

[96] B. Svilicic, E. Mastropaolo, R. Zhang and R. Cheung, "Tunable MEMS Cantilever Resonators Electrothermally Actuated and Piezoelectrically Sensed," *Microelectronic Engineering,* vol. 145, pp. 38-42, 2015.

[97] R. Syms and D. Moore, "Focused Ion Beam Tuning of In-plane Vibrating Micromechanical Resonators," *Electronics Letters,* pp. 1277-1278, 1999.

[98] S.-C. Jun, X. Huang, M. Manolidis, C. Zorman, M. Mehregany and J. Hone, "Electrothermal tuning of Al-SiC nanomechanical resonators," *Nanotechnology,* pp. 1506-1511, 2006.

[99] N. Manca, L. Pellegrino, T. Kanki, S. Yamasaki, H. Tanaka, A. Siri and D. Marre, "Programmable Mechanical Resonances in MEMS by Localized Joule Heating of Phase Change Materials," *Advanced Materials,* vol. 25, pp. 6430-6435, 2013.

[100] V. Challa, M. Prasad, Y. Shi and F. Fisher, "A Vibration Energy Harvesting Device with Bidirectional resonance Frequency Tunability," *Smart Materials and Structures,* pp. 1-10, 2008.

[101] J. Sung, J. Kim, W. Moon and G. Lim, "A Novel Resonant-Frequency-Trimming Method using CNT Rope Synthesis," *Journal of Microelectromechanical Systems,* vol. 23, no. 6, pp. 1383-1388, 2014.

[102] S. Enderling, C. Brown, M. Balakrishan, J. Hedley, J. Stevenson, S. Bond, C. Dunare, A. Harris, J. Burdess, M. Mitkova, M. Kozicki and A. Walton, "Integration of a Novel Electromechanical Tuning Scheme with MEMS Surface Micromachined Resonators," *MEMS 2005,* pp. 159-162, 2005.

[103] C. Peters, D. Maurath, W. Schock and Y. Manoli, "Novel Electrically Tunable Mechanical Resonator for Energy Harvesting," *Proceedings of PowerMEMS 2008,* pp. 253-256, 2008.

[104] E. Leland and P. Wright, "Resonance Tuning of Piezoelectric Vibration Energy Scavening Generators using Compressive Axial Preload," *Smart Materials and Structures,* pp. 1413-1420, 2006.

[105] H. Hosseinzadegan and A. Lal, "Tip-based Graphene Etching for MEMS Resonator Frequency Trimming," *Transducers 2013,* pp. 798-801, 2013.

[106] A. Samarao and F. Ayazi, "Postfabrication Electrical Trimming of Silicon Micromechanical Resonators via Joule Heating," *Journal of Microelectromechanical Systems,* pp. 1081-1088, 2011.

[107] B. Hamelin, V. Tavassoli and F. Ayazi, "Eutectic Trimming of Polysilicon Micro Hemispherical Resonating Gyroscope," *Sensors 2013,* 2013.

[108] G. Blanco-Gomez and V. Agache, "Experimental Study of Energy Dissipation in High Quality Factor Hollow Square Plate MEMS Resonators for Liquid Mass Sensing," *Journal of Microelectromechanical Systems,* vol. 21, no. 1, pp. 224-234, 2012.

[109] F. Schaffler, "SiGe," in *Properties of Advanced Semiconductor Materials GaN, AlN, InN, BN, SiC, SiGe*, New York, Eds. Levinshtein M.E., Rumyantsev S.L., Shur M.S., John Wiley & Son, Inc., 2001, pp. 149-188.